



**HAL**  
open science

# Surface plasmon resonance based biosensor applied to phytosanitary domain

Sivaramakrishnan Ganesan

► **To cite this version:**

Sivaramakrishnan Ganesan. Surface plasmon resonance based biosensor applied to phytosanitary domain. Micro and nanotechnologies/Microelectronics. Université de Lille, 2020. English. NNT : 2020LILUI059 . tel-03622687

**HAL Id: tel-03622687**

**<https://theses.hal.science/tel-03622687>**

Submitted on 29 Mar 2022

**HAL** is a multi-disciplinary open access archive for the deposit and dissemination of scientific research documents, whether they are published or not. The documents may come from teaching and research institutions in France or abroad, or from public or private research centers.

L'archive ouverte pluridisciplinaire **HAL**, est destinée au dépôt et à la diffusion de documents scientifiques de niveau recherche, publiés ou non, émanant des établissements d'enseignement et de recherche français ou étrangers, des laboratoires publics ou privés.

## **THESE DE DOCTORAT**

**Présentée à**

l'Université de Lille

Ecole Doctorale Régionale Sciences Pour l'Ingénieur

Pour l'obtention du grade de

**DOCTEUR de l'Université de Lille**

Spécialité: Electronique, Microélectronique, Nanoélectronique et Micro-ondes

Par

**Sivaramakrishnan GANESAN**

*Utilisation de la résonance plasmonique de surface pour la réalisation de capteurs  
appliqués au domaine phytosanitaire*

*Surface plasmon resonance based biosensor applied to phytosanitary domain.*

Thèse soutenue le 15 Décembre 2020

Tuami LASRI

*Professeur, Université de Lille*

Serge HABRAKEN

*Professeur, Université de Liège*

Gilles LERONDEL

*Professeur, Université Technologique de Troyes*

Fabian DORTU

*Ingénieur, MULTITEL (Mons)*

Sophie MARICOT

*Maitre de Conférences, Université de Lille*

Jean-Pierre VILCOT

*Directeur de Recherche, CNRS (Villeneuve d'Ascq)*

Président

Rapporteur

Rapporteur

Examineur

Encadrant

Directeur de thèse



## Acknowledgements

I would like to express my greatest thanks to my thesis director, **Jean-Pierre Vilcot** for his excellent advices and openness for scientific discussion and guidance during the three years of my PhD journey. I would also extend my greatest thanks to my thesis supervisor, **Sophie Maricot** for here great support and encouragement during the journey. I once again thank them for giving me freedom and long supporting hands till the end of my work. I thank University of Lille and the INTERREG project for the funding opportunities provided for my thesis work.

I would be very happy to thank **Marc Guillon**, my master thesis director and **Marco Pascucci**, with whom I worked during my master project. Marco was my inspiration for my PhD carrier, I thank him a lot for motivating me.

I have to extend my special thanks to a colleague, **Laurent Hay** for his well wishes and for being very much supportive during the complete journey. I convey my thanks to him and his family for letting me feel that I am not alone.

I thank **Mohamed Bouazzaoui**, and all the OPTO team members, **Phuong Dp**, **Mohamed-Taieb Bakouche**, **Thanh Bui**, **Pierre-Vincent Dugué** and all the members of the group for their support and encouragements. I thank all the members of administrative staff from IEMN.

I extend my thanks to all the engineering staff of IEMN clean rooms who provided their best support during my work as well as to the mechanical technicians of IEMN and Centrale Lille for their support. I extend my thanks to all members of IEMN and special thanks to the members of the cleaning and sanitary service of IEMN who maintain the rich and healthy environment for us to work healthy.

I thank all my friends from Lille, **Ankush Kumar**, **Reethuraj Pandey** for being very close during the journey. I also extend my thanks to, **Gurpreeth**, **Sri Saran** and all other friends from IEMN, Lille.

I thank my friends from India, **Praveen Kumar, Saravanan, Yuvaraj, Padmanaban, Sunil Kumar** for always being my support during all times. I extend my special thanks to **Dheeraj Singh** and his family, **Usha** aunty and their family for their well-wishing, support and encouragements from India.

At the end I have to thank my Mother, **Usha** and my Father, **Ganesan** who nurtured and nurturing me for what I am today. I have got great parents who struggled a lot and gave me a rich education, I bow my head towards them to thank them for giving me an opportunity to pursue PhD. I have to thank my great brother **Aakash** from whom I always learn and I have to thank him a lot for being with me during hard and happy times and keep motivating. I again thank my family who will be always my pillars for my future. Final thanks to **Krishna Moorthy** sir, my guru from school.

My wholehearted thanks to all of them who have travelled with me during my PhD journey.

## Abstract

The overall goal of this study was to develop a portable biological detection system with high sensitivity, accuracy and repeatability to be used in either the phytosanitary or the medical domain. This system is based on the Surface Plasmon Resonance (SPR) physical principle. Such a use of this principle is already achieved but leads to laboratory equipment. The goal here is to democratize its use up to an on field or point of care measurement system. In this context and within the frame of the BIOSENS INTEREG FWVL project, I worked more particularly on several developments around the sensor. From all the existing biosensor technologies, surface plasmon resonance (SPR) sensing technology has received continuous attention due to its advantages of a high-sensitivity, label-free and fast response time. Although the SPR sensing technique being legend in the sensor community, currently the temperature of the sample needs to be carefully maintained and controlled because SPR signal varies with temperature and any change in SPR signal can be interpreted as a biological interaction. This gives a huge challenge in the portable application that is targeted since embedding of a temperature-controlled chamber size and energy consuming. A SPR sensor design including 4 SPR channels has been made and the temperature is controlled in real time by using Joule effect. Temperature behavior has been modelled under COMSOL and we experimentally demonstrated that the temperature modulation of SPR channel by Joule effect does not affect the detection scheme. Water was heated by injecting current through the plasmonic layer and the refractive index change of water due to temperature was measured and compared with the theory. We also demonstrated that the temperature of each of the 4 channels can be controlled independently without any thermal crosstalk. In order achieving a more precise monitoring of sample temperature, a temperature sensor was also fabricated on top of the plasmonic layer, allowing the real temperature at the sensor surface to be monitored in real time. This temperature control can so be used either to maintain the temperature of biologic samples or to identify the effect of temperature on biomolecular interactions. On addressing the cost of the sensing tool, a flexible and cheap SPR sensor made on tape has been fabricated and tested. Air and water plasmonic responses were measured using such a "tape sensor". A PDMS prism has already been investigated and combined to the tape sensor making then a very cheap sensing platform.



## Table of Contents

Chapter 1: INTRODUCTION.....	1
1.1 Introduction to bio-sensing .....	3
1.1.1 Main techniques.....	3
1.1.2 Advantages and drawbacks of transducer types .....	7
1.1.3 Application domain of biosensors .....	9
1.1.4 Application domain targeted in this work .....	10
1.2 Introduction to SPR biosensing.....	13
1.2.1 Propagative surface plasmon resonance (SPR) .....	15
1.2.2 Basic principles.....	16
1.3 State-of-art of SPR biosensor.....	18
1.3.1 Academic research on SPR biosensor .....	20
1.3.2 Industrial level .....	21
1.4 Conclusion.....	23
Chapter 2: THEORY OF SURFACE PLASMON RESONANCE APPLIED TO BIOSENSING.....	25
2.1 Theory .....	27
2.2 Performance of a plasmonic sensing technique .....	36
2.3 Modelling of the SPR.....	37
2.3.1 Influence of the refractive index of coupling optics.....	37
2.3.2 Influence of plasmonic layer thickness .....	38
2.3.3 Influence of wavelength .....	41
2.3.4 Matching plasmonic layer thickness to interrogation wavelength .....	43
2.3.5 Spectral interrogation .....	44
2.3.6 Influence of plasmonic layer composition.....	46
2.3.7 Conclusion.....	52

Chapter 3: EXPERIMENTAL BENCHES .....	53
3.1 Angular interrogation scheme .....	55
3.1.1 Set-up overview .....	55
3.1.2 Set-up calibration.....	57
3.2 Spectral interrogation method .....	62
3.2.1 Set-up overview .....	62
3.2.2 Set-up calibration.....	63
3.3 Conclusion:.....	66
 Chapter 4: SPR SENSOR WITH INTEGRATED TEMPERATURE CONTROL.....	69
4.1 Basic idea that governs the implementation of the integrated temperature control	71
4.2 Design and fabrication of multichannel SPR sensor.....	72
4.3 Plasmonic channel as a Joule's effect heater. ....	74
4.4 Modelling the thermal behaviour of the plasmonic metal layer.....	75
4.4.1 Modelling of Joule's effect .....	75
4.4.2 Matching the modelling with the experiments .....	78
4.4.3 Time dependence .....	79
4.5 Characterization of the thermal behaviour of the plasmonic layer .....	79
4.5.1 Measurement set-up.....	79
4.5.2 Thermal measurements.....	81
4.6 Thermal measurements on SPR experiment. ....	84
4.7 Inbuilt-real time temperature sensor .....	86
4.7.1 Pt film calibration .....	88
4.7.2 Design and fabrication of the multichannel SPR sensor integrating temperature sensor.....	90
4.7.3 Modelling of SPR sensor with Pt resistor.....	92
4.7.4 Thermal characterization .....	93
4.7.5 Improved 4-channel device design.....	96

4.8 Validation of multi-channel temperature operation .....	97
4.8.1 Experimental validation using thermal IR imaging.....	97
4.8.2 Experimentation on the improved 4-channel design .....	99
4.9 Conclusion.....	100
Chapter 5: USE OF POLYMER OPTICS FOR SPR .....	103
5.1 Flexible SPR sensor .....	105
5.1.1 Modelling a tape based sensor.....	105
5.1.2 Fabrication of tape sensor.....	107
5.1.3 SPR experiment using tape sensor.....	107
5.2 Optical coupling prism using PDMS .....	111
5.2.1 Modelling.....	111
5.2.2 Fabrication of PDMS prism.....	113
5.2.3 Using PDMS prism (with a glass sensor).....	114
5.2.4 Using PDMS prism (with a flexible sensor).....	116
5.3 Conclusion.....	119
Chapter 6: BIMETALLIC SPR SENSOR FABRICATION .....	121
6.1 Fabrication of bimetallic Ag/Au sensor: .....	123
6.2 Experiments on angular bench at 1550nm .....	124
6.2.1 Calibration .....	124
6.2.2 Comparison between gold and bi-metallic sensor .....	125
6.3 Experiments on spectral bench in the visible range .....	127
6.3.1 Calibration .....	127
6.3.2 Comparison between gold and bi-metallic sensor .....	128
6.4 Conclusion:.....	129

CONCLUSION AND PERSPECTIVES .....	131
Conclusion.....	131
Perspectives .....	135
APPENDICES .....	139
Appendix A: Fabrication of PDMS microfluidics .....	141
Appendix B: On the particular use of Al <sub>2</sub> O <sub>3</sub> layer .....	143
Appendix C: On the response curves for high temperature .....	147
Appendix D: On the effect of current injection on polarization .....	151
REFERENCES .....	153

## Chapter 1: INTRODUCTION

Within this chapter, I will make a quick introduction of bio-sensing and its different declinations.

I will then present the context of my work and describe briefly its main content.

The chapter will finish by the overall description of Surface Plasmon Resonance technique that is the one I worked on during this work.



## 1.1 Introduction to bio-sensing

A biosensor is a device that allows obtaining a user-readable signal from a biological solution or interaction. Generally, biosensors determine the concentration of a specific biomolecule, called analyte, in a sample or analyse the interaction between specific biomolecules. In a first approach and a fully generic way, a biosensor can be globally illustrated by the combination of two main components that are a bio-recognition element [1] and a transducer. The bio-recognition element can be antibody, DNA, enzyme, cell, or any other biologic species. The transducer is a physical device that can be based on one or a combination of electrical, mechanical, piezoelectric, acoustic, optical principle(s) [2]. Figure 1.1 shows schematically the components of a biosensor.

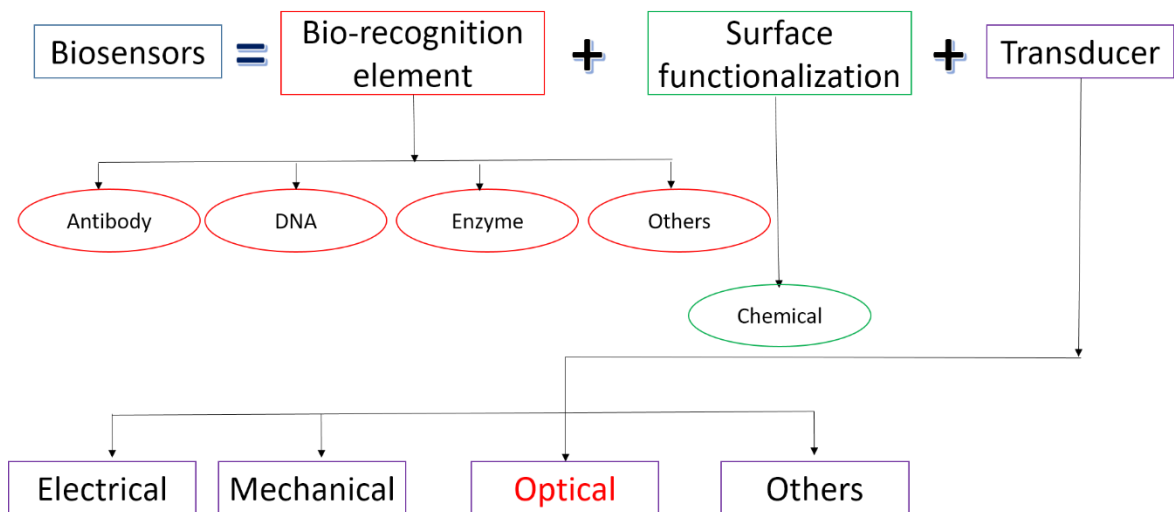


Figure 1.1 Generic constituents of a biosensor.

### 1.1.1 Main techniques

As mentioned above, there are different physical transducing schemes, the most widespread ones are based on electrical [3-5], mechanical [6-8], or optical [9-12] principles.

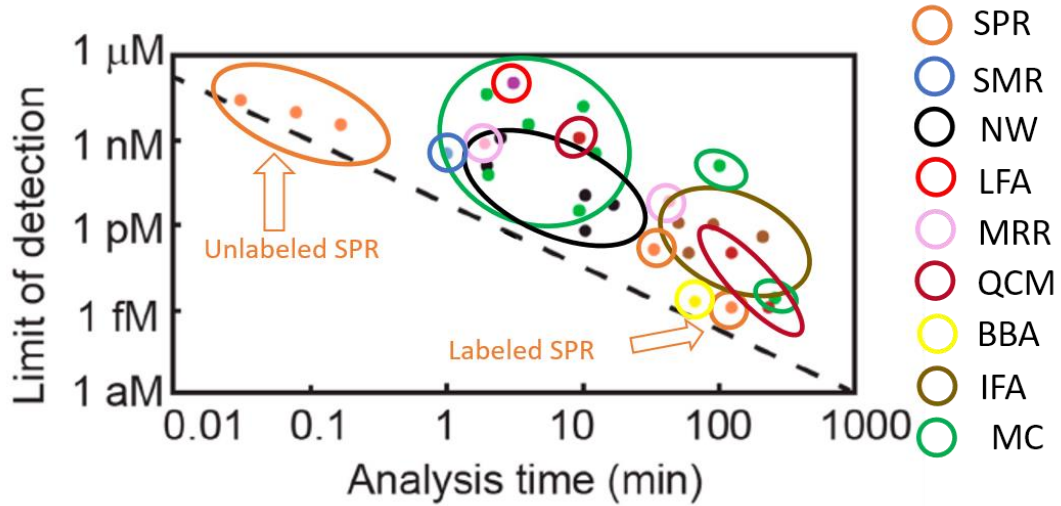


Figure 1.2 Comparison of the Limit of detection vs analysis time for various bio-sensing techniques(transducer types)[12]. SPR = Surface Plasmon Resonance; SMR = Suspended Microchannel Resonators; NW = Nanowires; LFA = Lateral Flow Assay; MRR = Microring Resonator; MC= Microcantilever; QCM = Quartz Crystal Microbalance; BBA = BioBarcode Assay; IFA = Immunofluorescence Assay.

Transducer types				
Electrical	Mechanical	Optical	Magnetic	Chemical
NW-FET	QCM MC	SPR SMR MRR	BBA	IFA

Types of transducers and the existing bio sensing techniques are mentioned in Table 1.1.

Table 1.1 Transducer types used for various bio-sensing techniques.

A very brief introduction on the types of transducers and the techniques that are currently used for bio sensing application are discussed below.

### Electrical transducer:

They transduce the biological interaction into electrical signals like current or impedance that can be processed directly. There are various electrical transducers like capacitive, conductive and many other but the most promising among these devices which are used

for bio-sensing application at the laboratory level is the NanoWire Field Effect Transistor (NW-FET) [14-18].

A NW-FET biosensor is composed of a semiconductor nanowire that can be considered as the channel of a classical FET device. The extremities of this nanowire can then act as the source and drain electrodes. Charged biomolecules that adsorb onto the nanowire act as a usual gate electrode, producing a surface electric field and varying the conductivity within the device. The resulting source-drain current can be then measured as a monitor of the biomolecule interaction.

### **Mechanical Transducer:**

These biosensors use mechanical forces to report on a biomolecule presence or interaction. Example of such a device is the micro-cantilever [19-22]. Micro-cantilevers oscillate at a characteristic frequency, much like a tuning fork. This frequency is a function of the shape and material properties of the cantilever and therefore changes with its mass and so upon the adsorption of biomolecules. The detection and the change in oscillation frequency can be monitored by reflecting a laser off the surface and tracking its position, much the same way as in an atomic force microscope.

An alternative mechanical sensor is the quartz crystal microbalance (QCM), which relies on the oscillation of a crystal and the change in resonant frequency as material adsorbs. This oscillation is stimulated electronically, but this frequency change occurs due to the mechanical coupling of bound biomolecules and the crystal surface [19], [23].

### **Optical Transducer:**

Optical biosensors use the interaction between light and matter to report the presence of the analyte. These technologies may be divided into two classes. The first one uses spectroscopy, under different declinations, to isolate the signal due to the analyte, including Fourier Transform Infra-Red (FTIR) spectroscopy [24] and ultraviolet-visible (UV-vis) spectroscopy [25, 26]. The most common technique in this class is fluorescence, which

involves the absorption of a photon by a molecule and the subsequent emission of a second photon of lower energy. Species that exhibit minimal fluorescence when exposed to a particular wavelength of light available for the experiment may be labelled with a fluorophore better suited to that wavelength to enable detection based on the intensity and spectrum of emitted light. The fluorescence signal is isolated using optical filters to eliminate background and excitation light, and collected using a detector (e.g. photodiode, photomultiplier tube, avalanche photodiode, or charge-coupled device).

Fluorescence technique exhibits two key drawbacks [27, 28]. First, attaching a fluorescent tag to the analyte can interfere with the binding reaction that occurs during specific sensing. Second, quantitative fluorescence measurements can be inaccurate in the limits of both high and low concentrations of the analyte [28]. Alternative fluorescence assays range from classical biochemical methods, such as Western blots or ELISA assays, to new sensor technologies such as Total Internal Reflection Fluorescence (TIRF). In TIRF, one monitors the adsorption of material by measuring the amount of light given off by fluorescent tags attached to the surface-bound analyte molecules. These fluorophores are excited using the evanescent field that results from total internal reflection at the substrate, often a glass prism. Fluorophores may only be excited by the evanescent wave [29], ensuring that only those fluorophores within a short distance ( $< 100$  nm) of the surface will contribute to the emitted fluorescence signal. This technique significantly improves the sensitivity of the measurement.

Currently, the most prominent optical biosensors are based on either surface plasmon resonance (SPR) or fluorescence [30] owing to their ability to detect minimum concentration levels as shown in Figure 1.2 [13].

As can be seen from Figure 1.2, among the various kinds of biosensors, label free SPR based biosensor offer the shortest analysis time on the order of few seconds that can allow the real time monitoring of molecular interactions. But on the other hand, this technique exhibits the highest detection limit (minimum limit: 1nM) compared to other techniques. However labelled SPR technique could reduce the limit of detection to 1fM even though loosing fastest reaction time (100min) and label-free assets.

It is also necessary for a biosensor to detect the smaller molecules as possible in shortest time since the interest of the application always lies in the scale lower than  $1\mu\text{m}$  as shown in Figure 1.3.

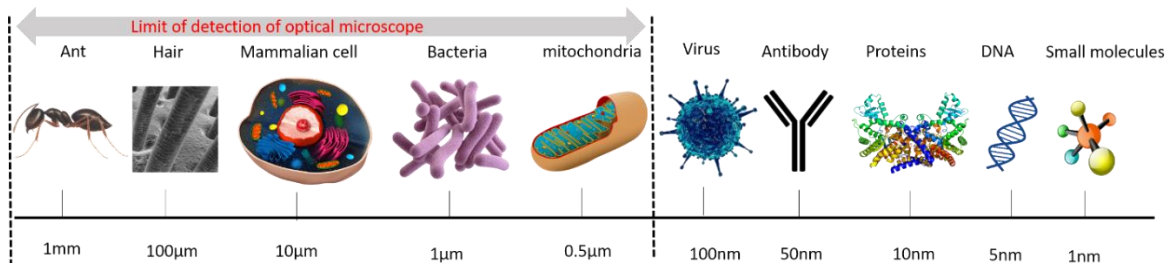


Figure 1.3 The size of biomolecules being a limit for the optical microscopies.

Due to the advancement in optical microscopy technologies, the biological interaction of the bigger molecules is easily monitored. The experiments are conducted by using labels which improve to detect at femto-molar range at the expense of a compromised analysis time [31]. Sensitivity improvement is an ever-lasting goal in biosensor development. The requirement for sensitivity indeed varies from case to case. For example, one does not need a very high sensitivity for glucose detection since glucose concentration is high in the blood. This is part of the reason for the success of glucose monitors. However, in many cases, it is very important to develop highly sensitive biosensors, optimally single-molecule detection, to meet the requirement of molecular diagnostics and pathogen detection.

### 1.1.2 Advantages and drawbacks of transducer types

According to the type of transducers, the sensitivity and the performance of the bio-sensing differs. Some advantages and disadvantages of the currently used transducers are discussed in the Table 1.2.

Transducer Type	Method	Advantages	Disadvantages	LOD
Mechanical	QCM MC [32-36]	<ul style="list-style-type: none"> <li>• High sensitivity</li> <li>• Label free</li> <li>• Easy to Fabricate</li> <li>• Commercially available.</li> <li>• Real time.</li> </ul>	<ul style="list-style-type: none"> <li>• Experiments has to be performed in vacuum.</li> <li>• Complex preparation of the experiment.</li> <li>• Mechanical way might damage the biological molecule due to stress or strain.</li> <li>• biochemical recognition in a liquid medium is a great challenge</li> <li>• Sensitivity limited by size constrains.</li> <li>• Surface functionalization remains key issue.</li> </ul>	1fM-1pM
Electrical	NW-FET [37-40]	<ul style="list-style-type: none"> <li>• Extremely sensitive.</li> <li>• Commercially available technology.</li> <li>• Real time measurement.</li> <li>• Simple interpretation.</li> </ul>	<ul style="list-style-type: none"> <li>• Difficult for fabrication</li> <li>• Some bio molecules may get damaged due to electric field.</li> <li>• Sensitive to environment.</li> </ul>	1pM-1nM
Optical	SPR [34, 41, 42] SMR [130, 131, 132] MRR [133, 134]	<ul style="list-style-type: none"> <li>• Wide range of analysis.</li> <li>• Real time.</li> <li>• High sensitive and label-free.</li> <li>• Good for liquid environment.</li> <li>• Having microfluidic facilities.</li> <li>• Measurement of multiple interactions at the same time.</li> <li>• Usage of only small quantity of samples.</li> </ul>	<ul style="list-style-type: none"> <li>• Dependence on surface functionalization.</li> <li>• Low sensitive compared to electrical and mechanical biosensor.</li> <li>• Required knowledge on the system mechanism.</li> </ul>	1μM-1nM  1nM  1pM-nM

Table 1.2 Some of the advantages and disadvantages of the currently used transducer types of a biosensor.

### 1.1.3 Application domain of biosensors

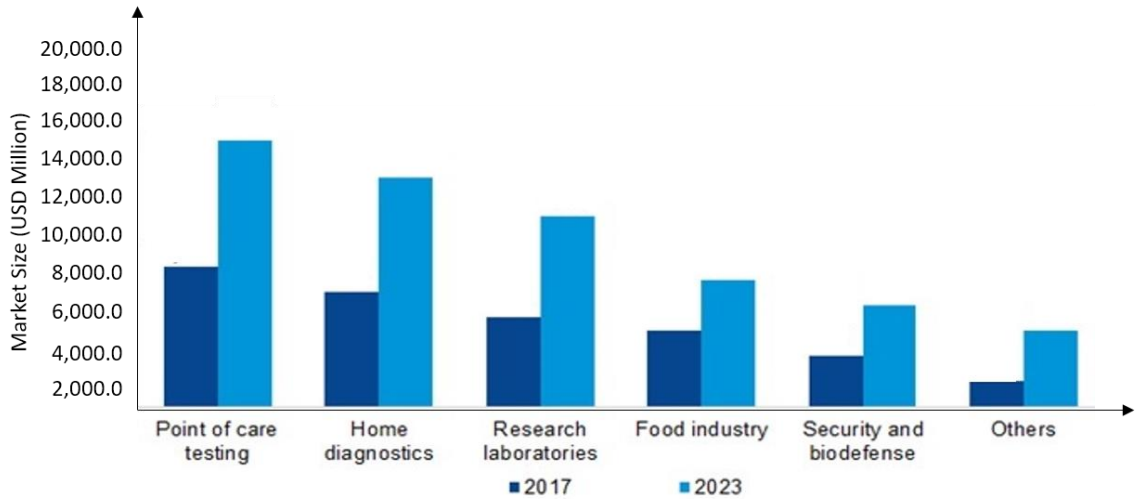


Figure 1.4 Biosensor market share in 2017 and its future expected developments [43].

As seen in Figure 1.4, the biosensor market is expected to double in the year 2023 compared to the year 2017. We can also notice that a lot of different application domains exists. With this hint, the research for the right transducer that can be better adapted to a particular application field is a real challenge since requests can be different from one domain to another. When it comes to the point of care testing [43], the main property of a biosensor is expected to be a noninvasive sensor. Non-invasive procedures are those which leave the skin intact and unbroken. They have become increasingly popular in recent years, not just because of the lack of a scar but because they often involve less time during treatment and afterward for recovery.

The second highest application domain of biosensors will be in the home diagnostics [44]. Likewise, the biosensors are not only used in the medical and clinical domains but also in various application domains as shown in the histogram (Figure 1.4). And few more biosensor application fields are life science research [45-47], health care and medical diagnostics [48-50], environmental pollution monitoring, drug screening, and discovery, food safety and analysis and military applications [51, 52] based on interest. With such a myriad of diverse applications, the overall biosensors market is expected to reach USD 35,729.14 Million by 2025 (Source: MRFR Analysis [43]).

There is intensive research on biosensors and each biosensor is characterized by a method that translates the quality and quantity of analyte present in the sample into a user measurable signal. Biosensor research is a highly interdisciplinary venture that brings together physicists, biologists, chemists, doctors, and engineers. As can be seen from Figure 1.1, the different parts of biosensors have to be developed by a specialist and all parts to be collaboratively optimized for a bio-sensing system to work.

#### 1.1.4 Application domain targeted in this work

The project I worked on is funded by the European Union through an INTERREG France-Wallonie-Vlaanderen programme, and more particularly within the BIOSENS project that is part of the SMARTBIOCONTROL portfolio (01/10/2016 to 31/12/2020). BIOSENS is a cross-border collaboration between physicians, micro-technologists, biologists, microbiologists, and agronomists to develop a portable biosensing equipment in the phytosanitary application domain. This equipment will be used for the early detection of pathogens for which the effectiveness of a biological treatment requires a quick response, before the appearance of the first symptomatic signs. A secondary application domain is set on the detection of pathogens in the medical domain. The link between those two is related to the pathogen to be detected that are fungi in both applications.

What are these pathogens and why they need to be detected at their early stage? As mentioned above, a first application is in the phytosanitary domain and more especially on the detection of a wheat crop fungus, *Zymoseptoria tritici*. It is a foliar disease that can reduce the yield of wheat by 30 to 50%, so having a huge economic impact. This fungal disease is difficult to control because populations contain extremely high levels of genetic variability and it has very unusual biology for a pathogen. *Zymoseptoria tritici* has an active sexual cycle under natural conditions, which is an important driver of septoria tritici blotch epidemics and results in high genetic diversity of populations in the field [53]. The BIOSENS project aims to develop real time detection equipment aiming to detect the fungus in its early-stage development, i.e. before symptomatic signs appear, and so to minimize the pesticide treatments. Moreover the other projects of the SMARTBIOCONTROL portfolio aim at determining, developing and producing

alternative biopesticides that could force the agricultural community to change practices in the way of using chemical pesticides. At the end of the project, the expectation is to develop a portable equipment that can be used on fields without the request of high-level biology technicity. It should be able to survey the appearance of the fungus as well as to monitor the efficiency of the biopesticide treatment. The ultimate goal is then reaching a greener agriculture using bio treatments and optimizing their spreading. The medical application concerns a human fungus, *Candida Albicans* that is naturally present in human body. During an immune or hormonal imbalance, it can proliferate and becomes then pathogenic by releasing toxins. This is usually mild but can be severe in case of immunocompromised patients. The goal is the same than in the previous case, i.e. to detect the pathogen proliferation as soon as possible in order to lighten the curative treatment. For this purpose during the BIOSENS project, we have developed a biosensing tool that can be used for detecting the presence of both fungal pathogens, *Zymoseptoria tritici* and *Candida Albicans*. This biosensing tool consists of various elements such as sensor, a bio-recognition element, a reading equipment and a data processing. The sensor and the bio-recognition are combined together into a biosensor that transduces a biological interaction into a signal. This signal is read using a reading equipment and data processing is finally applied to convert raw results into user readable data. Finally, the integration of all these elements is a biosensing tool (see Figure 1.5).

Each part of this tool was developed by one of the project partners that are:

- the C.A.R.A.H institute (agronomists and micro-biologists): they were in charge researching the specific DNA sequence allowing the detection of *Zymoseptoria tritici*. They also developed the process flow extracting DNA of the pathogen from the plant, soil or air environment up to the preparation of the test solutions. From their study, we got the DNA sequences to be used as probes on our sensors.
- the CHU de Lille (medicine, biologists); they were in charge researching the antibody for the detection of *Candida Albicans* fungus. This protein-based interaction is also planned to be implemented for the *Zymoseptoria tritici* at the end of the project.
- Materia Nova and University of Liège (physicists): they worked on the way using Localized SPR (LSPR) and more especially on the way fabricating "low cost" LSPR sensors.

- Multitel (Research and Innovation Center) was in charge fabricating the portable SPR equipment. They implement some aspects of optical reading system and sensor developments presented in this work.

- CSL (Centre Spatial de Liège) worked on the development of localized SPR sensing and corresponding reading equipment.

The sensor was developed by Material Nova and CSL (LSPR) and IEMN (SPR). The biorecognition element was developed by CHU Lille and Carah where CHU was developing antibodies for both pathogens, *Zymoseptoria tritici* and *Candida albicans*, and Carah was developing the DNA for the *Zymoseptoria tritici*. Both, antibodies and DNA, entities have to be functionalized on the sensor surface. The reading equipment was developed at CSL, IEMN, and Multitel. The data processing was shared between IEMN and Multitel. In the end, the integration of all those elements was done at Multitel. All the elements of the biosensing tool and the project partners who worked on the development of each of the element are shown in Figure 1.5. During my thesis, I have worked on the development of both the element sensor and the reading equipment.

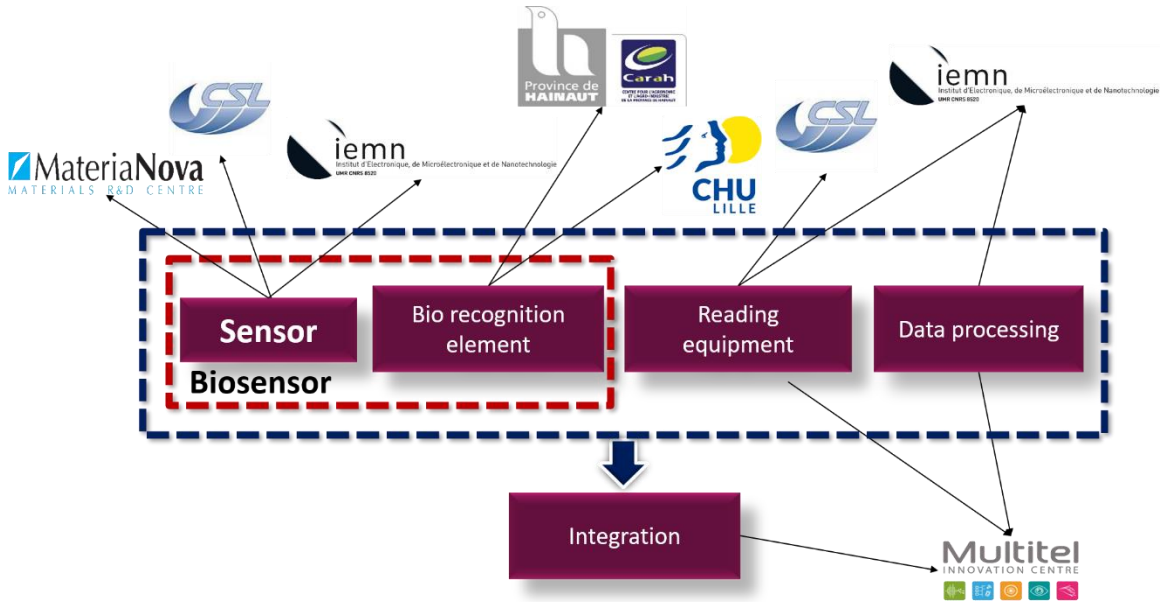


Figure 1.5 BIOSENS project: activities of partners.

My thesis work was carried out at Institut d'Électronique de Microélectronique et de Nanotechnologie (IEMN) at University of Lille and focused more especially on the study of different developments in the SPR detection technique aiming at matching its

operability, and eventually its cost, with the targeted applications. In particular, temperature affects particularly the SPR measurements. Two main developments were so investigated during this work:

- in order to get a portable detection system whatever it concerns detection in fields for the agricultural domain or point of care testing for the medical domain, idea was to remove the bulky temperature controlled environment that is commonly used by an integrated temperature control at sensor level.

- in order to ease the setting-up of the SPR sensor on the optical reading system and also, perhaps, to decrease the analysis cost, the use of polymer based optics was tested at coupling prism and sensor level.

## 1.2 Introduction to SPR biosensing

Visualization of the Surface Plasmon Resonance phenomenon can be firstly observed on the Lycurgus cup [54, 55] shown in Figure 1.6, fabricated by the Romans in the 4<sup>th</sup> century.



*Figure 1.6 Lycurgus cup, an ancient Roman nanotechnology example.*

Under daylight, the cup appears as green colour (Figure 1.6 left), but when a light source is placed inside the cup the transmitted colour will make it look like the glass glows in red as shown (Figure 1.6 right). This phenomenon also happens to stained glass in the Sainte Chapelle, the transmitted light from outside not only shows exquisite colour but also exhibits varying colour based on the time of the day and the viewing point. Due to the changing solar incident angles, the different colour patches on the window show an intensity change and colour variation. These astonishing optical effects are effectively due

to the plasmonic resonance and the "secret "ingredient embedded in the glass that is now called as metallic nanoparticle (NP).

The embedded metallic NPs in the ruby glass is typically 5-60 nm in size, which are much smaller than the incident wavelength. Light interacts with these sub-wavelength NPs and created a plasmonic wave oscillating locally around the NP under a physical principle now denominated localized surface plasmon resonance (LSPR). When the electron cloud is displaced relative to the atom nuclei, the Coulomb force between the nuclei and electrons generates a restoring force and results in a collective oscillation of the electron cloud regarding the fixed nuclear array known as LSP shown in Figure 1.7.

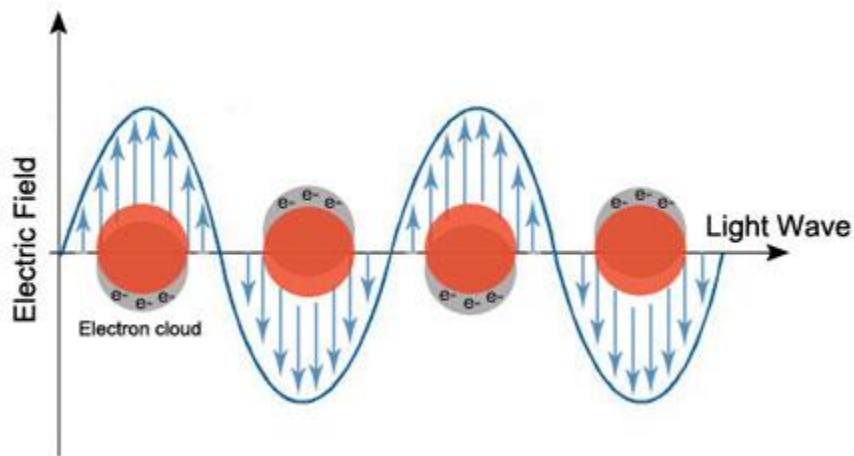


*Figure 1.7 Localized surface plasmon resonance in gold nano particles*

The LSPR is determined by the metal properties, the shape and size of the metal, and, similar to SPR, the refractive index of the surrounding medium which is the basis of the (L)SPR sensing applications.

Localized plasmons in metal nanoparticles are excited directly by light illumination independent of the angle. If the condition of the illuminating light is fulfilled then the light is coupled to the plasmon (with an evanescent field around the NP) and leads to an intensity drop in the transmitted light. Therefore, the plasmon excitation corresponds to the maximum observed in absorbance as shown in Figure 1.8. Upon changes of the refractive index in the vicinity of the NPS, the coupling condition changes and leads to a shift of the peak maximum.

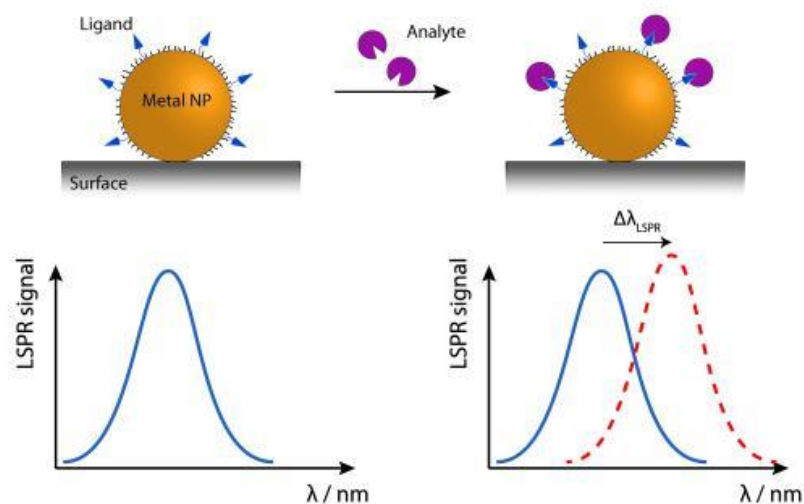


Figure 1.8 LSPR Absorbance curve for varying refractive index around the Au nanoparticle [56].

### 1.2.1 Propagative surface plasmon resonance (SPR)

During an experiment performed by Woods in 1902 and 1912 at Johns Hopkins University, he noticed that when he shone a polarized white light on a diffraction grating, a pattern of unusual dark and bright bands appeared at the reflection [12, 57]. Although Woods experiment could not answer the real phenomena behind the bright and dark bands of light, Lord Rayleigh in 1907 found that the scattered field was singular at wavelengths for which one of the spectral orders emerged from the grating at the grazing angle [58]. These singularities appeared only when the electric field of the optical electromagnetic wave was polarized perpendicular to the rulings of the gratings. His theory answered normally to the Woods experiment behaviour. Woods further research suggested that both P and S polarization anomalies exist but only P anomalies were found on gratings with deep groves [59]. Finally, theoretical analysis by Fano in 1941 concluded that these anomalies were associated with surface waves (surface plasmon) supported by the network [60]. This phenomenon was later described during the 1970s in terms of excitation of electromagnetic evanescent waves at the surface of thin metal to excite the surface waves. The surface plasmon (SP) or surface plasmon polariton (SPP) is a non-radiative electromagnetic surface wave that exists at the interface between a metal (few tenths of nanometres) and a dielectric medium (air, water, fluid, etc). They do not exist spontaneously, but it is possible to excite

them either by using an incident photon or electron bombardment. Optical stimulus is nevertheless the easiest and commonly used way creating SPPs.

### 1.2.2 Basic principles

To obtain the surface plasmon to be in a resonant condition, the incident photons must have the same momentum as that of the surface wave. Few techniques could satisfy the above conditions to achieve the resonance and generate different operating principles:

1. Angular interrogation,
2. Spectral interrogation,
3. Phase interrogation,

that distinguish upon the way excitation and observation of plasmon resonance is made.

#### 1.2.2.1 Angular interrogation:

Using a monochromatic input light beam, the plasmon resonance phenomenon is angle and polarization dependent [61]. Hence one can send a p-polarized light through a glass prism in a certain fixed angle to increase the wavenumber and achieve the resonance condition at a particular wavelength (as shown in Figure 1.ç). This configuration of exciting surface plasmon waves is known as Kretschmann configuration [20, 38, 62-65] (attenuated total reflection [64, 66]). The p-polarized light passes through the prism of known refractive index and is reflected from the thin metal surface. Collimating lenses allow a small dispersion in the value of the input beam angle around the assumed one corresponding to the matching of the momentum of light and plasmonic waves. An evanescent wave is created at the junction of the prism surface and the metal which can interact with the SP waves existing at the metal-dielectric interface. The s-polarized light occurring perpendicular to the plane of incidence cannot excite the electronic plasmonic wave. When the plasmonic wave is created, its related energy disappears in the output beam that is reflected from the metal. That leads to a black spot or line in this output beam that can be detected using a camera.

A variant of this technique is denominated SPRi (i for intensity) where instead of following the shift of the minimum of the plasmonic response over an output angle detection range, the detector only receives the output light in a dedicated angle; the shift in angle is then translated into an amplitude variation.

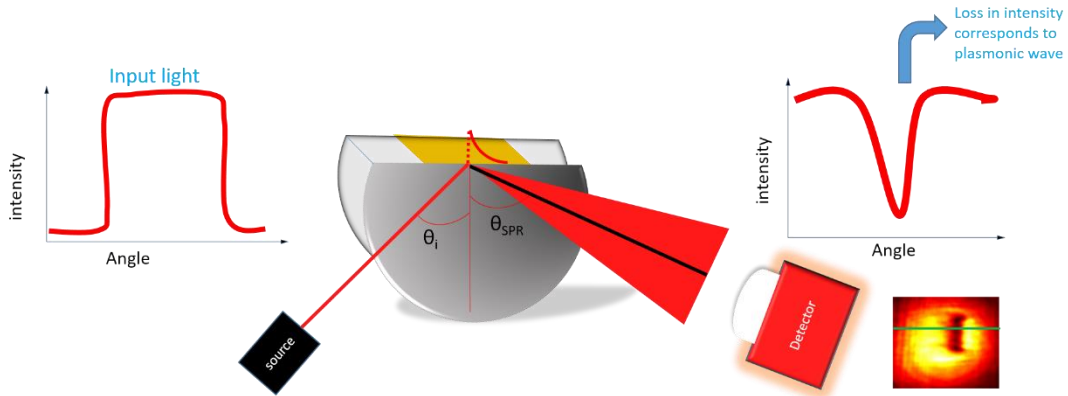


Figure 1.9 Angular interrogation technique: Left shown is the input monochromatic light source passing through the prism block with angle values around  $\theta_i$  to the surface of the metal. At the right, the reflected intensity as it can appear on a CCD camera. The profile of the reflected light exhibits a loss in intensity which corresponds to the matching of input photons to the surface plasma waves and so the creation of the SPP.

### 1.2.2.2 Spectral interrogation

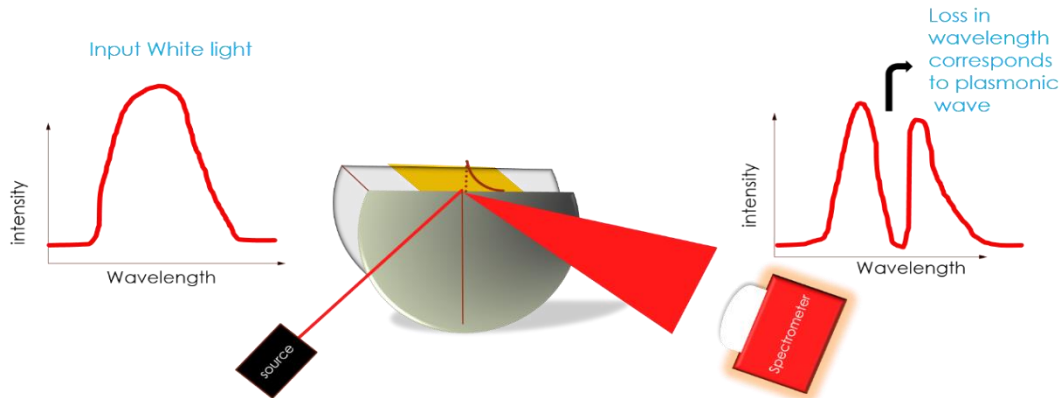


Figure 1.10 Spectral interrogation technique to excite the SP waves. At the left, the input light used is white light made to pass through the prism and reflected from the metal. A spectrometer captures the reflected spectra and the loss of a particular wavelength of the spectra corresponds to the SP wave.

This is almost the reciprocal situation of the angular interaction scheme, using a fixed injection angle the plasmon resonance phenomenon is wavelength and polarization-

dependent [67]. The optical configuration used for the spectral interrogation is similar to that of the previously discussed angular interrogation technique except collimating lenses furnish here a parallel beam. P-polarized polychromatic light is sent through the prism block to the surface of the thin metal and reflected light is detected and analysed by using a spectrometer. Once the momentum of the optical and plasmonic waves matches, there is a loss in the reflected spectra as shown in Figure 1.10.

### *1.2.2.3 Phase interrogation*

In the phase interrogation technique, the transducer part remains the same as compared to the previously mentioned technique. This technique is polarization and phase-dependent [68], so the input polychromatic light source passing through the phase meter is sent to the metal surface and the reflected beam is guided to another phasemeter. Both input and output beam phases are compared and any change reflects a refractive index modification at the sensor surface. But this technique is more complicated than the previous ones and requires more optical components, modulation instruments, and image processing techniques, which make an instrument more expensive.

## **1.3 State-of-art of SPR biosensor**

Most of the biosensors that are in the peak of academic research [69] have also commercial availability; they are based on calorimetry, fluorescence, luminescence, surface plasmon resonance, spectroscopy and electrochemistry. From all these biosensors using optical sensing, SPR has great potential towards label-free bio-sensing that can allow detection without any need of preparation. Surface plasmon resonance (SPR) has become a popular biosensor for its molecular specific detection in a very short time. SPR has drawn enormous attention and found various applications in bio sensing fields. The early research on SPR began 80 years ago when Wood observed the first phenomena and after following the introduction of the first commercial surface plasmon resonance (SPR) instrument (Biacore) in 1990, the number of publications on the topic of SPR biosensors (non-commercial biosensors) are estimated approximately to be around 8750 papers by 2016 as shown in

Figure 1.11 and when the data collected from commercial biosensors the number of publications may increase to more than 20 000 papers by 2016 (PubMed data) [74]. Not only the number of publications but also advances in the technology led to an improvement in detection sensitivity by roughly 100-fold up to  $10^{-8}$  RIU [70] (refractive index unit) or 0.01 RU (response unit that is used on Biacore systems,  $1\text{RU} = 10^{-6}$  RIU).

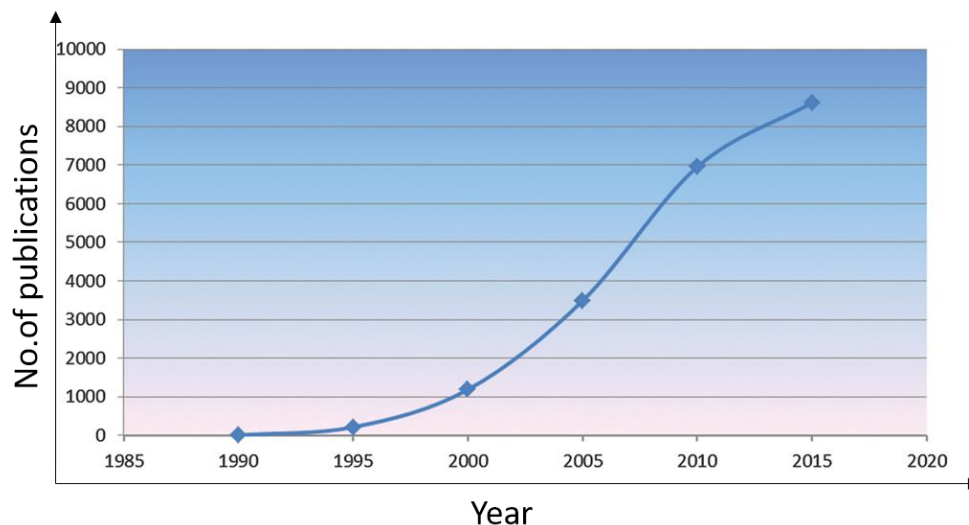


Figure 1.5 Number of publications on the topic of SPR biosensors in a research journal [71].

The classical SPR interrogation schemes that are used for bio-sensing application are angular and wavelength interrogation schemes (see §1.2.2). These interrogation schemes have been developed and can be used to characterize and identify the concentration of chemical and biological samples, based on their interactions with target-specific molecules, such as antibodies, DNA, proteins, enzymes, etc. With the advancement in this interrogation schemes the detection limits are drawn to 5 orders of magnitude better than the other immunoassays [72-74]. And nowadays SPR systems are developed by many industries with many numbers of throughputs and with many inbuilt technologies. Sensitivity is the most important parameter for every bio-sensing technique [75] but, as it will be detailed in chapter 2, one must be aware that the sensitivity of the full detection system is a complex mix between hardware (SPR sensor, SPR detection scheme, SPR optical reading implementation) and software (post-data treatment). So currently research is to improve the sensitivity of SPR by developing different SPR interrogation schemes. For example Phase-sensitive SPR sensors have recently been developed rapidly because of

their high sensitivity and high throughput when compared with conventional intensity-, angle- and wavelength-interrogated SPR systems [68]. Likewise all the research are quite progressive among sensing platforms developments, particularly in its prominent features such as its sensitivity, real-time detection, label-free assay, throughput, portable system and cost efficiency.

### 1.3.1 Academic research on SPR biosensor

The Table 1.3 presents the typical performance of SPR sensors based on angular, spectral and phase interrogation detection schemes [76]. Here the performance of a SPR sensor is given by its resolution and dynamic range. The resolution is given by the smallest change in the refractive index of the sensed medium that produces a detectable change in the sensor output. It is then more especially a characteristic of the whole sensing equipment than only linked to the sensor itself. In SPR the resolution is said as bulk index resolution.

The sensor dynamic range is defined as the highest to the lowest refractive index difference (so the limit of detection (LOD)) that a SPR system can measure. LOD and dynamic range, identically to the sensitivity are characteristics of the whole sensing equipment.

It can be seen that the phase detection scheme offers a better sensitivity but as discussed earlier the phase detection scheme is more complicated than the classical angular or wavelength detection schemes and to setup a phase interrogation SPR system requires expensive optical components, modulation instruments and important image processing technologies and techniques. All these ads up to increase the cost of the system and at the same time it is not easy to make the system portable by integrating this complex optical instrument.

<b>SPR Interrogation techniques</b>	Angular	Spectral	Phase
<b>Resolution</b>	$5 \times 10^{-7}$ RIU	$10^{-6}$ RIU	$4 \times 10^{-8}$ RIU
<b>Dynamic Range</b>	0.1RIU	>0.1RIU	$5 \times 10^{-4}$ RIU

*Table 1.3 Global performance of SPR sensing techniques [69]*

### 1.3.2 Industrial level

Current commercially available SPR sensors, are based on angular or spectral interrogation scheme. Some of the well-known commercial SPR technique companies are Biacore, AutoLab, Biosensing Instrument, ICx Nomadics, Hofmann sensorsysteme, etc. Some of the commercially available SPR instruments and their specification are shown in Table 1.4. We try to get as much as details on available characteristics as possible but only few SPR companies give access to those and so some major companies are not represented in this table.

It can be seen from the Table 1.4, from all the companies only two of them (Biosensing Instruments and Biacore) provides a SPR instrument (BI-4500 and Biacore 8K instrument) with the facility to control the temperature.

Company	P4SPR	Nicoya SPR	Plasmatrix	4SPR Xantec	BI-4500	Affinity instruments	Biacore 8K Instrument Kit	Autolab TWINGLE
Instrument Size(mm)	175X155 X55	460X340X 210	50X150X 32	-	355X250 X515	175X155X 55	-	330X400X 360
Sensor	Au 50nm	Au 50nm	Au 50nm	Au 50nm	Au 50nm	Au 50nm	-	-
Number of channels	4	2	2	4	5	4	16 in 8 channels	2
Power source	USB	-	USB	-	-	USB	100 to 240 V	100 to 240 V
Microfluidic volume ( $\mu$ l)	50	5-100	-	50-4500	10-50	150	20 -50	20-150
Flow rate ( $\mu$ l/m)	-	5-200	-	1-250	1-250	-	1 - 200	30-130
Resolution (RIU)	1 $\mu$	1 $\mu$	1*10 <sup>-6</sup>	1*10 <sup>-8</sup>	<10 <sup>-5</sup>	1 $\mu$	1*10 <sup>-7</sup>	1*10 <sup>-7</sup>
Light source	Polychromatic	polychromatic	650nm	780nm	Polychromatic	-	-	670nm
Software	Labview	Labview	Visual C, Labview	Labview	-	Labview	Biacore 8K Control Software	-
Temperature control	No	No	No	No	6 <sup>0</sup> -50 <sup>0</sup> C	-	4 <sup>o</sup> -40 <sup>o</sup> C	No

Table 1.4 Main characteristics of commercial SPR biosensing systems.

## 1.4 Conclusion

In the context of the BIOSENS project exposed in §1.1.3, a first goal was to investigate angular and spectral detection schemes in order to determine the solution that will be best suited for the integration in a portable equipment. My study was initially based on the results obtained in a previous project within the research group focused on angular detection scheme in the near IR wavelength range (1550nm) [77-80]. I started so working on such a detection system and set up a spectral detection system afterwards. Those two experimental set-ups are described in Chapter 3. Before that, I will describe the modelling approach and results at the sensor level in Chapter 2.

One of the most factor that could affect the sensitivity of a SPR detection system is temperature [81]. The change in the ambient temperature introduces modification in the refractive index of the biological solution that be interpreted as a change linked to a molecular interaction. Some of the commercial available SPR instrument works on the temperature controlled environment but this instruments are bulky and so they are not portable. So targeting this ultimate portable system, it was not envisaged implementing a temperature control system. Moreover, our system shall work on different surface functionalizations, i.e. DNA and proteins that might require the control of temperature of the biological solutions. Chapter 4 describes a novel way we investigated in order controlling and monitoring the temperature of the sensed media by using the plasmonic layer as a localized Joule's heater.

Since a secondary, but not the least, goal for the developed system is to democratize the use of SPR, we investigate optical solutions at sensor level in order either to ease their use either to decrease their cost. For that, polymer optics as well as sensor substrate were investigated and they are described in chapter 5.

Chapter 6 looks back on the use of bi-metallic sensors, i.e. based on a silver-gold plasmonic layer, in order to determine if their use would be beneficial increasing the sensitivity of the system.

Conclusion will sum up main results and give perspectives of the work following the obtained results.



## Chapter 2: THEORY OF SURFACE PLASMON RESONANCE APPLIED TO BIOSENSING

In this chapter, I will briefly introduce the history of plasmons and their mathematical derivations. Further I will focus on the simulation results which are rendered for both angular interrogation and spectral interrogation SPR sensing methods. As result of this modelling activity, I will conclude by giving the rules for the design of SPR sensors in order they will be used for performing the experiments reported in the next chapters.



## 2.1 Theory

This chapter aims to introduce the theory of surface plasmons and their mathematical derivations that can be used for modelling surface plasmon waves. Surface plasmon resonance (SPR) or surface plasmon polaritons (SPP) is the non-radiative electromagnetic surface wave that exists between negative and positive permittivity material [82] (metal-dielectric) which can be stimulated by incident light under certain conditions [83-85]. One of the main conditions is that the incident photon has to match its momentum to that of the plasmon wave [83]. The first method to provide the incident light photons with additional momentum has been discovered and explored by Wood [12, 57], which we have already seen in the previous chapter.

This phenomenon was later described during the 1970's in terms of excitation of electromagnetic evanescent waves at the surface of thin metal to excite the surface waves [58]. However, this phenomenon of exciting plasma waves can be mathematically derived by considering the interaction of the electromagnetic fields at the conducting surfaces [86, 87]. In this case, it is being necessary to understand the electromagnetic properties of the conducting surfaces. Below is shown the derivation of the electromagnetic and dielectric properties of metals that are strictly needed to excite plasma waves at the metal-dielectric interface.

To derive the equation associated with surface plasmon (SP) waves we could begin with Maxwell's equations. Maxwell's equations are the foundation of the electromagnetic theory explaining the creation of the electric and magnetic fields [88]. Here we could begin with the classical Maxwell's equations to understand the surface plasma waves.

Gauss law gives the relation between the electric flux density and the free charge density in a material. It is stated that the strength of the electric flux depends on the number of free charges present in a material.

$$\text{Gauss's law} \qquad \qquad \qquad \nabla \cdot \mathbf{D} = \rho_f \qquad \qquad \qquad 2:1$$

$$\text{Gauss's law for magnetism} \qquad \qquad \qquad \nabla \cdot \mathbf{B} = \mathbf{0} \qquad \qquad \qquad 2:2$$

Gauss's law of induction  $\nabla \times \mathbf{E} = -\frac{\partial \mathbf{B}}{\partial t}$  2:3

Ampere's law  $\nabla \times \mathbf{H} = \mathbf{J}_f + \frac{\partial \mathbf{D}}{\partial t}$  2:4

where  $\mathbf{D}$  is the electric flux density,  $\mathbf{B}$  the magnetic flux density,  $\mathbf{E}$  the electric field,  $\mathbf{H}$  the magnetic field,  $\rho_f$  the free charge density and  $\mathbf{J}_f$  the free current density. For homogeneous, isotropic, and linear dielectric materials,  $\mathbf{D}$  and  $\mathbf{B}$  can be related to  $\mathbf{E}$  and  $\mathbf{H}$  by:

$$\mathbf{D} = \epsilon_0 \mathbf{E} + \mathbf{P} = \epsilon_0 \epsilon_r \mathbf{E} \quad 2:5$$

$$\mathbf{H} = \frac{\mathbf{B}}{\mu_0} - \mathbf{M} = \frac{\mathbf{B}}{\mu_0 \mu_r} \quad 2:6$$

where  $\mathbf{P}$  is the polarization,  $\mathbf{M}$  is the magnetization,  $\epsilon_0$  and  $\mu_0$  are the electric permittivity and magnetic permeability in free space, respectively.  $\epsilon_r$  and  $\mu_r$  are the relative electric permittivity and relative magnetic permeability of the material, respectively. The material permittivity and the permeability are given by:

$$\mu = \mu_0 \mu_r \quad 2:7$$

$$\epsilon = \epsilon_0 \epsilon_r \quad 2:8$$

Deriving from equation 2:3 and equation 2:4, the electromagnetic wave equation in the free space are given in terms of both electric field (Equation 2:9) and magnetic field (Equation 2:10):

$$\nabla^2 \mathbf{E} - \frac{\epsilon_r \mu_r \partial^2 \mathbf{E}}{c^2 \partial t^2} = \mathbf{0} \quad 2:9$$

$$\nabla^2 \mathbf{B} - \frac{\epsilon_r \mu_r \partial^2 \mathbf{B}}{c^2 \partial t^2} = \mathbf{0} \quad 2:10$$

Where  $\nabla^2$  is the Laplace operator,  $C$  is the speed of light in vacuum  $\left(c = \frac{1}{\sqrt{\epsilon_0 \mu_0}} = 2.99792458 \times 10^8 \text{ m/s}\right)$ ,  $B$  is perpendicular to  $E$  and both are perpendicular to the direction of the propagation.

Let's assume that all materials used in this discussion are non-magnetic with a relative permeability  $\mu_r = 1$ . Then the relative permittivity and refractive index of the materials, which are complex quantities, are given by Equation 2:11 and Equation 2:12 respectively:

$$\boldsymbol{\epsilon}_r = \boldsymbol{\epsilon}_1 + i\boldsymbol{\epsilon}_2 \quad 2:11$$

$$\boldsymbol{n}_r = \boldsymbol{n}_1 + i\boldsymbol{n}_2 \quad 2:12$$

Where  $\epsilon_1$  and  $\epsilon_2$  are the real and imaginary components of the permittivity of the material respectively.  $n_1$  and  $n_2$  are the real and imaginary components of the refractive index of the material respectively. From here we aim to use the material for optical bio-sensing purposes it will be encouraging to relate the material electromagnetic property with the refractive index of the material and also its optical properties so further we could use this property for the optical bio-sensing application. Firstly, the relationship between permittivity and refractive index of the material can be found in the following equations:

$$\boldsymbol{n}_r = \sqrt{\boldsymbol{\epsilon}_r} \quad 2:13$$

$$\boldsymbol{\epsilon}_1 = \boldsymbol{n}_1^2 + \boldsymbol{n}_2^2 \quad 2:14$$

$$\boldsymbol{\epsilon}_2 = 2\boldsymbol{n}_1\boldsymbol{n}_2 \quad 2:15$$

Till here we have seen the electromagnetic properties of the material. From here let us derive the optical properties of the material as we aim to excite the plasmon at the metal-dielectric interface using photons. To answer the question of what is plasma, we rely on the Drude's model of electrical conductivity [89-91].

The Drude's model proposed in 1900 [92] by Paul Drude assumes that the metal is formed by a lattice of positive charge ionic cores with negatively charged gas. The negatively charged gas is formed by an ensemble of electrons moving freely inside the metal and is also called plasma. This model is used to describe the optical properties of a metal [93, 94]. If a volume of plasma is displaced by a distance,  $x$ , it results in polarization,  $P$ . This leads to the formation of an electric field,  $E$ , with the following relationship:

$$E = \frac{-P}{\epsilon_0} = \frac{nex}{\epsilon_0} \quad 2:16$$

Where  $n$  is the electron density and  $e$  the electronic charge. The Drude's model only considers electron motion damping from the collisions, represented by the mean free time  $\tau$ , between collisions.

When there is a collision between objects that are in motion, then it is necessary to consider its acceleration force and its frictional force during collision then the equation of motion of a free electron can be written as:

$$m \frac{d^2x}{dt^2} + m \frac{1}{\tau} \frac{dx}{dt} = -eE = -\frac{ne^2x}{\epsilon_0} \quad 2:17$$

Where  $m \frac{d^2x}{dt^2}$  is the acceleration force,  $m$  the electron mass.  $m \frac{1}{\tau} \frac{dx}{dt}$  is the frictional force due to collisions and as a result, these collision energies are in the form of electric force which is given in the term  $-eE$ .

A description of the time-dependent electric field is given in Equation 2:18, and the oscillation of the electron response as a function of time is given in Equation 2:19:

$$E(t) = E_0 e^{-i\omega t} \quad 2:18$$

$$x(t) = x_0 e^{-i\omega t} \quad 2:19$$

Substituting into the motion equation presented in Equation 2:17 we obtain:

$$x_0 = \frac{e}{m(\omega^2 + \frac{1}{\tau}i\omega)} E_0 \quad 2:20$$

Since  $P = -nex$  (Equation 2:16), we can rewrite Equation 2:20 as:

$$P = -\frac{ne^2}{m(\omega^2 + \frac{1}{\tau}i\omega)} E \quad 2:21$$

Substituting this description of  $P$  into the relation for  $D$  in Equation 2:5 we obtain:

$$D = \epsilon_0 \left( 1 - \frac{ne^2}{\epsilon_0 m (\omega^2 + \frac{1}{\tau}i\omega)} \right) E \quad 2:22$$

The natural frequency of oscillation of electron in a metal associated with the plasma is known as the plasma frequency and it is defined as:

$$\omega_p = \sqrt{\frac{ne^2}{\epsilon_0 m}} \quad 2:23$$

Where  $\omega_p$  is the plasma frequency.

Then Equation 2:18 changes into:

$$D = \epsilon_0 \left( 1 - \frac{\omega_p^2}{\omega^2 + \frac{1}{\tau}i\omega} \right) E \quad 2:24$$

From the comparison between Equation 2:5 and Equation 2:24, the relative permittivity of metal can be written in terms of its plasma frequency as follows:

$$\epsilon_r = 1 - \frac{\omega_p^2}{\omega^2 + \frac{1}{\tau}i\omega} \quad 2:25$$

And the real and imaginary components of  $\epsilon_r$  are:

$$\epsilon_1 = 1 - \frac{\omega_p^2 \tau^2}{1 + \omega^2 \tau^2} \quad 2:26$$

$$\epsilon_2 = \frac{\omega_p^2 \tau}{\omega(1 + \omega^2 \tau^2)} \quad 2:27$$

Below the plasma frequency, the dielectric function is negative and the field cannot penetrate the sample meaning that for angular frequencies,  $\omega$ , below the plasma frequency ( $\omega < \omega_p$ ), the permittivity of the metal is negative and the metal is reflective. At frequencies above the plasma frequency ( $\omega > \omega_p$ ), the permittivity is positive and the metal becomes mainly absorbing or the light waves can penetrate the metal. From this analysis, it is found that for SPR to take place, and the plasmon to propagate along with the interface in the form of an evanescent wave, the incident field must be a TM wave or p-polarized. In this type of polarization, the electric field is parallel to the incidence plane, and thus the magnetic field perpendicular to it.

Furthermore, the continuity conditions establish that for the evanescent waves to exist, it is required for the two materials in the interface to have dielectric functions of opposite signs, for example metal and fluid interface or metal and air interface.

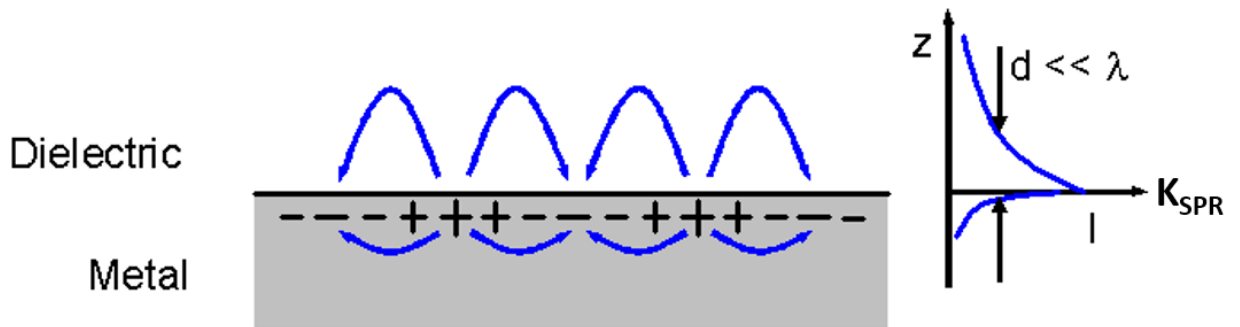


Figure 2.1 Schematic representation of a surface wave (surface plasmon polariton) propagating along with a metal-dielectric interface.

A metal-dielectric interface satisfies this condition, since metals have a large negative real part of their dielectric function, while for dielectric materials this property is positive. From Figure 2.1 the wave amplitude away from the surface dies off exponentially (right-hand graph) and those fields are thus described as evanescent waves in the z-direction.

Solving the wave equation for TM-waves incident at a metal-dielectric interface leads to the fundamental SPR equation, relating the properties of material with the frequency/wavelength of the light (dispersion relation):

$$K_{spr} = K_0 \sqrt{\frac{\epsilon_d \epsilon_m}{\epsilon_d + \epsilon_m}} \quad 2:28$$

Where  $K_{SPR}$  is the surface propagation constant of the plasmonic wave along with the interface (x-axis),  $K_0$  is the wavenumber given by  $K_0 = \frac{2\pi}{\lambda}$ ,  $\epsilon_d$  the permittivity of the dielectric medium and  $\epsilon_m$  the permittivity of the metal. Nevertheless, incident light cannot be directly coupled with the surface plasmon to produce resonance (see Figure 2.3), it is necessary to match the propagation constants of the incident light and the surface plasmon through an excitation scheme.

The first method to match those propagation constants has already been described by Wood [83]: a periodic corrugation in a metal surface can diffract incident light into the plane of the metal-dielectric interface, resulting in the resonant coupling of light with surface plasmons. The schematic illustration of this method is shown in Figure 2.2a).

The second most common excitation method is based on prism coupling as shown in Figure 2.2b) (total internal reflection (TIR)). This excitation method can be applied in two different configurations. The first configuration is known as the Otto configuration [85], where there is a gap between the metal and the TIR surface. The gap is filled with a lower refractive index medium, which can be useful in the study of SPR in solid phase media [95]. However the gap reduces the SPR efficiency, it is less useful for applications using fluidic media (biological solutions). For the applications with solutions the most common method used is Kretschmann's configuration, which is also based on attenuated total reflection (ATR). In this configuration the metal is directly coated on the TIR surface (prism) and the photons are made incident on the metal surface. In total internal reflection (TIR), the reflected photons create an electric field on the opposite side of the metal-dielectric interface and the surface plasmons are excited at the metal-dielectric interface showing a sudden dip in the light reflectance.

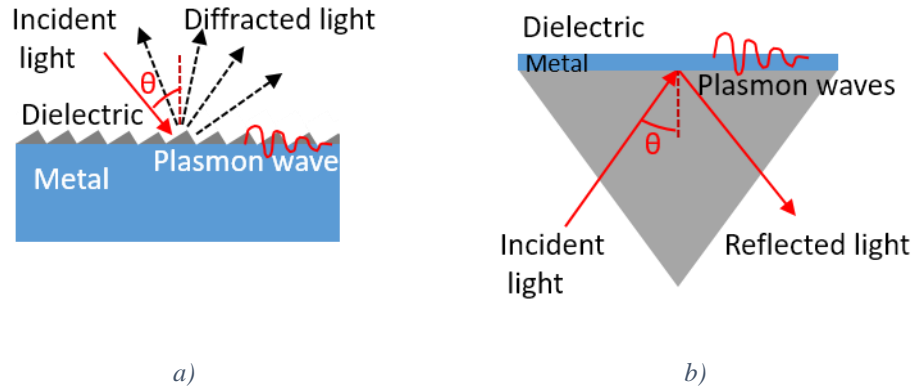


Figure 2.2 Plasmon excitation a) using diffracted grating (Wood's experiment). b) classical Kretschmann's configuration.

Although prism coupling is the most commonly used technique for SPR sensing, the basic principle of this method is the same as grating coupling where the propagating surface plasmons at the interface of metal and dielectric react to changes of the refractive index of the dielectric medium, resulting in detectable changes in the reflected light for a given angle, as adsorption occurs on the metal surface. This results in a shift in the effective refractive index at the metal surface. This physical principle is used as a biosensor.

The need of using prism is shown in Figure 2.3. Without the prism, the dispersion relation of the incident light, propagating in air, is represented by a black solid line and given by the x-component of the wave vector  $k_x = k_0 \sin \theta$ . On the other hand, the dispersion relation derived as shown in the Equation 2:28 for the metal-dielectric interface is represented by a red solid line. As can be seen, these lines do not intersect at any point, meaning that the incident light in air cannot excite surface plasmon. However, when light passes through a prism having an optical refractive index of  $n_p$ , the dispersion relation of light, which is shown as a black dashed line, intersects the metal-dielectric interface dispersion relation. In that case, the x component of the wave vector of incident light is given by  $k_x = k_0 n_p \sin \theta$  at the point where both curves intersect, shown by a grey dot in the Figure 2.3; the resonance condition is then achieved.  $n_p$  being the refractive index of the prism, the propagation constant of the incident light in the prism can be obviously modified by changing the refractive index of the prism. The influence of the refractive index of the prism on the plasmonic angle is discussed in the following section but can be simply

overviewed on Figure 2.3 under the blue dotted-dashed curve exhibiting another possible resonance condition.

Thus, for SPR to be excited under Kretschmann’s configuration the following relation must be met:

$$K_x = \frac{2\pi}{\lambda} n_p \sin\theta = \text{Re} \left( K_0 \sqrt{\frac{\epsilon_d \epsilon_m}{\epsilon_d + \epsilon_m}} \right) \quad 2:29$$

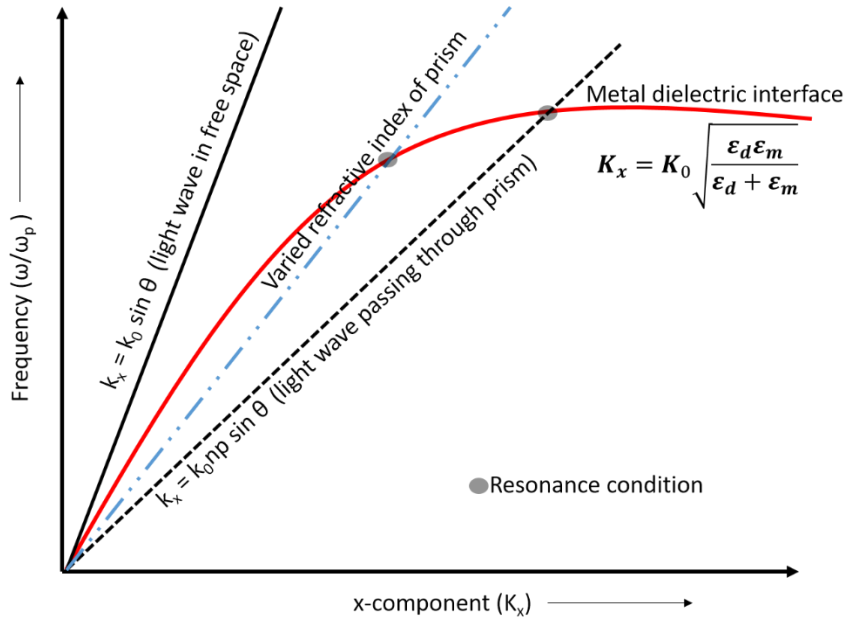


Figure 2.3 Dispersion relation for SPPs: the solid black line represents the light wave in free space, the black dashed line the light wave passing through a prism and the blue dotted-dashed line the light wave passing through a prism with a different refractive index. The red solid curve is the dispersion curve of surface plasmons at the metal-dielectric interface. The black dots represent the resonance conditions.

As can be seen from Equation 2:29, the plasmonic response can be altered by either the wavelength or the refractive index of the prism. To model the plasmonic response, a Matlab code was used. It has been then possible to determine the effects of the prism optical refractive index, of the thickness of the metal constituting the plasmonic layer, of the incidence angle and of the wavelength on the plasmonic response. The following paragraph will present this plasmonic response model and its application to both the angular and spectral interrogation methods.

## 2.2 Performance of a plasmonic sensing technique

The performance of a SPR sensor can be given by its sensitivity, resolution, limit of detection, and dynamic range [96]:

- The sensitivity,  $S_{opt}$ , is given by the ratio of change in the optical output signal (angle in degrees,  $\Delta\theta$ , or wavelength in nm,  $\Delta\lambda$ , for angular and spectral interrogation scheme, respectively) per change in the refractive index ( $\Delta n$ ) of the sensed medium. Change in refractive index is often referred in refractive index unit (RIU), 1 RIU being a refractive index difference of 1. For angular interrogation and spectral interrogation schemes, the sensitivity of the biosensor is then given in degree  $^{\circ}$ /RIU and wavelength nm/RIU, respectively.
- The resolution is given by the smallest change in the refractive index of the sensed medium that produces a detectable change in the sensor output. It is then more especially a characteristic of the whole sensing equipment than only linked to the sensor itself. So the resolution is lowest sensor out's lower limit that can detect a small change is set by the level of uncertainty in the sensor output (noise in the instrument). In SPR the resolution is said as bulk index resolution.
- The limit of detection (LOD) is almost well described by its composing words; it corresponds to the lowest refractive index difference the sensor can detect. Here too, it is almost a characteristic of the whole sensing system that is linked to the noise level in the detection circuit (optics, electronics). It is commonly evaluated as 2 or 3 times [97-99] the measured noise level of the system.
- The sensor dynamic range is defined as the highest to the lowest refractive index difference (so the LOD) that a sensor can measure. As for the LOD, it is also a limitation of the whole sensing equipment.

So, the only characteristic that is only dependent on the sensor itself is the sensitivity. It has also to be noticed that all other characteristics are strongly dependent on the data treatment that is done on the raw SPR measurements results. It is then difficult to compare

these values from one system to another since both hardware and software solutions that are implemented will modify the results.

In order to evaluate the sensitivity, the above mathematical equations were used to model the plasmonic responses using a Matlab code. Both angular interrogation and spectral interrogation methods were modeled and respective results are shown and discussed further.

We introduce a figure-of-merit (FOM) for the plasmonic response and so the sensor performance [96, 100, 101] that is defined as the ratio of sensitivity to the FWHM of the response:

$$FOM = \frac{S_{opt}}{FWHM} \quad 2:30$$

## 2.3 Modelling of the SPR

### 2.3.1 Influence of the refractive index of coupling optics

The influence of prism material (refractive index) and wavelength on the plasmonic resonance angle is shown in Figure 2.4. Resonance angle is defined as the incident light beam angle for which the minimum of intensity is obtained on the reflected beam. The light intensity reflected to the detector is calculated by using Fresnel's equation for a multi-layer system. For the near infrared wavelength range (from 800nm to 1550nm), a prism refractive index below 1.345 cannot excite plasmon since incident light beam is almost parallel to the plasmonic layer surface. In the visible wavelength region from 450nm to 800nm, the minimum prism refractive index value is much more dependent on the used wavelength. It has to be noticed that the wavelength-angle correspondence is also slightly depending on the thickness of metal that is used as the plasmonic layer. In Figure 2.4, the plasmonic layer was 35nm thick and made of Au.

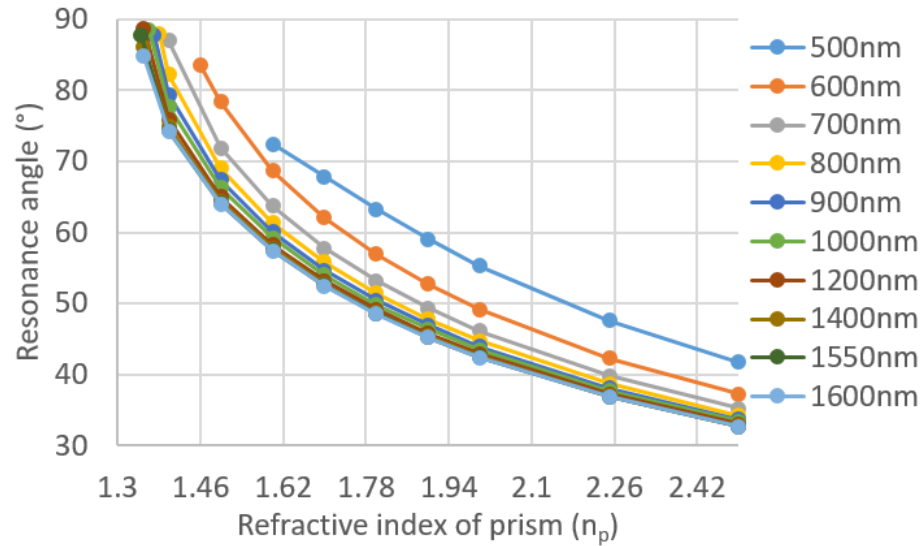


Figure 2.4 Relationship between prism material refractive index and resonance angle for various wavelengths (plasmonic layer is 35 nm-thick gold).

For the subsequent modelling, we fix the prism refractive index to that of H-ZF1 glass (e.g. 1.62 at 1550nm wavelength [102]) since the experimental set-up (angular interrogation scheme) I started working on was effectively using a coupling prism made of this material.

### 2.3.2 Influence of plasmonic layer thickness

For this study, we considered an angular interrogation scheme at 1550 nm wavelength. The plasmonic layer is composed of gold. Its thickness was varied up to 50nm and the plasmonic responses were calculated considering water (refractive index of 1.3180 at 1550 nm) [103] as a dielectric medium (Figure 2.5). The resonance angle decreases when the thickness of the metal Au is increased but it tends to converge around 56.2° for the thicker films. Also, the full width at half maximum (FWHM) of the response curve is larger for the smallest thickness, i.e. 25nm. The variation of the FWHM of the plasmonic response for various metal thicknesses is discussed below.

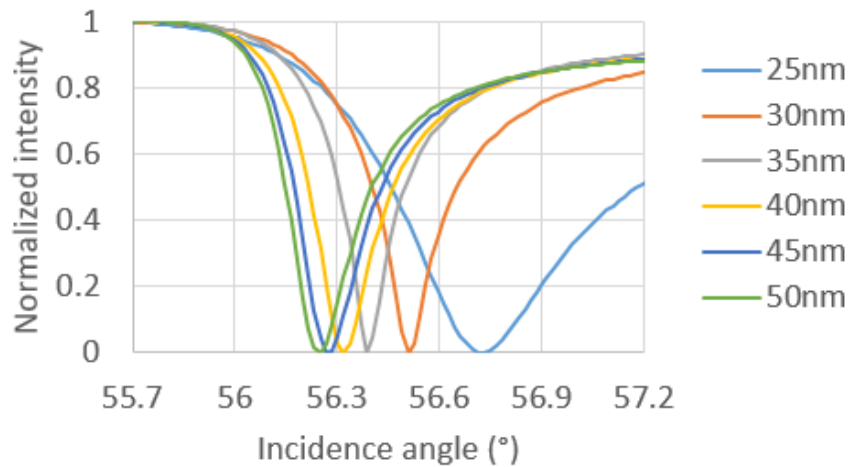


Figure 2.5 Calculated plasmonic responses versus varying thickness of the plasmonic layer (Au). Sensed medium has been here taken as water.

When continuing increasing the plasmonic layer thickness above 50 nm, it is noticed that the resonance angle effectively modifies slightly (see Figure 2.7) but the contrast of the response drastically decreases. Up to a thickness value of 85nm, the contrast is mainly affected by the decrease of the maximum value ("white level") of the response intensity (Figure 2.6a). Between 85 and 100nm, this is mainly the intensity value at the resonance peak ("dark" value) that increases (Figure 2.6b, see also Figure 2.8).

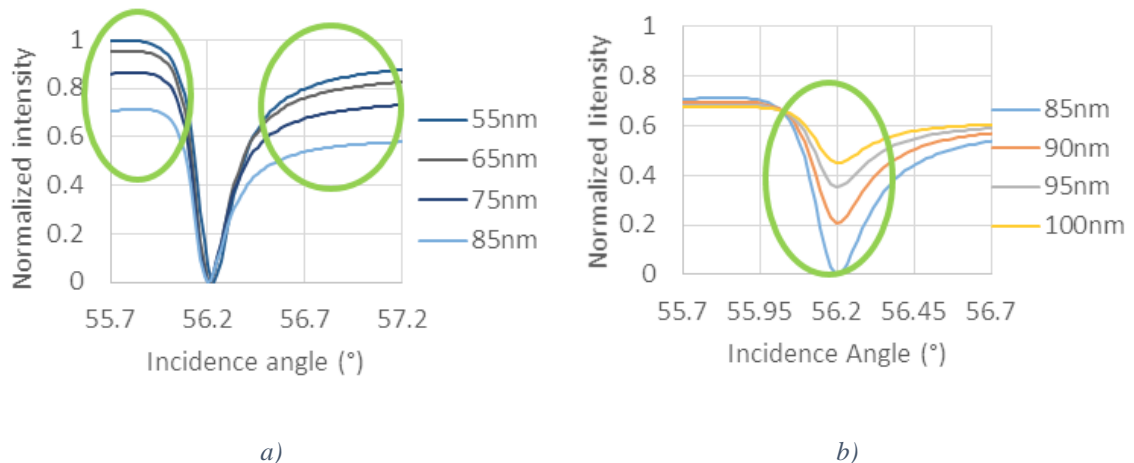


Figure 2.6 Calculated plasmonic responses for varying thickness of the plasmonic layer (Au) above 50 nm. The green circles indicate the reduction of contrast that is then appearing up to thickness value of a) 85nm and b) 100nm. .

Figure 2.7 resumes the evolution of the resonance angle (Figure 2.7a) and the "black level" of the plasmonic response (Figure 2.7b) when increasing the plasmonic layer thickness and represents then how the properties of the plasmonic response is altered when sensor thickness varies, i.e. what can be observed in practical case depending on the fabrication process variability.

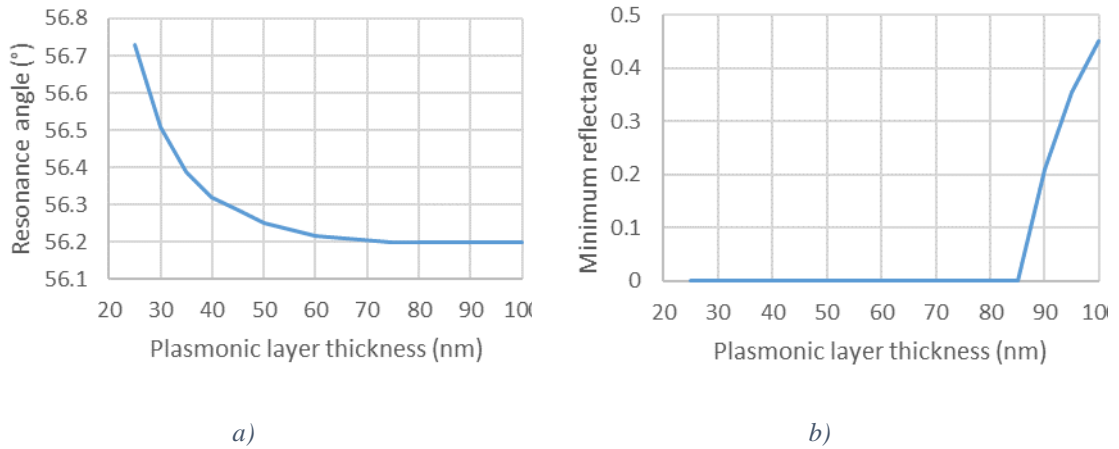


Figure 2.7 Evolution of a) resonance angle and b) minimum reflectance value versus thickness of plasmonic layer (Au).

Figure 2.8 shows the sensitivity of the sensor that was calculated for different thicknesses of the Au plasmonic layer. In this calculation, the refractive index at the sensed medium was varied by  $0.928 \times 10^{-4}$  RIU that corresponds to the refractive index difference between water and 1% ethanol-glycol solution.

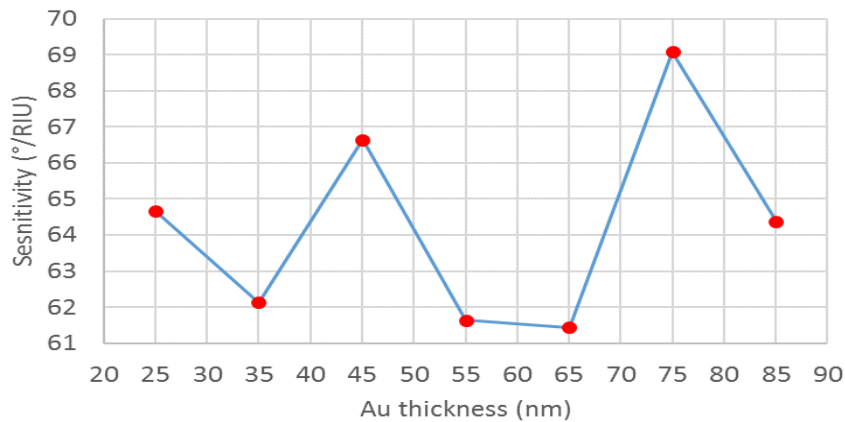


Figure 2.8 Calculated sensitivity of sensor versus gold layer thicknesses (angular interrogation scheme @ 1550 nm, H-ZF1 coupling material).

From the modelling, it is found that using 75nm thickness of the plasmonic layer could provide the highest sensitivity. Nevertheless, referring to Figure 2.6a, the response contrast has already decreased for that thickness. A 45nm-thick plasmonic layer (Au) provides a just slightly lower value and will be then preferred for practical implementation since the contrast of the response is not affected. The sensitivity is calculated to be close to  $69.085^{\circ}/\text{RIU}$  and  $66.637^{\circ}/\text{RIU}$  for 75nm- and 45nm-thick metal layer, respectively. It can also be noticed that there is little evolution of sensitivity value when the film thickness changes, this is also an asset for practical cases where fabrication variability can modify a little bit the film thickness from one fabrication batch to another.

Figure 2.9a) shows the calculated FOM for metal thickness from 25 up to 100 nm. As the sensitivity was almost constant with metal thickness, FOM value is mainly reproducing the FWHM behaviour (Figure 2.9b)). The smallest FWHM value,  $0.191^{\circ}$ , is obtained for a 35 nm film thickness. So highest FOM value is obtained for 35nm.

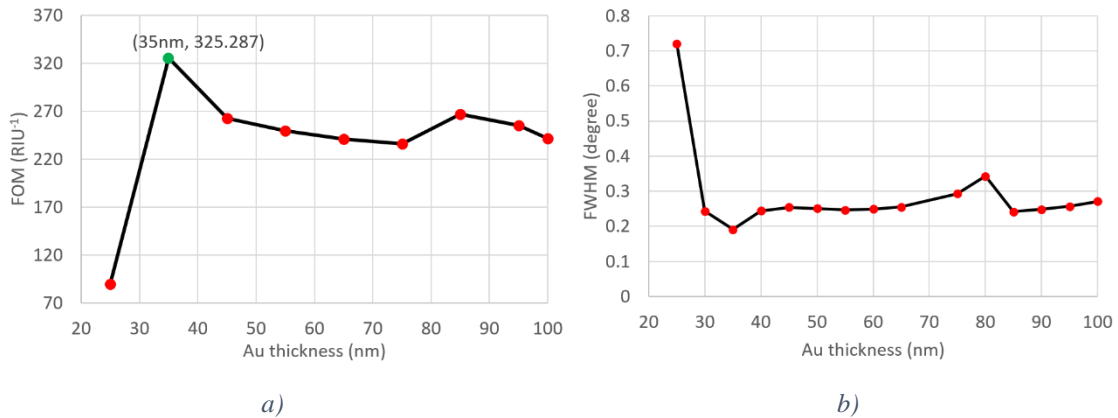


Figure 2.9 a) Calculated FOM of sensor and b) FWHM of the plasmonic curves versus plasmonic layer thickness.

### 2.3.3 Influence of wavelength

In the previous paragraph, interrogation beam was at 1550 nm wavelength. Hereby we modelled the effect of wavelength tuning on the sensor plasmonic response. Figure 2.10 reports the effect of such a wavelength tuning on the sensor response (that is still composed of a 35nm-thick Au film). In practical cases, wavelength variation can be due to the temperature dependence of the optical source but only small variations (up to some tens of

nm) should be taken into account [104, 105]. Nevertheless, in this modelling we made a huge variation of wavelength. It can be first noticed that for "small" variations of wavelength, i.e. between 1500 and 1600nm, the plasmonic response varies slightly, as well as the FOM (Figure 2.11). Nevertheless, it can be noticed that the FOM value varies greatly at 1400nm. That is to say that if one wants maximizing the FOM value, plasmonic layer thickness shall be fitted to operation wavelength.

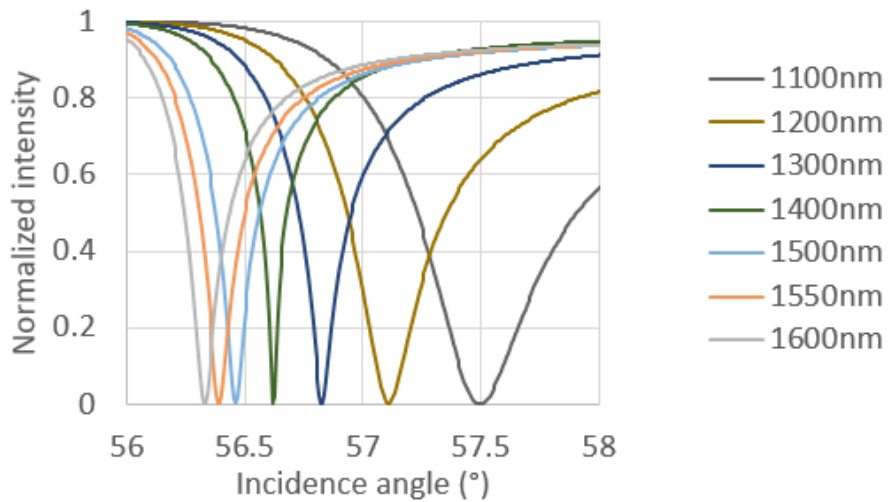


Figure 2.10 Calculated sensor response for varying wavelength from 1100nm to 1600nm Sensor is made of a 35nm-thick layer.

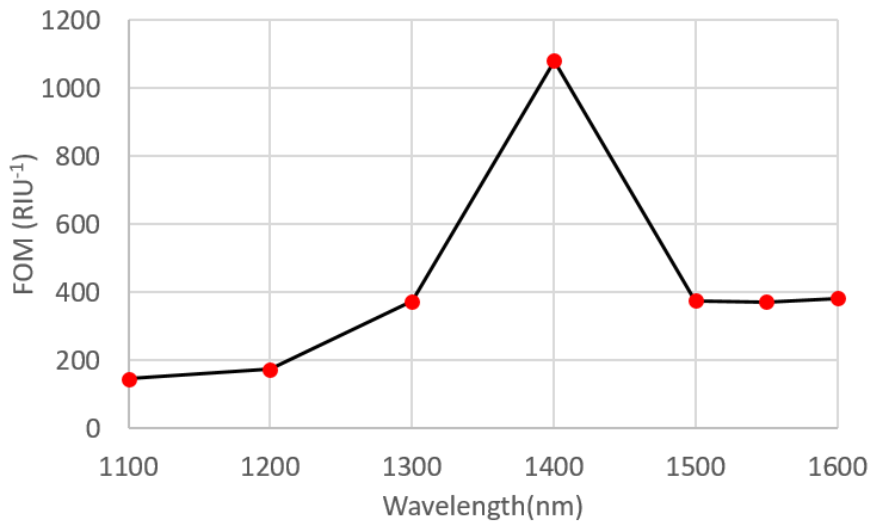


Figure 2.11 Calculated FOM of a sensor with a 35nm-thick Au plasmonic layer versus wavelength (in near infrared region).

### 2.3.4 Matching plasmonic layer thickness to interrogation wavelength

The above study has been replicated for interrogation wavelengths starting in the visible range and reaching the near-IR one. Commonly, visible wavelengths are used for SPR systems since they ease the system implementation and minimize its cost, mainly by the use of lower cost detection systems. Here we compared the sensitivity that is obtained on the 500 nm to 1600 nm wavelength range for different values of plasmonic layer film thickness.

Sensitivity of the SPR system was calculated like previously by calculating the shift of the plasmonic response peak versus changes in sensed refractive index. This was reiterated for various wavelength from visible to near infrared range (Figure 2.12).

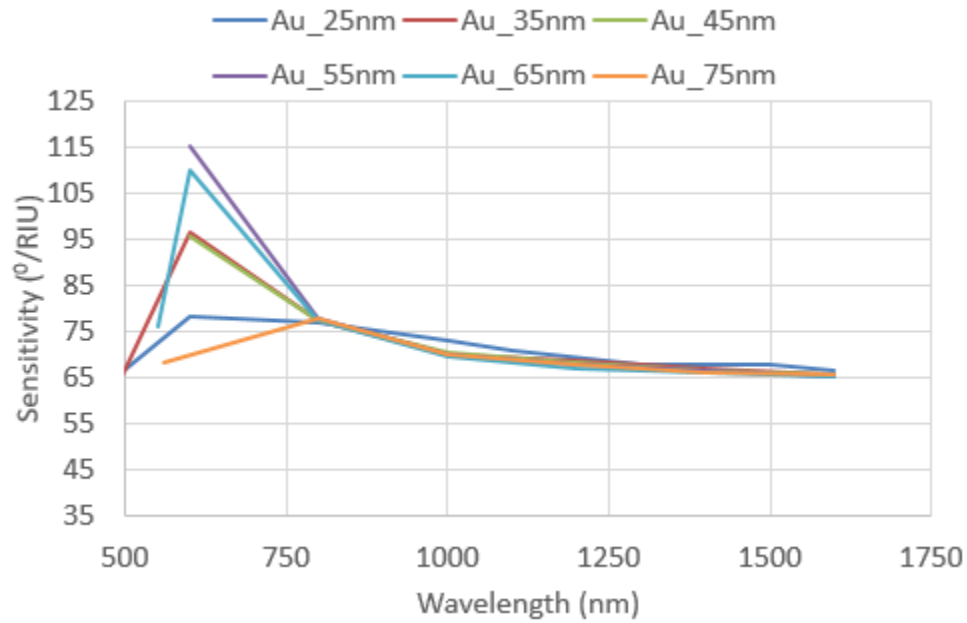


Figure 2.12 Calculated sensitivity of the system depending on wavelength for different metal (Au) thicknesses.

From Figure 2.12, it is seen that the sensitivity of the system in the visible wavelength range is dependent from the metal layer thickness, it can range roughly values as  $90 \pm 20$  °/RIU. A thickness around 50 nm seems achieving higher sensitivity. In the near-IR wavelength range, the sensitivity is almost independent of plasmonic layer thickness. Obviously, this result is a general trend and more fitted calculations shall be done depending on the experimental conditions that are envisaged.

### 2.3.5 Spectral interrogation

As mentioned in chapter 1, spectral interrogation scheme is almost the dual implementation of angular interrogation scheme. Here the angle is fixed but a wide spectrum source is used. The SPR phenomenon appears then as a dip in the output spectrum. The model presented above can easily be tuned to simulate this spectral interrogation scheme. We present modelling results in the visible wavelength range since it corresponds to that of the bench that has been implemented. We kept the same coupling prism made of H-ZF1, its refractive index of 1.639 in the visible wavelength region. First, we investigate the effect of the Au film layer thickness (Figure 2.13) (water is still used as sensed medium and incident beam angle was modified in order to get the resonance peak at same wavelength, or so). The corresponding values of FWHM are given in Figure 2.14.

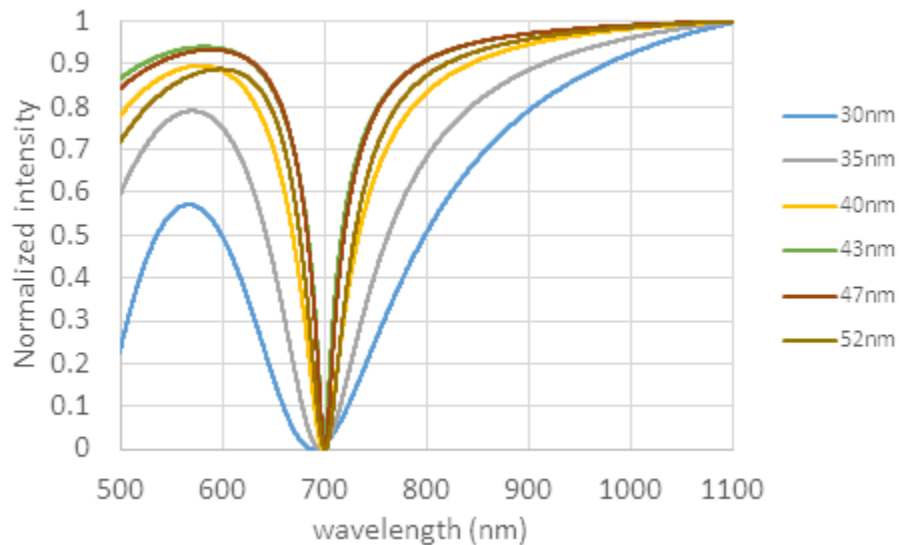


Figure 2.13 calculated plasmonic responses versus thickness of the plasmonic layer (Au). Sensed medium has been here taken as water.

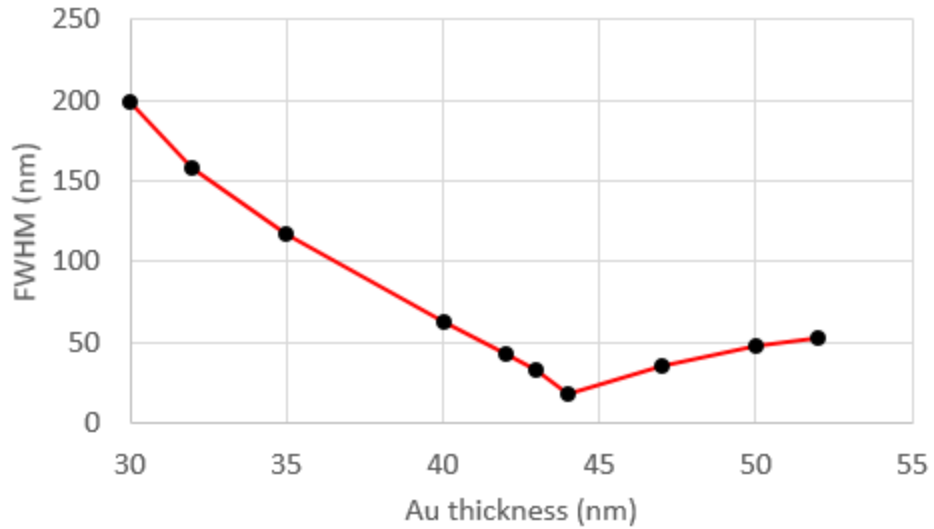


Figure 2.14 Calculated FWHM of the plasmonic response for various thickness of the plasmonic layer (here: Au).

The sensitivity of the sensor has been determined by modelling the plasmonic responses for different solutions of diluted ethylene glycol as sensed medium (Figure 2.15). The incident angle was varied corresponding to the gold thickness that were tuned from 30 nm to 52 nm.

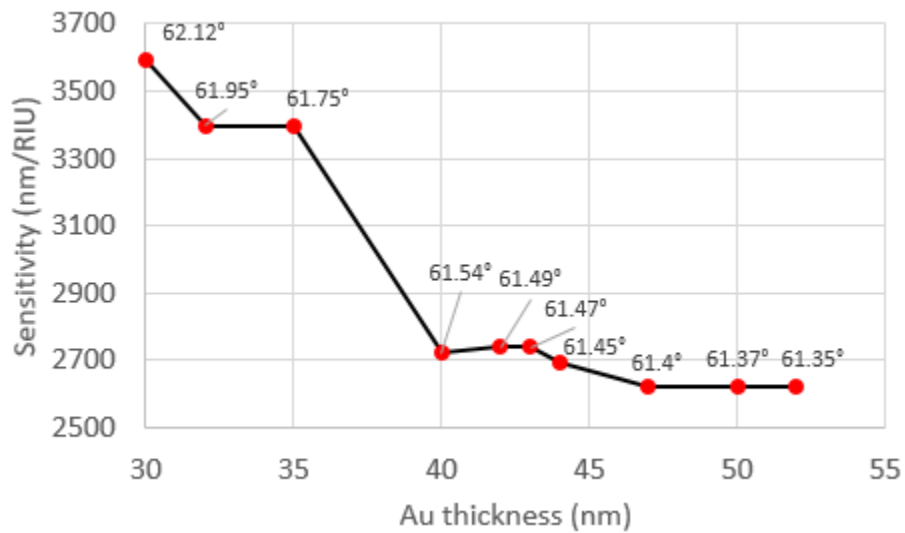


Figure 2.15 Sensitivity versus metal thickness.

From sensitivity and FWHM values, FOM has been calculated (Figure 2.16). It is seen that the FOM curve exhibit a peak for plasmonic layer thickness around 45nm. However, we

must keep in mind that overall SPR system performance will be the combination of hardware and software solutions and some conclusions that can be drawn at this sensor level could be modified at global level.

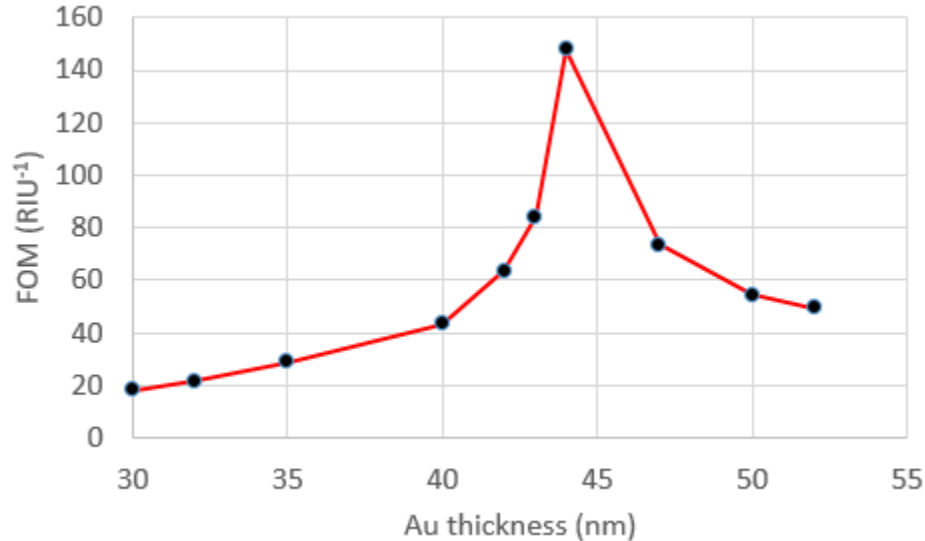


Figure 2.16 Calculated FOM versus metal thickness.

### 2.3.6 Influence of plasmonic layer composition

In above modelling, we considered the plasmonic layer as entirely made of gold. Here we will present some results about a bi-metallic variant, i.e. made of silver and gold. Silver is often presented as exhibiting better plasmonic properties than gold [78, 106, 107] but it cannot be used as it since it oxidizes quickly especially when liquid solutions are used, which is the case in bio-sensing. We modelled so the behaviour of a sensor whose metallic layer is composed by a silver film protected by a gold film.

Plasmonic wave is characterized by two main parameters that are the penetration depth ( $\delta$ ) and the propagation length ( $L$ ) of the evanescent wave into the metal and the dielectric medium. For sensing application, the main important characteristic is the penetration depth within the sensed medium. One can think that higher the penetration of the evanescent wave into the dielectric medium is higher the sensitivity of the system will be. Nevertheless, we must be cautious about that since, in the case of biomolecular interaction monitoring that uses surface functionalization protocols, the relevant data is located just at

very close neighbouring of the sensor surface. Exhibiting a too huge penetration depth can then more or less partly mask the surface refractive change by the bulk refractive of the medium under test. Both parameters depend on the metal and the wavelength that are used for sensing as the relative electric permittivity of the metal depends on the wavelength. As an example, those parameters have been calculated and reported for both plasmonic metals Au and Ag for fluid (water) (Figure 2.17a) and air (Figure 2.17b) refractive index values.

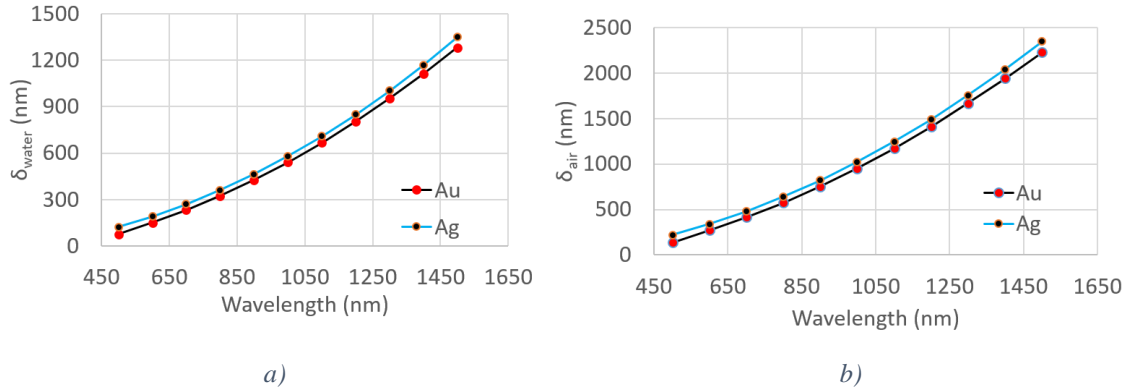


Figure 2.17 Penetration depth ( $\delta$ ) of plasmonic wave into the dielectric medium as function of wavelength a) for water refractive index b) for air refractive index (Au and Ag thickness is 35nm).

From Figure 2.17, it can be seen that the penetration depth of the evanescent wave into the dielectric medium (air and water) is slightly higher by using silver as plasmonic layer. Same remark can be made for the propagation length (Figure 2.18).

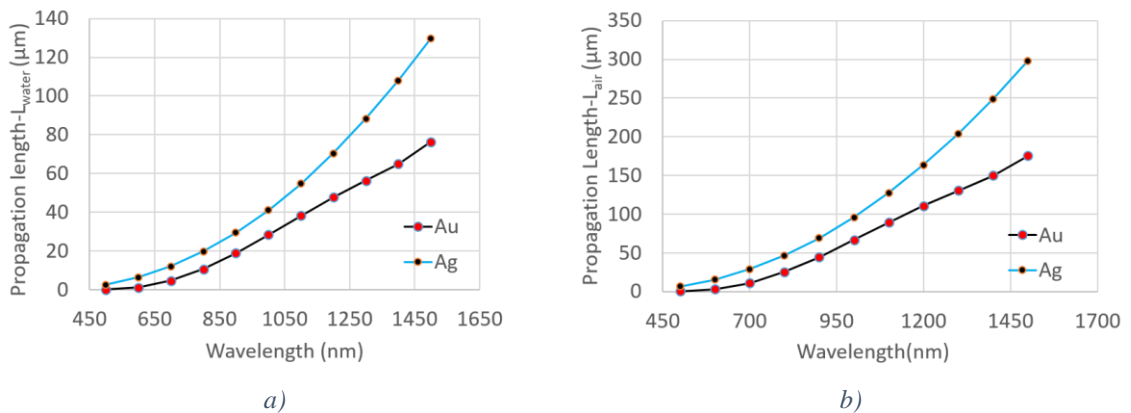


Figure 2.18 Propagation length ( $L$ ) of plasmonic wave as function of wavelength a) for water refractive index b) for air refractive index (Au and Ag thickness is 35nm).

Even if there is few interest knowing it for practical matters, Figure 2.19 shows the penetration of the plasmonic wave into the plasmonic layer made of Ag or Au (35 nm

thick). One thing to be noticed is that penetration depths in sensed medium and metal are balance, i.e. higher it is in sensed medium, lower it is in metal and vice-versa.

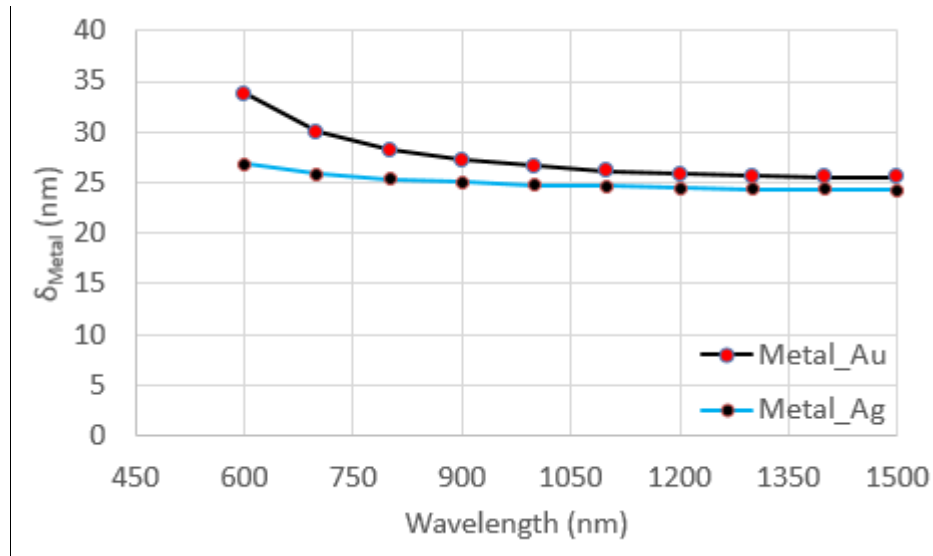


Figure 2.19 Penetration depth ( $\delta$ ) of plasmonic wave wavelength into the plasmonic layer metal (35nm-thick Au or Ag layer).

Plasmonic response was calculated for both interrogation schemes, angular and spectral. Same parameters as for above modelling were used, i.e. for 1) angular interrogation scheme: 1550nm monochromatic light source and H-ZF1 coupling prism having refractive index value of 1.62 and 2) spectral interrogation scheme: wide spectrum (500nm to 900nm) light source and same prism exhibiting a mean refractive index value of 1.639 in this wavelength range. Sensed medium is water. As an example, we only report here the results obtained for angular interrogation scheme.

Figure 2.20 shows the sensor response for different top gold layer thicknesses keeping the silver layer thickness constant and equal to 30nm. It can be particularly noticed that the beneficial effect on FWHM narrowing brought by silver quickly disappears as soon as gold surface layer is used. For 10 nm gold layer thickness, the effect of response FWHM narrowing due to silver has almost vanished.

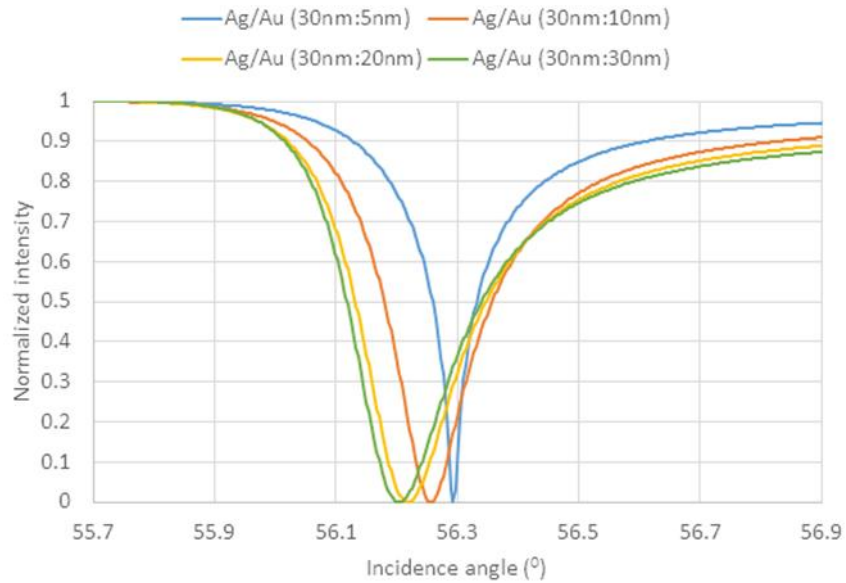


Figure 2.20 Modelling results of SPR curves for different thickness of gold when the silver thickness is kept constant.

In the next plot (Figure 2.21), the gold film thickness was kept constant to 30 nm and the silver film thickness was varied. Here the lowest FWHM value is  $0.185^\circ$  for the combination Ag/Au 5nm:30nm to be compared to  $0.071^\circ$  obtained for the Ag/Au 30nm:5nm configuration (on Figure 2.20).

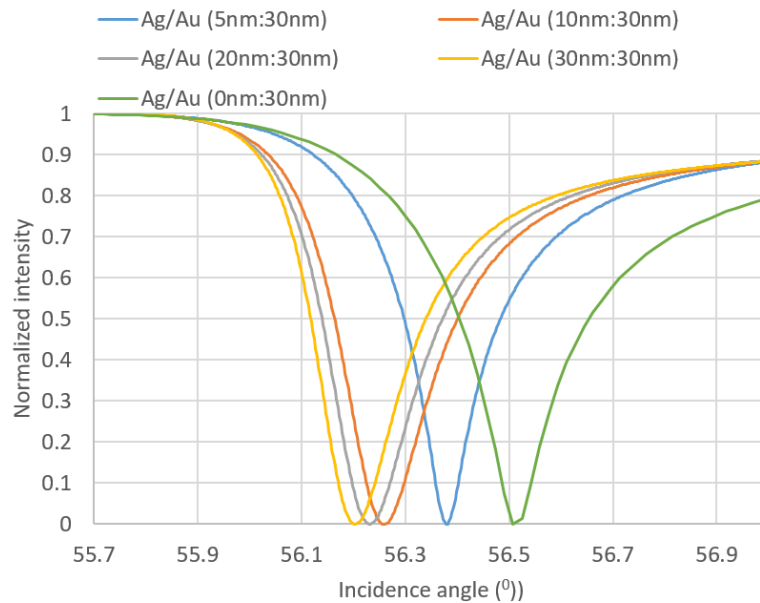


Figure 2.21 Modelling results of SPR curves for different thickness of silver when the gold thickness is kept constant.

Then, optimizing the bi-metallic sensor is not so direct since both overall metal thickness and thickness of each layer shall be jointly taken into account. Nevertheless, comparing the evolution of the FWHM value of the plasmonic responses for the cases reported in Figure 2.20 and 2.21 (Figure 2.22) shows that 1) thinner overall thickness (i.e. 35nm) gives the smallest FWHM values and 2) maximizing silver film thickness minimizes the FWHM values.

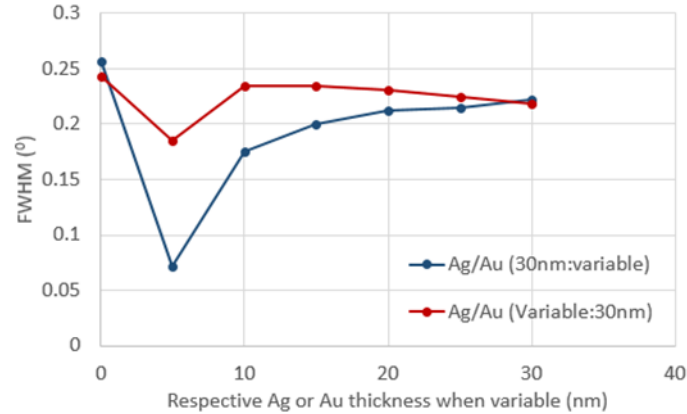


Figure 2.22 FWHM variation versus bi-metallic film composition: blue line: Ag thickness is 30 nm and gold thickness is variable, red line: Ag thickness is variable and gold thickness is 30 nm.

It appears that the combination Ag/Au (30nm:5nm) confers the best (lowest) FWHM value. We then calculate its sensitivity using the same calculation way than before, i.e. by modelling the sensor response to different solutions of ethylene glycol/water concentrations (Figure 2.23).

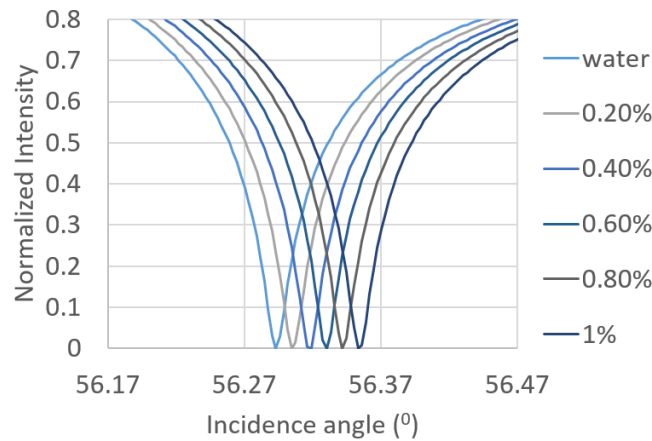


Figure 2.23 Calculated plasmonic responses of Ag/Au (30nm:5nm) bi-metallic sensor for different concentrations of ethylene glycol diluted in water.

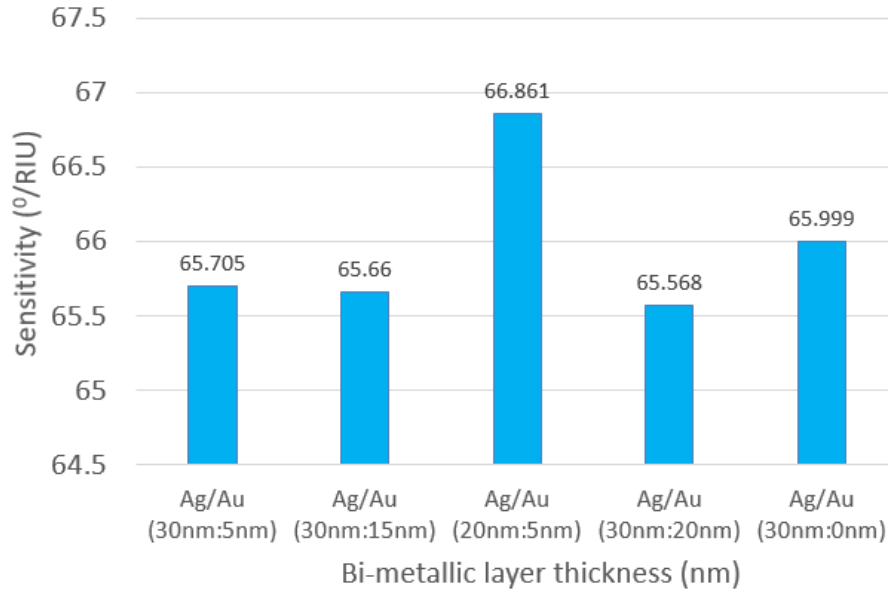


Figure 2.24 Sensitivity value for different bilayer sensor configurations.

Figure 2.24 shows the sensitivity of the sensor by using various metal thickness combinations. Ag/Au (20nm:5nm) gives a slightly higher value compared to other combinations but the difference is weak. Figure 2.25 shows the FOM value for both types of bi-metallic layer composition that are above mentioned, i.e. either keeping the gold or the silver layer of at constant value.

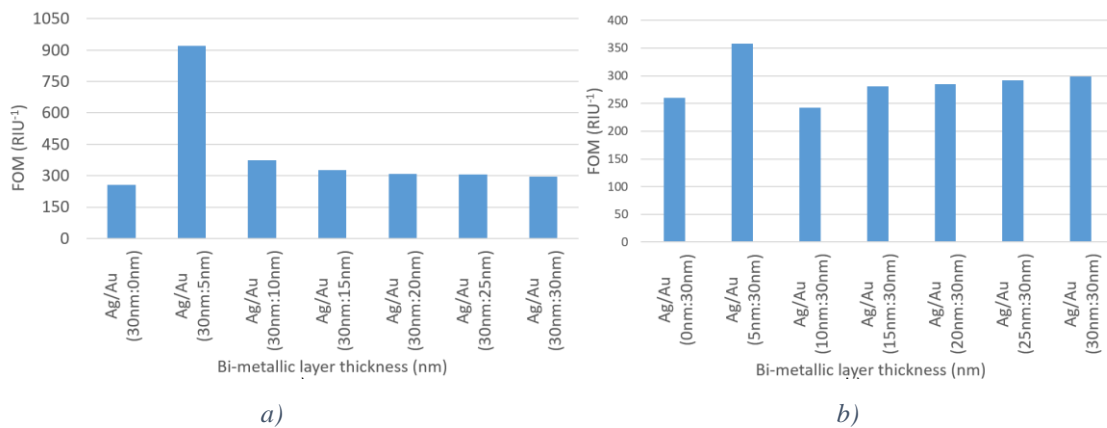


Figure 2.27 Calculated FOM for the bi-metallic plasmonic layer at 1550nm wavelength: a) thickness of silver is kept constant to 30nm and gold thickness is varied, b) reverse configuration.

As can be seen, only one case distinguishes, the Ag/Au (30nm:5nm) with a FOM value roughly 3 times higher than for other configurations.

### 2.3.7 Conclusion

In this chapter, I presented the results of the modelling tool that has been developed for the calculation of the plasmonic response of a sensor. The tool allows to model both investigated interrogation schemes, angular and spectral, in wavelength range from visible to near-IR.

At sensor level, it allows to determine what would the "best" layer thickness keeping in mind that performance parameters such as sensitivity, FWHM and FOM are somehow tricky to handle when the sensor is placed in its operational context, i.e. with surface functionalization and post-data treatment. Moreover, such as for bi-metallic sensor, some conclusions can be issued.

For the next experiments, and whatever the interrogation scheme is, we will use for the plasmonic film of the:

- mono-layer sensor: Au (35 nm)
- bi-layer sensor: Ag/Au (30nm:5nm)

A Ti (2nm) layer is always deposited as first layer as adhesion layer.

Concerning the experimental set-ups presented in next chapter, it allows to determine the injection parameters, i.e. mainly angle, of the input beam and so quickly reduces the setting time of the benches.

## Chapter 3: EXPERIMENTAL BENCHES

In this chapter, I present the two experimental benches that have been implemented and used in this work.

- an angular interrogation set-up working in the near-IR (1550 nm) band
- a spectral interrogation set-up working in the visible range (500 – 900 nm)

I also present the calibration process for both benches allowing to convert the raw data into calibrated data in Refractive Index Unit (RIU).



### 3.1 Angular interrogation scheme

#### 3.1.1 Set-up overview

An angular interrogation based SPR set up was already existing in the lab, it was developed during a previous INTERREG project and used in the PhD work of E. Wijaya [77]. Its schematic is given in Figure 3.1. Its implementation is shown in Figure 3.2. It is working in the near-infrared wavelength range and more precisely at 1550nm; this wavelength being intensively used in the fibre telecommunication domain, lot of stabilized sources exist. We use a semiconductor DFB source or a tuneable source with single mode fibre. The prism is a semi-cylindrical H-ZF1 material having a refractive index of 1.62 in this wavelength range; as seen in the modelling part (Chapter 2), this implies an incidence angle around  $60^\circ$ . A mirror was mounted on a micro rotating stage to finely control the angle of the input beam and finally a camera working in the near-infrared region was used to capture the reflected light exiting from the prism, also using a rotating mirror. The output image of the camera was treated using LabVIEW software to monitor the plasmon shift in real-time. Some data processing (filtering, averaging) as well as resonance shift calculation (intensity, centroid) are implemented in order obtaining the final sensorgrams. The SPR sensor is tightly pressed onto the prism using matching index liquid (Cargille Series A,  $n = 1.63$ ) [108].

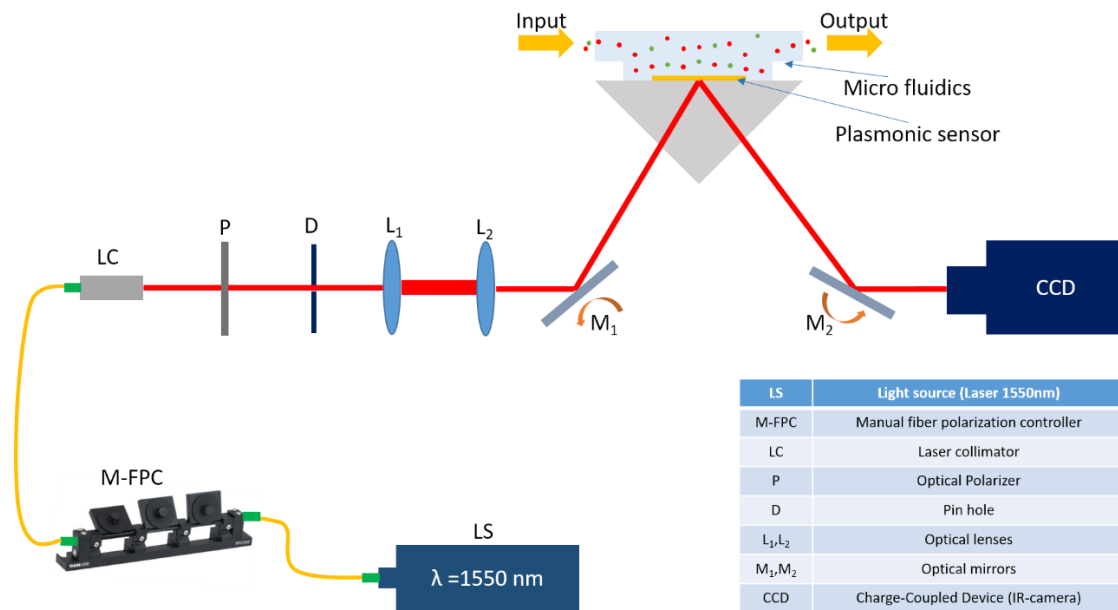


Figure 3.1 Schematics of the angular interrogation bench

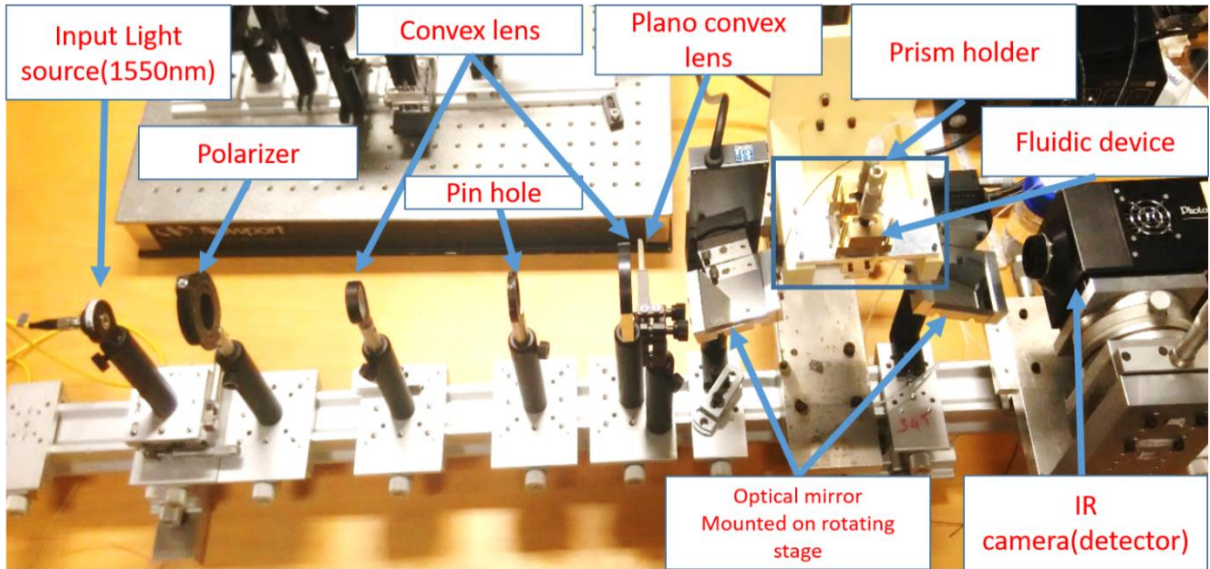


Figure 3.2 SPR bench using angular interrogation scheme.

Figure 3.3a shows the raw image captured by the IR camera (here using a device with fluidics injection on a 1.5 mm wide channel (see § 3.1.2). Figure 3.3b shows the corresponding plasmonic response after averaging, filtering and normalizing. At that time, the x-axis is only referring to a pixel position that is the raw data obtained from the IR camera. For bio-sensing applications, this x-axis labelling can remain in pixels, it would not affect the results. The conversion into angle position is only needed to feedback on modelling.

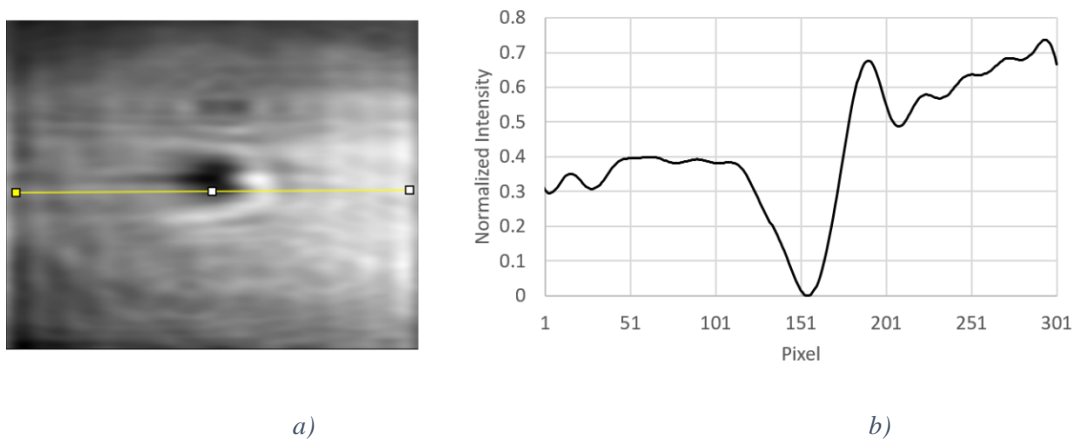
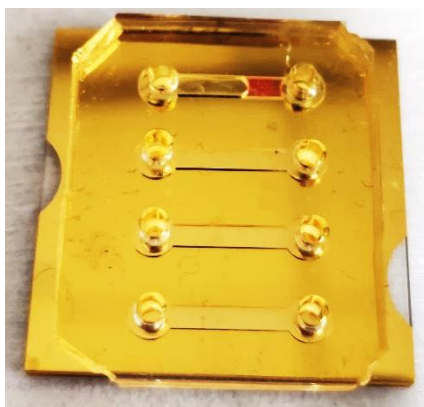


Figure 3.3 a) raw image of plasmonic response (water drop) as observed from IR camera, b) plasmonic response obtained after filtering, averaging and normalizing.

### 3.1.2 Set-up calibration

For calibration, we have used different concentrations of ethylene glycol solutions. The refractive index of solutions of ethylene glycol diluted in water is well known [109,110]. In order to ease fluidic measurements, PDMS microfluidic channels are integrated on the sensor (Figure 3.4) (See Appendix A for their fabrication details). A peristaltic pump is used launching the fluids into the channels. Such microfluidic channels have been used on the different sensors that have been tested on the different benches.



*Figure 3.4 Au plasmonic sensor with microfluidic PDMS channels.*

A centroid calculation is used to follow the shift of the plasmonic curve. Figure 3.5 shows the resulting sensorgram (sensor used has a 35 nm gold layer) when injecting various concentrations of ethylene glycol solutions (0.2% to 1% by weight in water, increment of 0.1%). A water cleaning/rinsing is made between the injections of the different solutions. This calibration gives the relationship between the position (pixel of camera) and the refractive index (Figure 3.6).

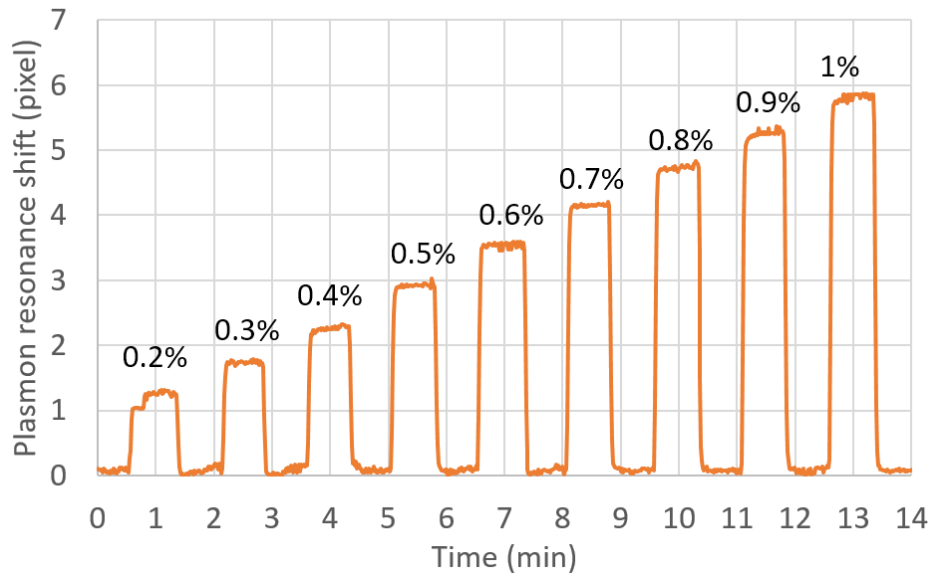


Figure 3.5 Sensorgram for various concentrations of ethylene glycol solutions. Resonance position (in pixel value) is given by a centroid calculation of the plasmonic responses.

The sensitivity that is so obtained is closed to 6362pixel/RIU (Figure 3.6).

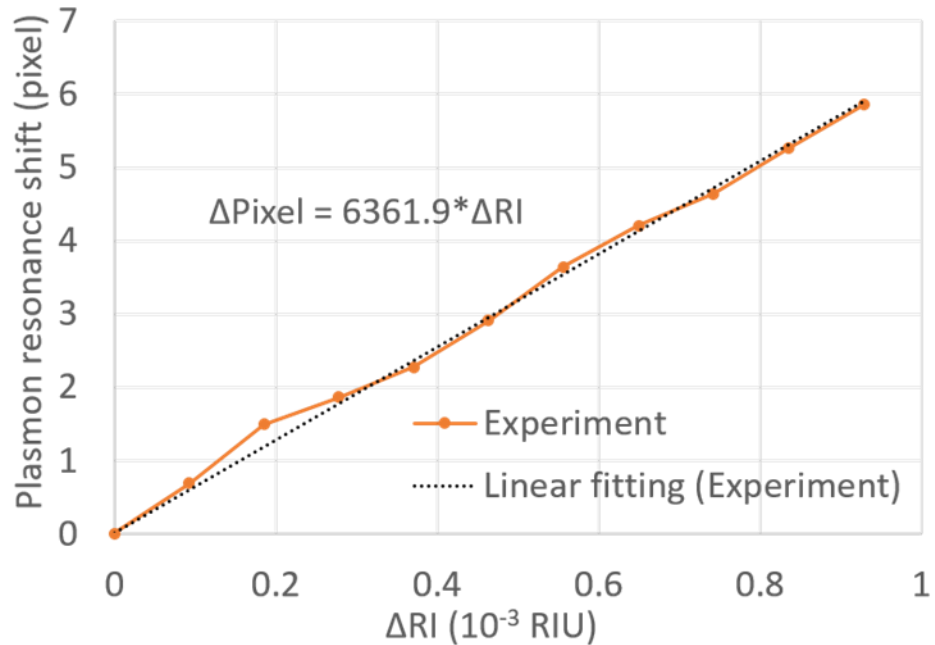


Figure 3.6 Relationship between changes in refractive index ( $\Delta RI$ ) vs change in the pixel position (movement of the plasmonic curve).

This sensitivity value (in pixels/RIU) cannot be used to compare with theoretical results. Indeed, it is a representation of the sensitivity of the system since the pixel position is an image of the angular position. To compare experimental and modelling results, we had to convert the change in pixel position to a change in the resonance angle. This was done using:

$$\Delta\theta = 2 \times \tan^{-1} \left( \frac{\Delta Pixel \times Pixel \text{ size}}{2 \times \text{distance from sensor to detector}} \right) \quad 3:1$$

where  $\Delta\theta$  is the change in resonance angle.

For our system, the relationship between angle and pixel position is  $\Delta\theta = 10.18 \times 10^{-3} \Delta Pixel$ . Using this relationship, the sensitivity can be converted into  $^{\circ}/RIU$  and the obtained value is close to  $65.05^{\circ}/RIU$  that is in the range of the theoretical calculated one (see Figure 2.8). Figure 3.7 is then the sensitivity of the system; it is the same curve than in Figure 3.6, pixel coordinate has only be changed in angle value.

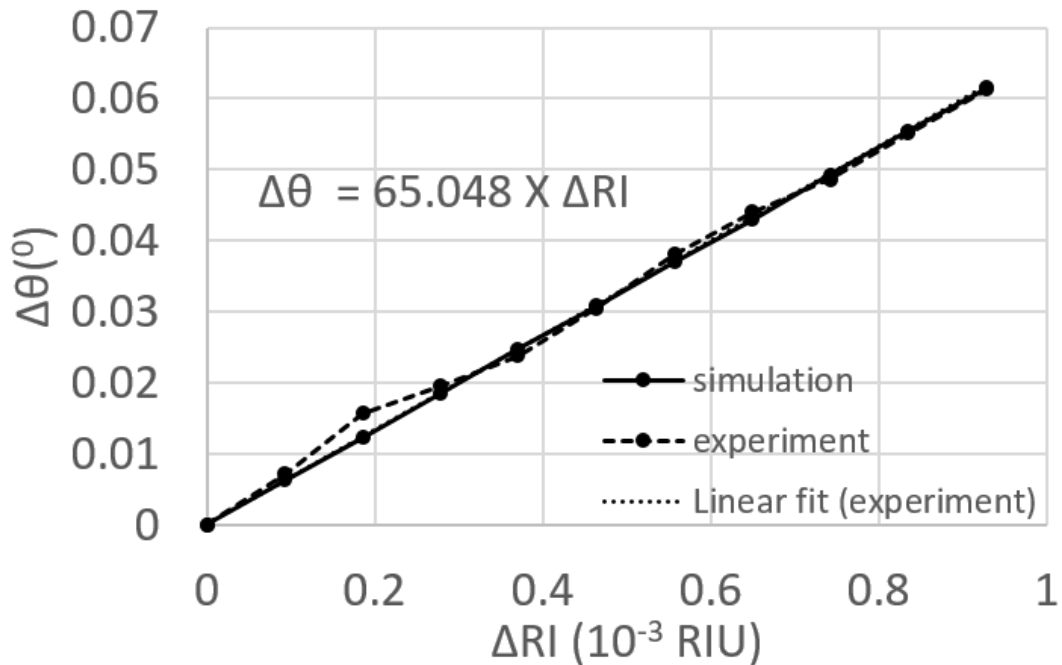


Figure 3.7 Comparison of the experimental and theoretical variation of the resonance angle with that of refractive index. Linear regression gives the sensitivity of the system.

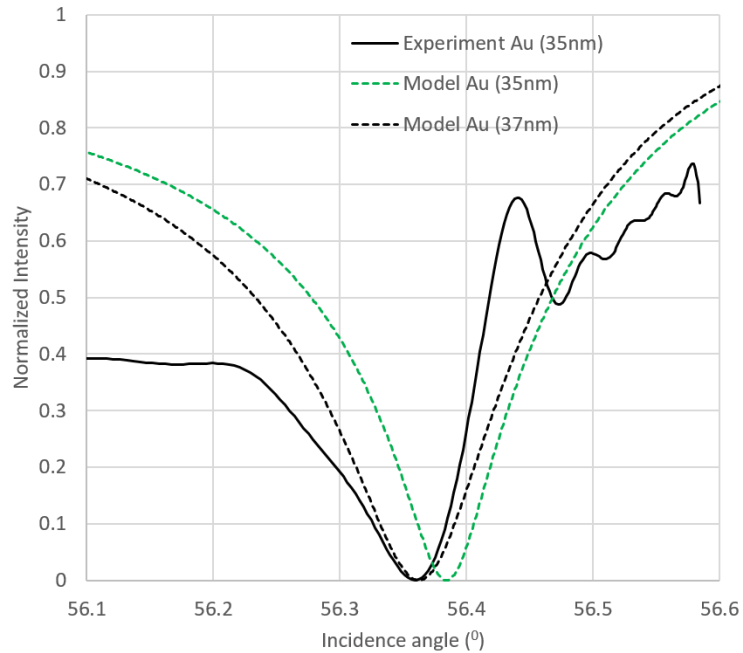


Figure 3.8 Comparison of experimental and theoretical plasmonic responses (note: modelling curve has been reversed in order to range the angle the same way that in experimental results).

Figure 3.8 represents the experimental and theoretical plasmonic responses. Targeted gold thickness was 35 nm. Using this value in the modelling gave a slightly different resonance angle. Simulated resonance angle fits for a gold thickness of 37nm. Nevertheless, this 2 nm difference is within the tolerance of the fabrication of the gold layer.

Likewise, we have also performed experiments to verify the reproducibility of the measurements. For this, we have repeated the same experiments with ethylene glycol solutions as used before and recorded the sensorgrams for all the experiments. For this experiment, as it has to be repeated several times, we have used only three concentrations of the ethylene glycol solutions.

Figure 3.9 shows the sensorgram of measured concentrations of ethylene glycol solutions for 4 different experiments.

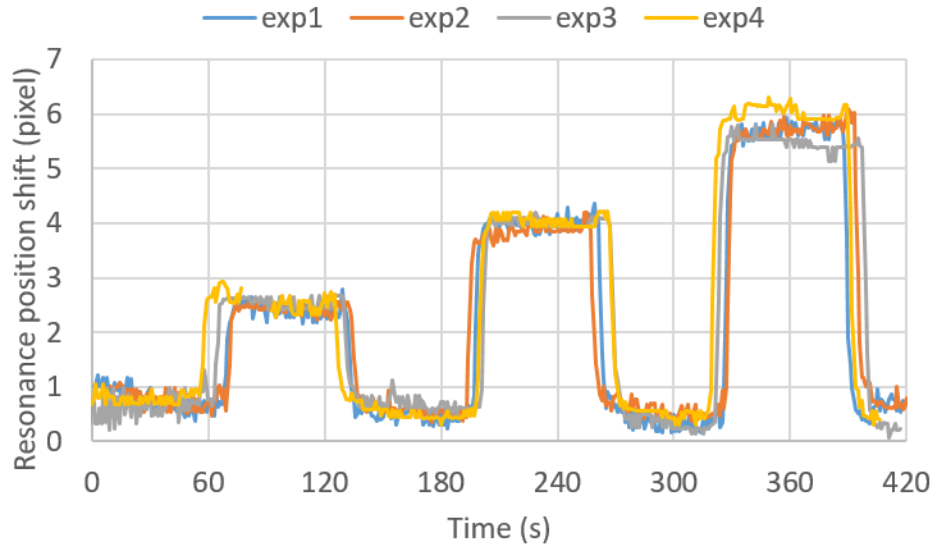


Figure 3.9 Reproducibility of the measurements: sensorgrams of four different experiments using ethylene glycol concentrations of 0.3%, 0.6%, and 0.9% in water.

These sensorgram data were post-treated and the relation between the refractive index and resonance angle was plotted (Figure 3.10). The results of the four experiments are coherent with the previous one (see Figure 3.7). The sensitivity value is then  $66.45 \pm 0.84$  °/RIU, that is a rather nice results since, even all care has been taken in carrying out the experiments, it is still fully manual operation.

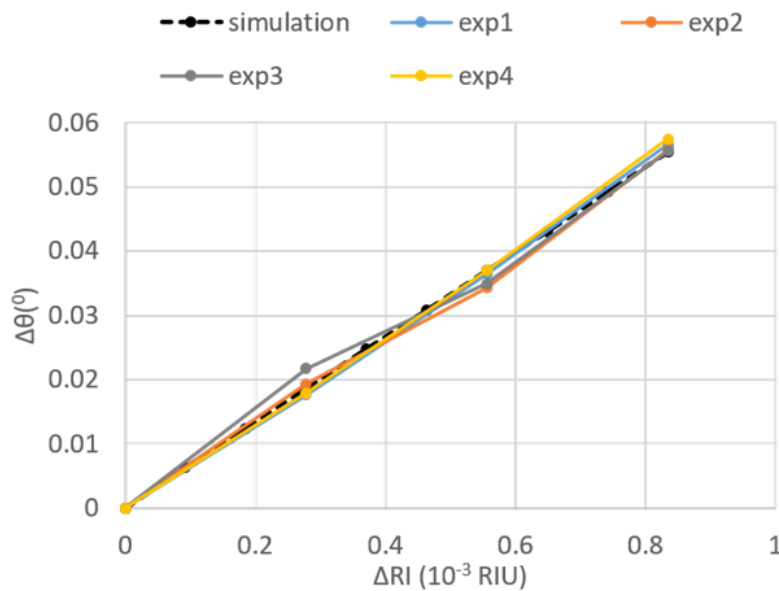


Figure 3.10 Reproducibility of the measurements: results of 4 different trials compared to theory (theoretical sensitivity is 66.4°/RIU and mean value of experimental one is 66.5°/RIU).

Finally, we have also evaluated the noise of the system. The experimental overall noise level can be due to several causes that are almost hard to distinguish: vibrations, optical noise, pixel noise, temperature, etc.

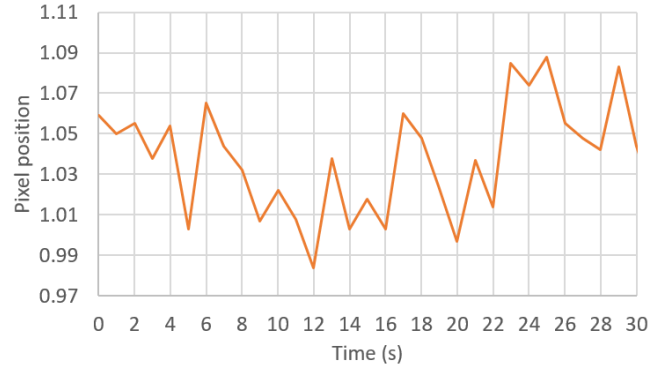


Figure 3.11 Fluctuation of system detection baseline.

The fluctuation of the baseline of a sensorgram (Figure 3.11) is evaluated at  $0.028 \text{ pixel}$  that corresponds to  $285 \times 10^{-6} \text{ }^\circ$ . If we consider that the minimum detectable signal is that providing a signal at least twice the amplitude of the noise level, the minimum detectable signal will be corresponding to  $0.056 \text{ pixel}$ . The limit of detection of our system should be there around  $8.60 \times 10^{-6} \text{ RIU}$ .

## 3.2 Spectral interrogation method

### 3.2.1 Set-up overview

The schematics of the spectral bench is shown in Figure 3.12. Compared to the angular interrogation setup, it was built more compact to develop the portable system. The input source is a fibered stabilized broadband (360 nm – 2600 nm) light source (Thorlabs SLS201) and the detector system is a compact spectrometer with a detection bandwidth of 500nm to 1000nm (Thorlabs CCS175). Ultimately, this spectrometer will be replaced by a proprietary spectrometer from the partner (Multitel) of BIOSENS project in charge of the fabrication of the whole portable system. Figure 3.13 shows the experimental implementation of the spectral interrogation optical setup.

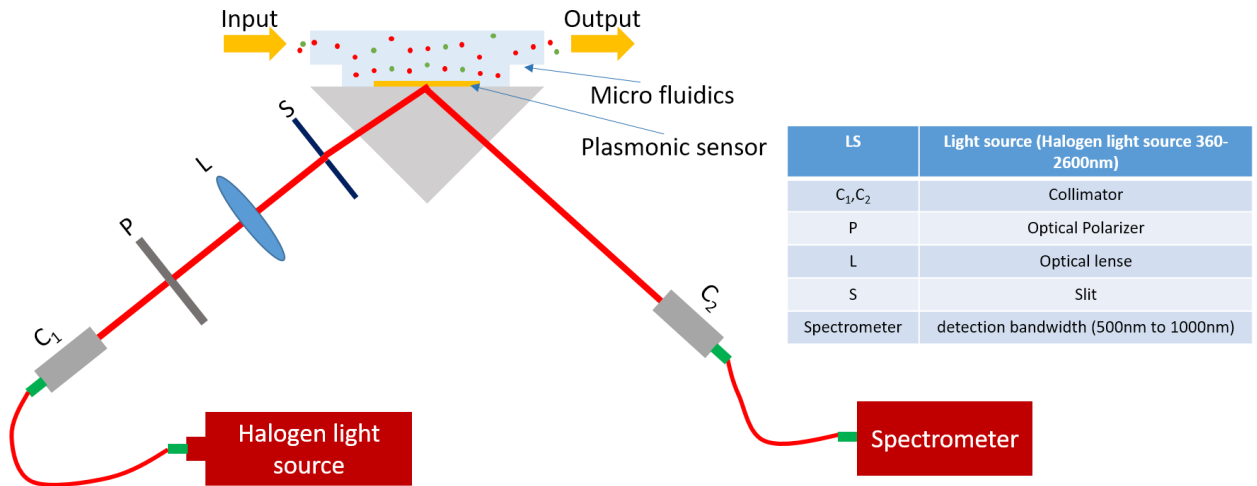


Figure 3.12 Schematics of spectral interrogation bench.

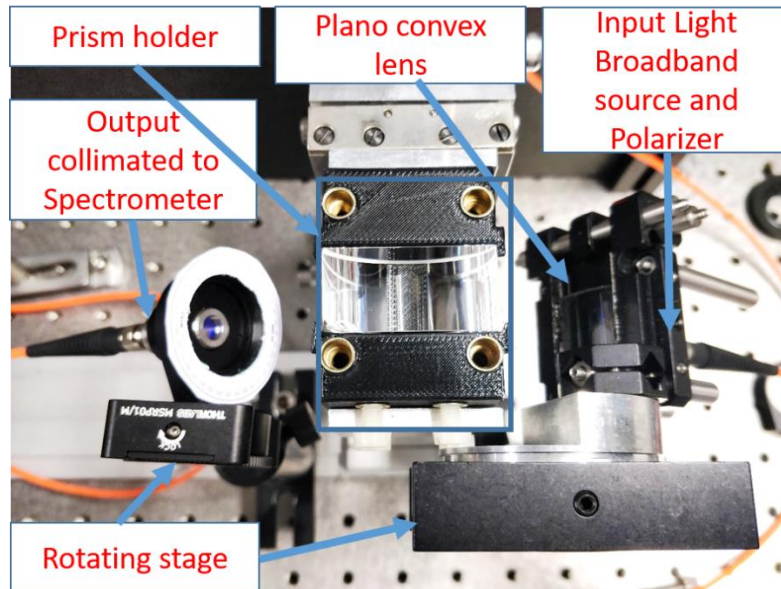


Figure 3.13 SPR bench using spectral interrogation scheme.

### 3.2.2 Set-up calibration

The input injection angle was determined from the simulation so that the plasmonic response can be observed in the wavelength range of the spectrometer. We chose it as  $60.71^\circ$  in order the response peak to be almost centred on the higher intensity levels of the full optical chain (source – SPR system – spectrometer). Although the data post-processing has the same goals (averaging, filtering, centroid calculation) than for the angular

interrogation scheme, it shall have been adapted to the output signal of the spectrometer (Figure 3.14). Injection of solutions is also made the same way than for the angular interrogation scheme, i.e. peristaltic pump and PDMS fluidics.

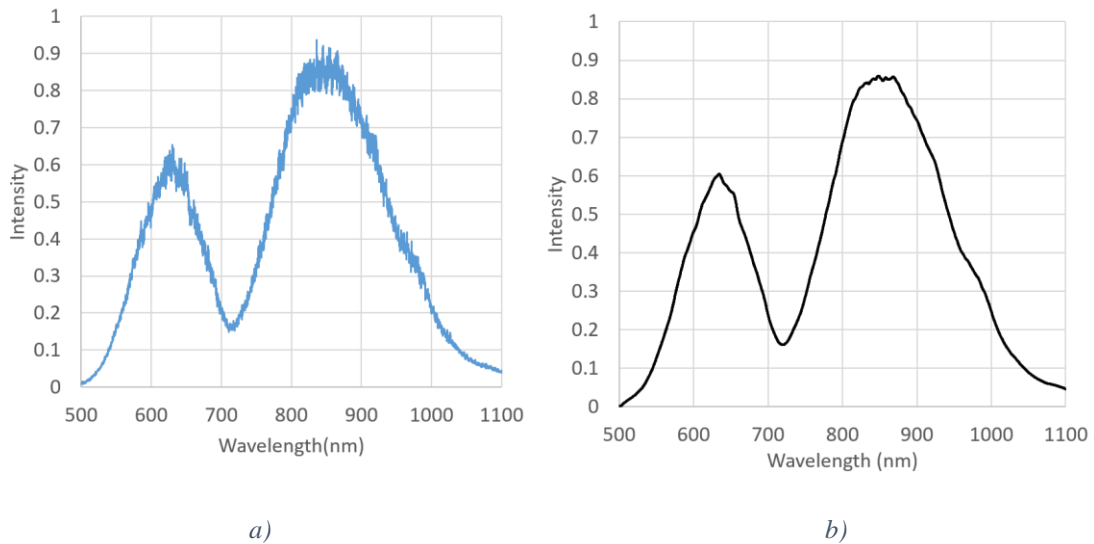


Figure 3.14 Plasmonic response a) raw data from spectrometer output, b) filtered spectrum.

Figure 3.15 represents the spectra for the different solutions of ethylene glycol.

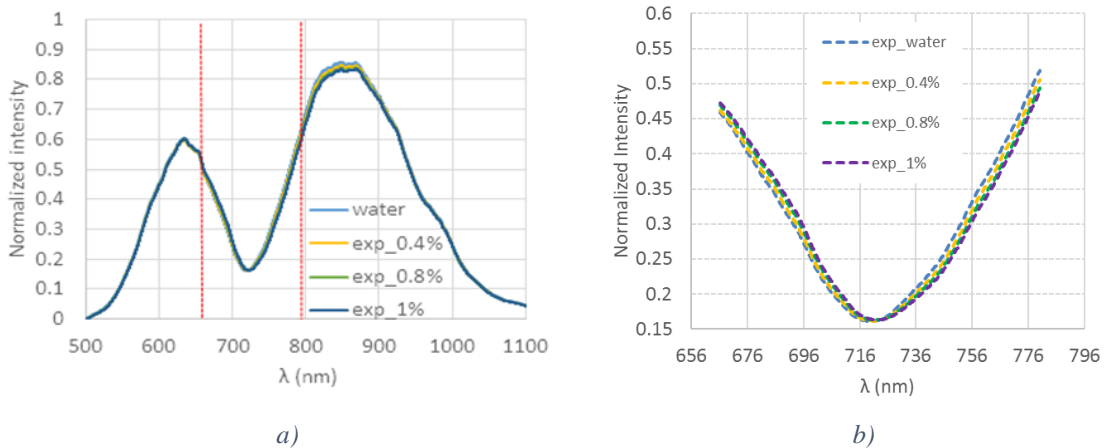


Figure 3.15 Plasmonic response versus different ethylene glycol solutions, a) full spectrum b) zoomed part (corresponding to the part between dashed lines on a)).

After post-processing, we compared the experimental and theoretical evolutions of the response curves. (Figure 3.16). Experimental curves are slightly broader than theoretical ones but minimum position is located as the same position.

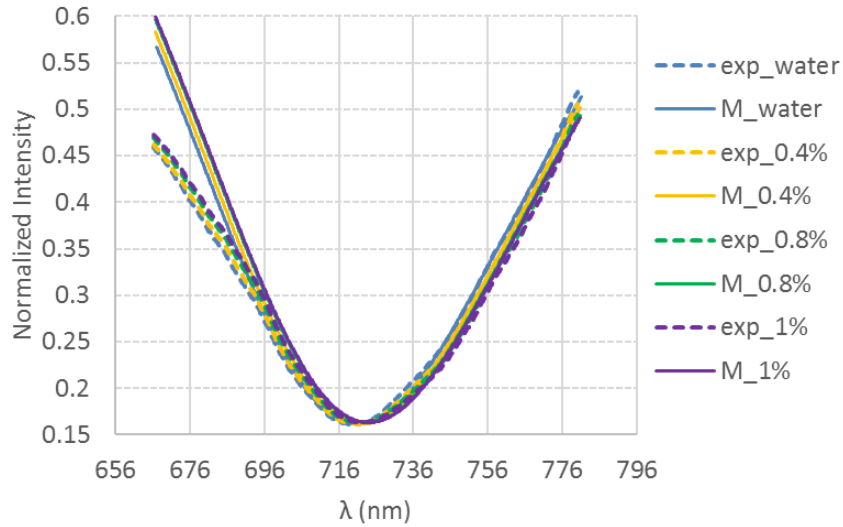


Figure 3.16 Experimental (exp\_, dashed lines) and theoretical (M\_, solid lines) plasmonic responses for different concentrations of ethylene glycol solutions (\_XX% in weight)

We first calculate the sensitivity with a centroid calculation using wavelength boundaries (Figure 3.17).

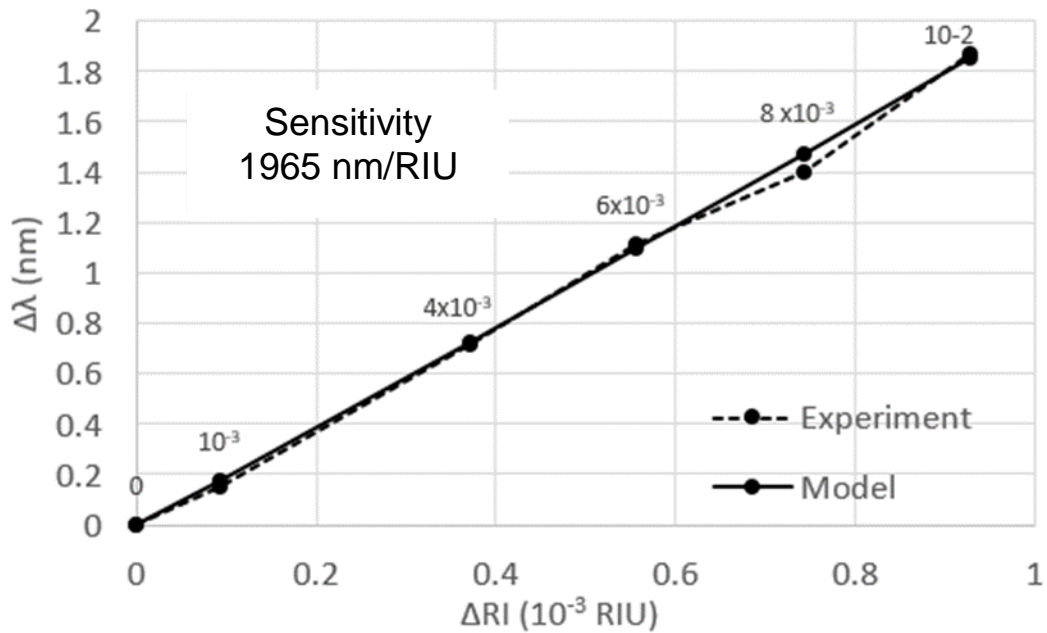


Figure 3.17 Calibration of the spectral interrogation scheme set-up using reference solutions made of different concentrations of ethylene glycol solutions (% EG by weight in water indicated above each data point).  $\Delta RI$  is the refractive index difference of the solutions to pure deionized water (0%) and  $\Delta \lambda$  is the shift of plasmonic response obtained by centroid calculation using spectral boundaries.

The obtained value was 1965 nm/RIU that fits pretty well with the calculated value using same centroid calculation on theoretical curves. In order to show that this sensitivity value

can be very sensitive to the data processing and so the values that can be encountered here and there, we applied another centroid calculation algorithm to both theoretical and experimental response curves. This second algorithm is based on calculation boundaries fixed by an adaptive level governed by the minimum of spectra. The result is presented in Figure 3.18. The sensitivity value is now of  $38 \times 10^2$  nm/RIU.

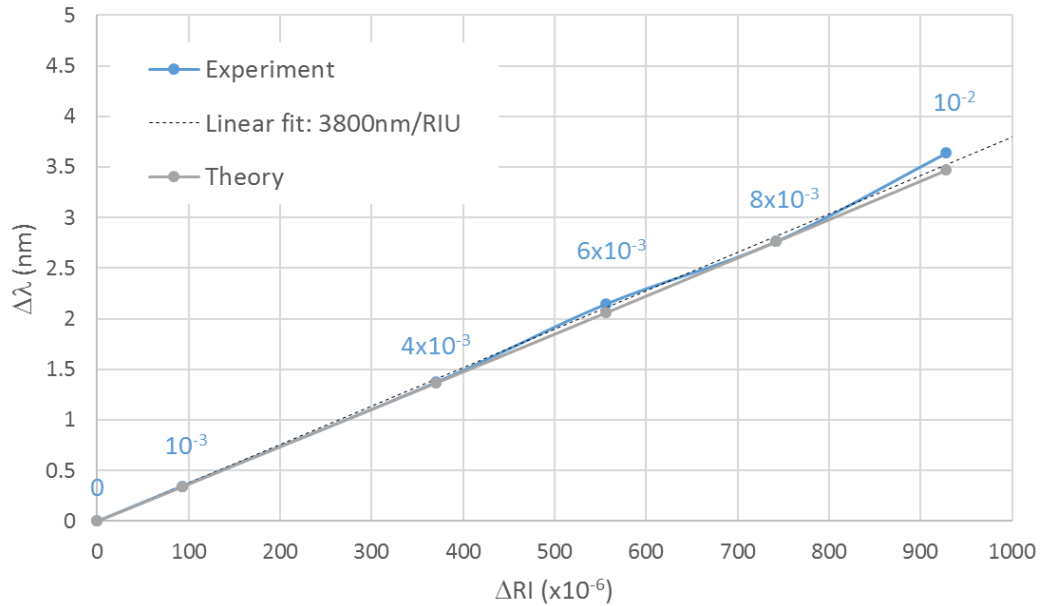


Figure 3.18: Calibration of the spectral interrogation scheme set-up using reference solutions made of different concentrations of ethylene glycol solutions (% EG by weight in water indicated above each data point).  $\Delta RI$  is the refractive index difference of the solutions to pure deionized water (0%) and  $\Delta \lambda$  is the shift of plasmonic response obtained by centroid calculation.

### 3.3 Conclusion:

In this chapter, we presented the two benches I worked on. Experimentations were firstly conducted on the angular bench and, as going along with its implementation, they were conducted on the spectral bench whose principle has been used in the portable equipment developed in the BIOSENS project. Owing to its higher potential compactness and the ability of the MULTITEL partner of the BIOSENS project to fabricate multi-channel spectrometers, the spectral interrogation scheme has been kept to be integrated within the portable equipment that has been developed by this partner.

We also presented the calibration of those benches using different concentrations of mix water/ethylene glycol solutions. As far as same data treatment is used calculating the sensitivity of the full detection system, good agreements are obtained between theoretical and experimental results. We also noticed that sensitivity values are mainly governed by the post-data treatment than by that of the sensor alone.



## Chapter 4: SPR SENSOR WITH INTEGRATED TEMPERATURE CONTROL

In this chapter, we will present the innovative way that has been studied in order avoiding the use of a bulky temperature system control for implementing the SPR set-up in a compact environment.

The way that is proposed allows not only the temperature control of the sensed medium but also permits to control independently the temperature of several channels. This temperature control can be used two ways:

- to control and so maintain a constant temperature during experiments, this is the usual way temperature control is used in SPR system
- to tune finely the temperature during a SPR measurement. This is a totally innovative use that allows to observe the behaviour of molecular interactions versus temperature.

For the purpose of demonstration and following a global discussion within the BIOSENS project, mainly with the biologist partners, a number of 4 channels has been chosen. All demonstrations have been so made using such a sensor that is made on 2.5 cm x 2.5 cm glass substrate.



## 4.1 Basic idea that governs the implementation of the integrated temperature control

In the basics of surface plasmon resonance phenomenon (see Chapter 2), we saw that plasmonic wave senses the medium in the so-called penetration depth. The value of this characteristics either for the angular interrogation system we used in the near – IR band or the spectral interrogation system in the visible range, is very small, between 200nm in the visible range up to 1 $\mu$ m in the near-IR (Figure 4.1). Then, the plasmonic response only reflects the temperature effect occurring within this penetration depth, all other temperature effects (i.e. bulk of the sensed medium) is not taken into account.

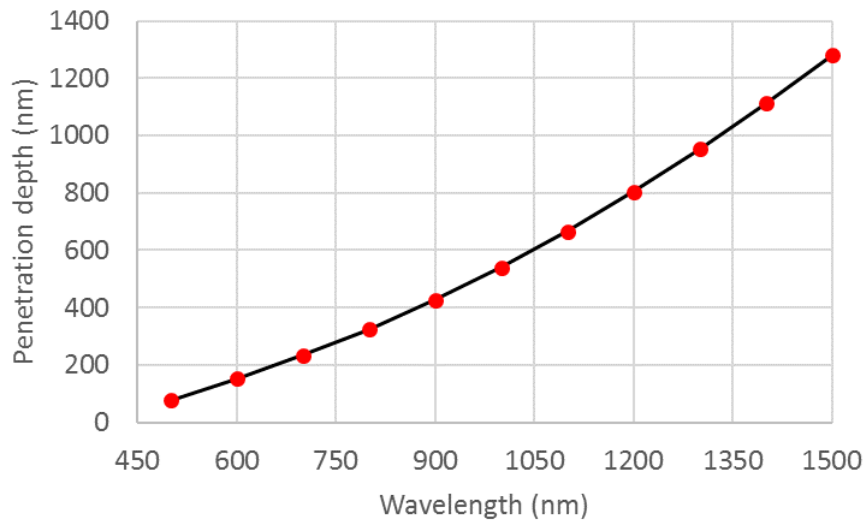


*Figure 4.1 Penetration depth of the plasmonic wave into water (35nm gold sensor)*

The idea is then to control the temperature in this very close vicinity of the sensor surface, where the measure takes place. We chose to investigate the use of the Joule effect using directly the plasmonic layer metal as heater.

In order to get 4 channels (but this is even valid for 1 channel or even more channels), we cannot any more have a full surface coverage of the plasmonic layer and only delimitating the different channels by the PDMS microfluidics. The plasmonic layer shall be then patterned in order to control the path of current and so the heat behaviour. It would also allow separate electrical feeding of the channels.

## 4.2 Design and fabrication of multichannel SPR sensor

The SPR sensor is always fabricated on a glass slide (H-ZF1 in our case) that is compatible with the SPR test set-ups that are employed (see Chapter 3) which uses such a glass type coupling prism. Obviously, the use of any other glass substrate is possible; it does not affect the principle that is hereby presented. As above mentioned, the plasmonic layer has to be patterned to afford the possibility of different heating on each channel. So, each sensing channel is materialized by a separate plasmonic layer.

The glass substrate is first cleaned into a piranha solution ( $\text{H}_2\text{SO}_4:\text{H}_2\text{O}_2$ ) and placed onto a hot plate at  $90^\circ\text{C}$  for dehydration. AZ1512 photoresist is then spin coated to obtain a  $1.5\mu\text{m}$ -thick layer (10s at a rotation speed of 2600rpm with acceleration of 4000rpm/s and in a closed environment. Photoresist post-bake is made on a hot plate at  $110^\circ\text{C}$  in order evacuating solvent. In order to get an easy versatility in the design, laser lithography was used. We use a DILASE 650 equipment from KLOÉ [111] (Figure 4.2a). The laser writing parameters i.e. writing speed, laser power, spot size, spot focus etc... were adjusted to obtain the patterns with good aspect ratio. After different dose tests, optimized parameters were defined as 25% power ratio, 50mm/s writing speed and  $10\mu\text{m}$  spot size. After insulation, resist is developed using a AZ400K solution (AZ400K/water, 1:3) by dipping the insulated substrate during 25s. During development of the pattern, exposed area of the resin was removed by the developer and non-exposed areas were hardened. This makes the photo-resin to stop reacting with the photons anymore. To verify that the area of interest was removed by the developer, the sample was viewed under optical microscopy. From this observation it can be verified that patterns have the right dimensions and are fully developed, i.e. that no resist is still present at bottom. The thickness of the photoresist was verified using a contact profilometer [112] (BRUKER DEKTAK XT-A) in order insure a correct ratio between photo resist thickness and metal thickness that will be deposited. This ratio is commonly taken as 5 in order no problems occur during the lift off process. The measured thickness of photoresist is  $1.5\mu\text{m}$  (Figure 4.2b). This thickness is much more the minimum one that should be required for metallization of the plasmonic layer, since roughly 200 nm would have been sufficient, but it will necessary for further processes (see

§ 4.7.2.2). Doing so, optimization of one process is enough for all the metallization steps I will have to use during this work.

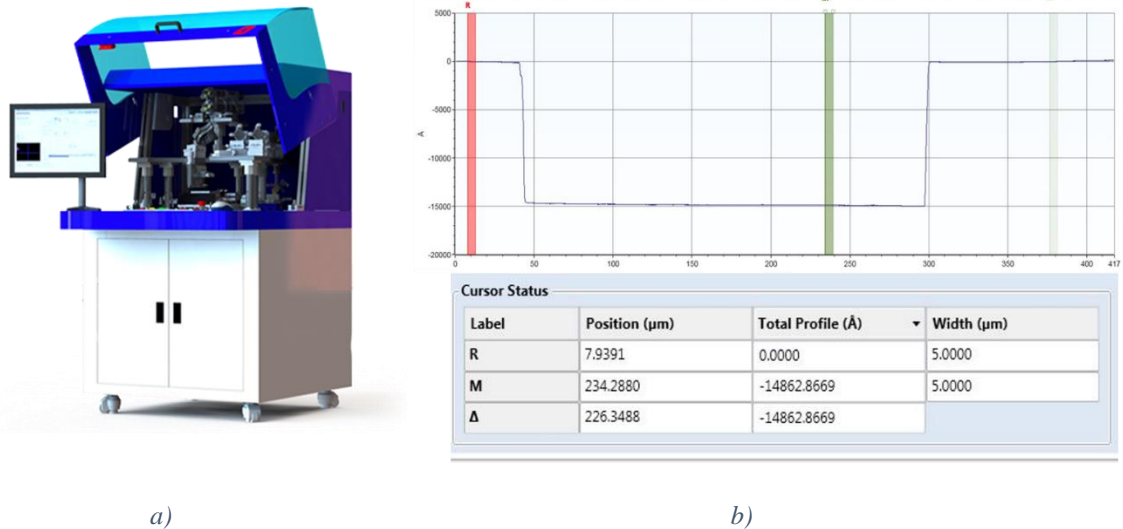


Figure 4.2 a) DILASE 650 laser writing system b) AZI1512 photoresist profile after development.

Subsequently, the developed sample was classically metallized with very thin layer of 2nm of titanium (Ti) and followed by gold (Au) of 35nm thick using e-beam evaporation in a high vacuum system (base vacuum level of  $10^{-8}$  mbar). The thin layer of Ti (2nm) was deposited to make the strong bonding between the gold and the glass substrate. During the vapor deposition method the metal was deposited on all over the surface of the sample. To remove the metal from all over except in the region of interest, we have carried out a lift-off process. Using a photoresist stripper, the resist and the metal deposited above are removed from the substrate leaving only the metal that was deposited directly on glass (exposed areas during insulation step). This process was carried out at 70°C with the sample immersed inside a resin stripper solution (AR 300-76) for an hour.

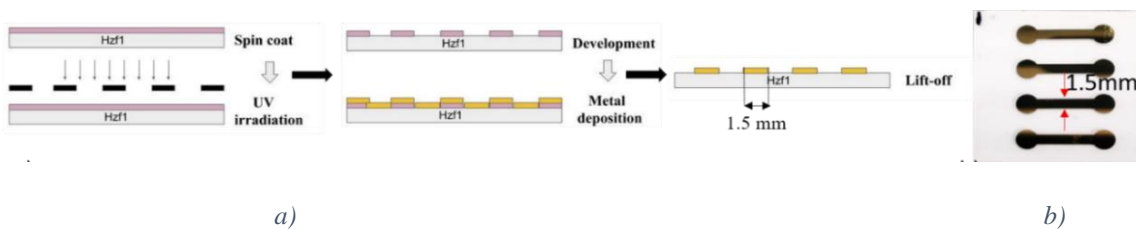


Fig 4.3 a) main steps of fabrication process b) view of a 4-channel sensor.

An overview of the main fabrication steps is shown in Figure 4.3a and an optical microscope view of a 4-channel sensor in Figure 4.3b. Channel width is 1.5mm, channel length is 1cm and channel spacing is 4mm edge to edge.

#### 4.3 Plasmonic channel as a Joule's effect heater.

Since the conductivity of the plasmonic layer will directly affect the resistance of the channel, it shall be measured, moreover versus the temperature. The sensor has been placed on the hotplate of the thermal measurement system (see § 4.5.1) and the resistance of a channel has been measured in a classical four probe scheme. Taking into account the dimensions of this channel (see § 4.2 above), the conductivity and resistivity of the plasmonic layer has been calculated. The result is shown in Figure 4.4. In the 20°C - 100°C, resistivity value is between 41 and 46 nΩ.m which is in very good agreement with values reported for such thin films [113, 114]. The value of the Temperature Coefficient of Resistivity (TCR) has been determined as  $1.65 \times 10^{-3}/^{\circ}$  that is in good agreement with reported values for evaporated thin films of gold on glass [115]. This value of TCR is used to extrapolate the resistivity value to higher temperatures.

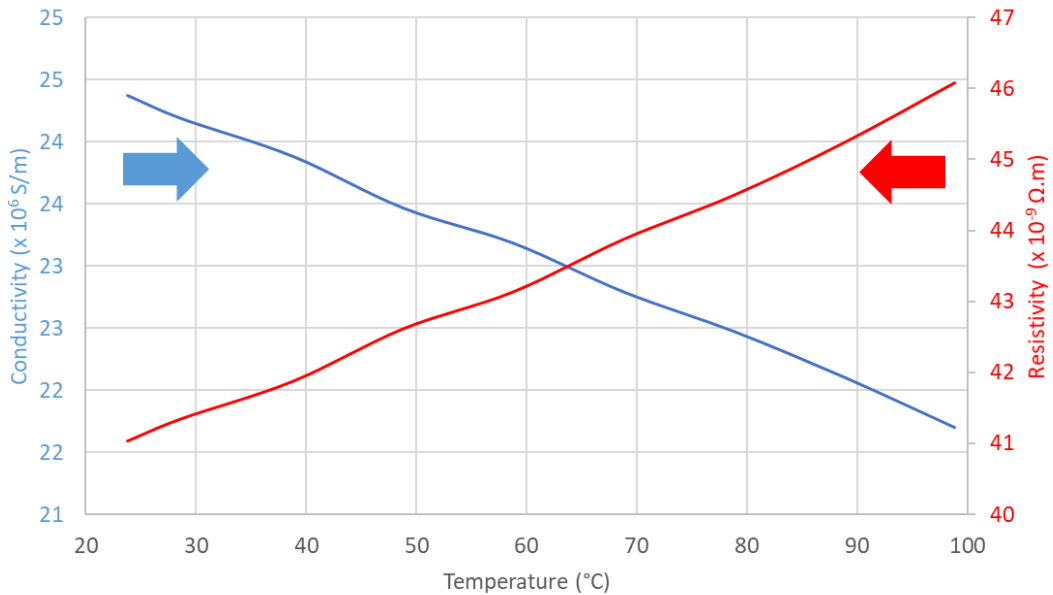


Figure 4.4 Electrical properties of the plasmonic layer versus temperature.

## 4.4 Modelling the thermal behaviour of the plasmonic metal layer

### 4.4.1 Modelling of Joule's effect

COMSOL has been used to simulate the thermal behaviour of a channel under current injection. The simulated structure is presented in Figure 4.5. In a first attempt, the full sensor has been simulated. The glass substrate is 2.5 cm x 2.5 cm and 1mm thick and the four channels have been implemented. The simulation parameters for both the glass substrate and gold are shown in Table 4.1. The first three parameters are used for simulating the thermal behavior and the last one for the electrical one. The above atmosphere has been set to air and ambient temperature to 20°C. A heat transfer coefficient value of 50 W/m<sup>2</sup>K has been taken, which is commonly assumed for laboratory conditions [116].

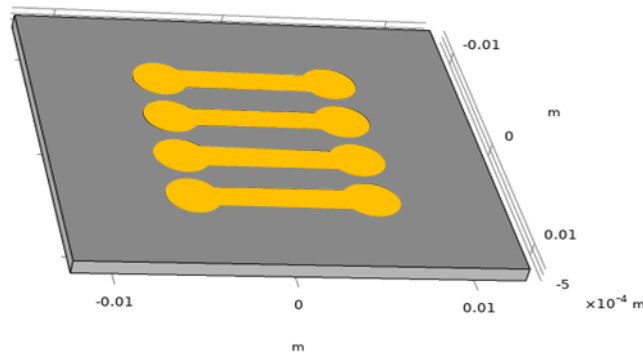


Figure 4.5 COMSOL simulated structure (metallic SPR surfaces are symbolized by yellow color)

	Glass	Gold	Unit
<b>Density (<math>\rho</math>)</b>	2730	17000	kg/m <sup>3</sup>
<b>Thermal conductivity (K)</b>	0.85	300	W/(m.K)
<b>Heat capacity (Cp)</b>	730	128.8	J/(Kg.K)
<b>Electrical conductivity (<math>\sigma</math>)</b>		From measurement (see §4.3)	S/m

Table 4.1: Material parameters used in the COMSOL simulation

The current has been injected into one channel. A typical graphical output is shown in Figure 4.6. As it will be detailed afterward (see Figure 4.7), lateral thermal expansion is limited to the close vicinity of the channel. This has particularly two main repercussions:

- it consolidates our original goal having independent control of each channel,
- it allows us to narrow the modelling window (white delimitation in Figure 4.6) and so to considerably decrease the calculation time.

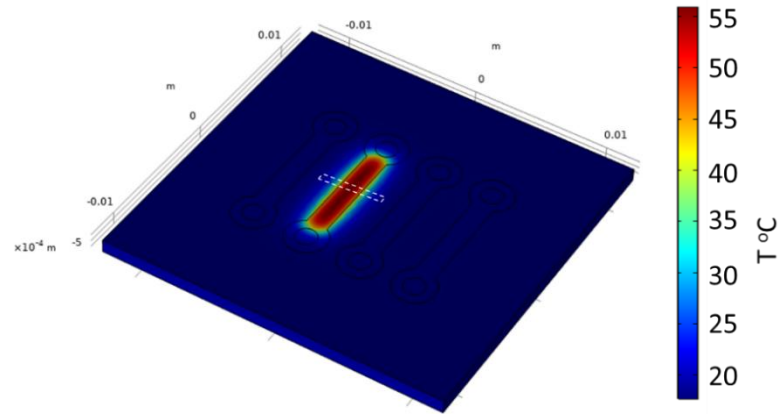


Figure 4.6 Typical graphical representation of sensor surface temperature under current injection (here 300 mA). The white delimitation refers to the narrowed surface area that will be used in further modeling.

So, the modelling was replicated on a smaller window (Figure 4.7). Extension from channel edge is 2.25mm each side of the channel width and channel length is 1.5 mm (full window is so 6 mm wide and 1.5mm long). The current injection is made on the full width of the channel (1.5 mm). The temperature that is obtained in such a narrowed modelling window is the same as obtained on the full sensor and validates so the use of this narrow window for further modelling.

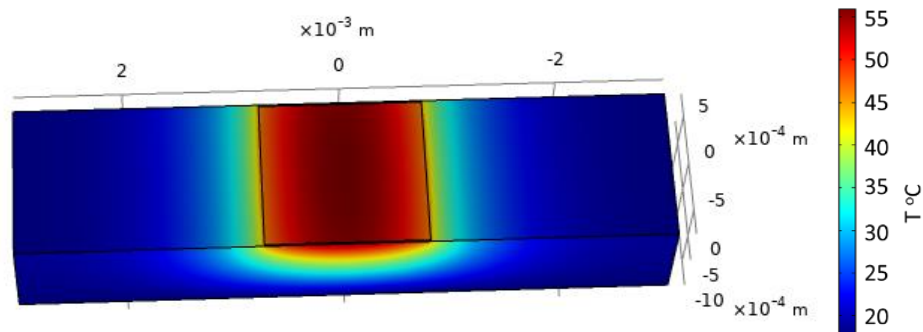


Figure 4.7 Narrowed surface area modelling window, under same current injection conditions than full sensor (see Figure 4.5)

The temperature profile across the modelled section is reported in Figure 4.8. High-temperature rises can be obtained but practical cases, for biological interactions, for instance, will mainly concern temperature rises in the order of some tens of degrees.

It can be observed a temperature gradient along the channel width, the higher temperature at the channel centre than on channel edges. Outside the channel, the temperature is quickly decreasing. The residual temperature outside the channel is even higher as the temperature is increased in the channel. Such a temperature gradient is quite classical for flat wires and has already been described for PCB lines [117] or integrated circuit interconnects [118]. However, this modelling reflects the case of this particular plasmonic layer that is very thin and deposited on glass.

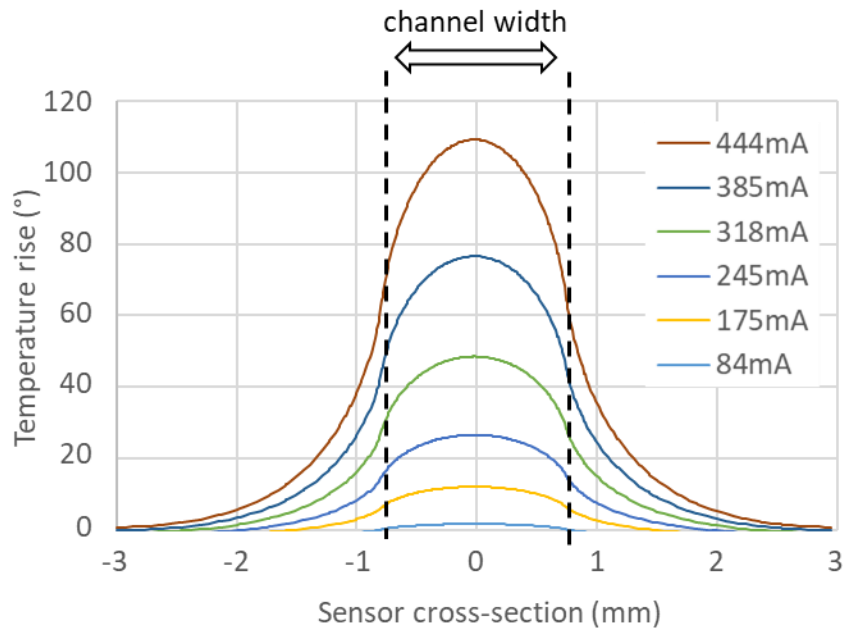


Figure 4.8 Cross-sectional temperature rise distribution versus injected current.

The maximum temperature rise (value at the channel centre) versus the injected current is reported in Figure 4.9 (w/oKPT curve).

#### 4.4.2 Matching the modelling with the experiments

As will be discussed in the experimental section dedicated to thermal measurements (see § 4.5.1), a 50 $\mu\text{m}$ -thick polyimide film (Kapton) has to be inserted for temperature measurements by infrared flux detection. To check the impact of such a film on the temperature that is measured, it has been inserted in the modelling. A block representing this film is stacked over the full surface area. Its parameters are:  $\rho = 1300 \text{ kg/m}^3$ ,  $K = 0.25 \text{ W/(m.K)}$  and  $C_p = 1000 \text{ J/(Kg.K)}$  [119]. The modelling has then been conducted the same way than previously. Figure 4.9 shows the results for both uncovered (w/oKPT) and covered (wKPT) channels with Kapton. For the polyimide film covered case (wKPT), the temperature at its surface is slightly lower than for the uncovered case. A mean value of 1.8% variation is obtained over the full temperature range. This modelling shows that the polyimide film slightly affects the experimental measurement and that its effect is computable anyhow.

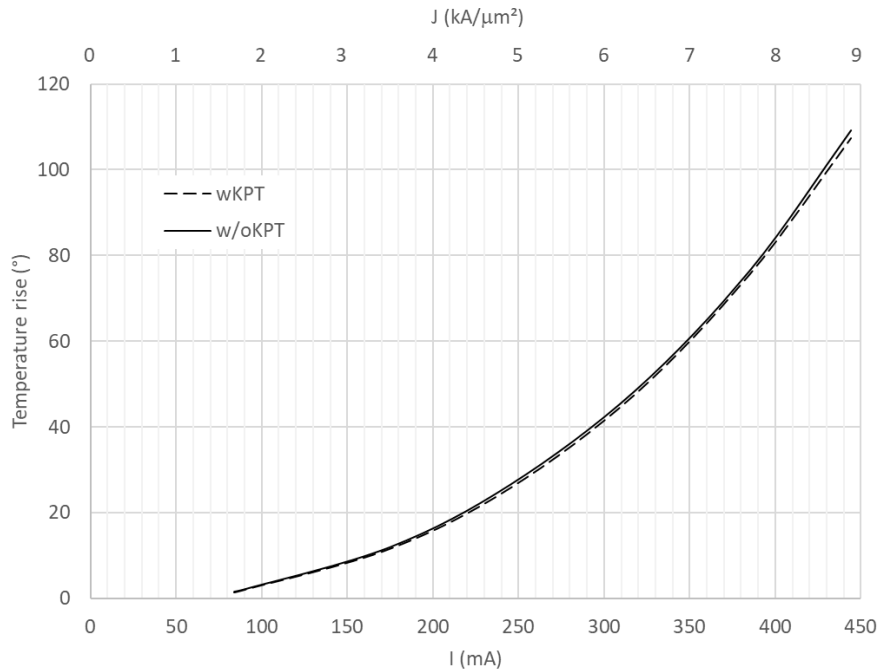


Figure 4.9 Temperature rise at channel centre versus injected current and current density.

### 4.4.3 Time dependence

For both cases (wKPT and w/oKPT), the time evolution has been modelled for different injected currents. The 10%-90% rise time is reported in Figure 4.10. The overall behaviour exhibits a slight decrease in rising time when the value of injected current increases. Comparing both cases, wKPT and w/oKPT, shows that:

- the slope is almost the same for both cases,
- the mean value of rising time is lower for the w/oKPT case, reflecting the slight heat capacitance behaviour of the polyimide film.

The rise time is then around  $1.6 \text{ s} \pm 10\%$  and  $1.75 \text{ s} \pm 10\%$  for the w/oKPT and wKPT cases, respectively, for the whole range of investigated currents.

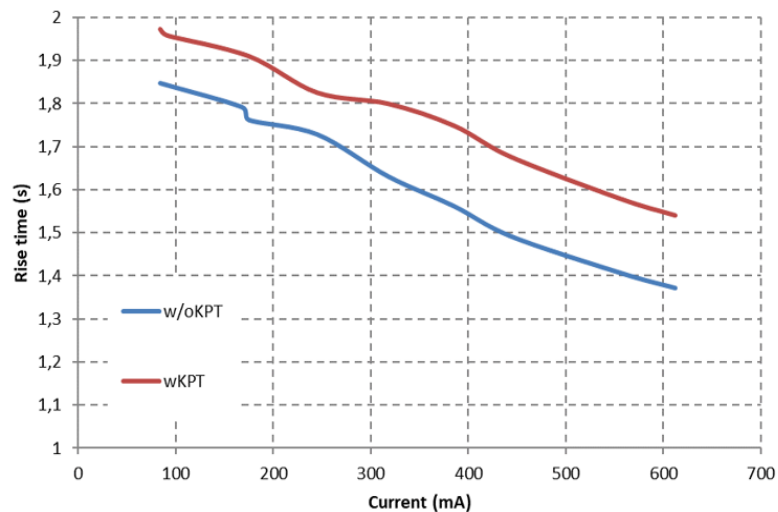


Figure 4.10 Rise time of the heating process.

## 4.5 Characterization of the thermal behaviour of the plasmonic layer

### 4.5.1 Measurement set-up

An InfraScope™ MWIR Temperature Mapping Microscope (Quantum Focus Instruments Corporation) was used for measuring the temperature of the channel under current

injection. The sensor is placed onto the sample holder of the equipment (Figure 4.11). To improve the sensitivity of the measurement:

- this holder is maintained at 60°C. The number of emitted photons for 1° temperature rise is then higher at a base temperature of 60°C than at 20°C since it increases as a cubic function with absolute temperature [120].

- a 50µm-thick adhesive polyimide film (Kapton) is placed onto the sensor to enhance emissivity. The evaporated gold thin films, that can be considered as polished gold, have low emissivity coefficient value, a commonly agreed value is between 0.01 and 0.02, the one of Kapton is between 0.75 and 0.85 [121]. The difference can be clearly observed on Figure 4.12 where the left part of the channel has been covered by a Kapton film and the right part is a nude gold surface: weak signal is emitted from the uncoated part of the channel.

1x magnification lens was used to focus on the sensor channel. The current was injected in the channel using electrical probes placed on both ends (circular patterns on Figure 4.13). QFI temperature mapping software was used to perform emissivity correction and to generate the true temperature map. Without injecting current, the so captured image is stored as the reference level. A follow-up of the experiment is made in movie mode to follow the real-time temperature variation.

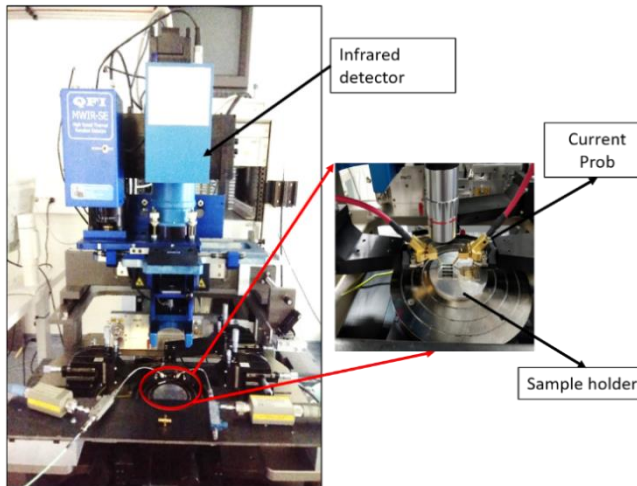


Figure 4.11 MWIR temperature microscope and measurement set-up

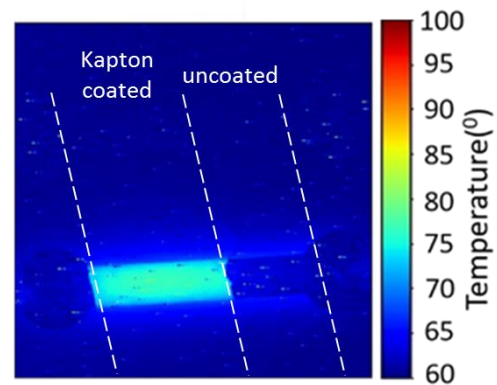


Figure 4.12 Effect of Kapton coating on thermal imaging.

#### 4.5.2 Thermal measurements

In order to determine experimentally the influence of Kapton on the IR imaging thermal measurement, two experiments were carried out:

- 1) the plasmonic channel was fully covered with kapton tape (Figure 4.14 left) (corresponding to the wKPT case of theoretical study),
- 2) the plasmonic channel was partially covered with kapton tape (Figure 4.14 right) (corresponds to the w/oKPT case of theoretical study)

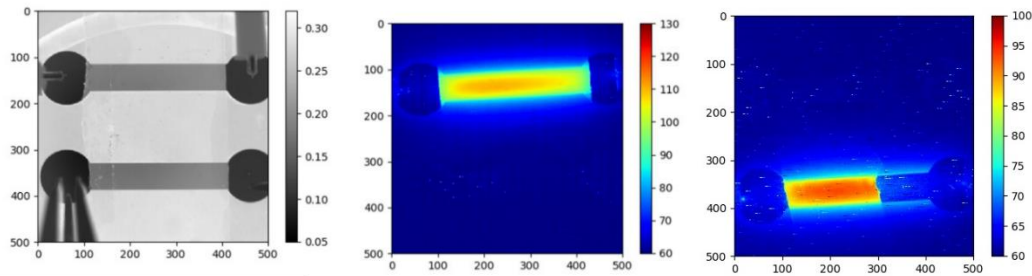


Figure 4.13 Probe testing of the plasmonic channel

Figure 4.14 IR imaging of fully (left) and partially (right) covered plasmonic layer under current injection

For both cases, a time dependent temperature measurement was performed. The temperature at the centre of the channel was measured in respect to time using the movie mode of the thermal imaging system. The results are shown in Figure 4.15a & b for the fully and partially covered channels, respectively.

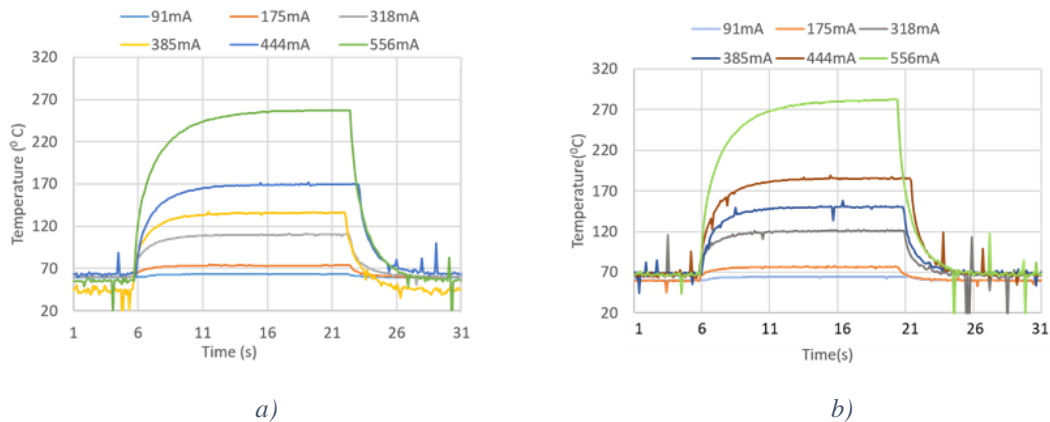
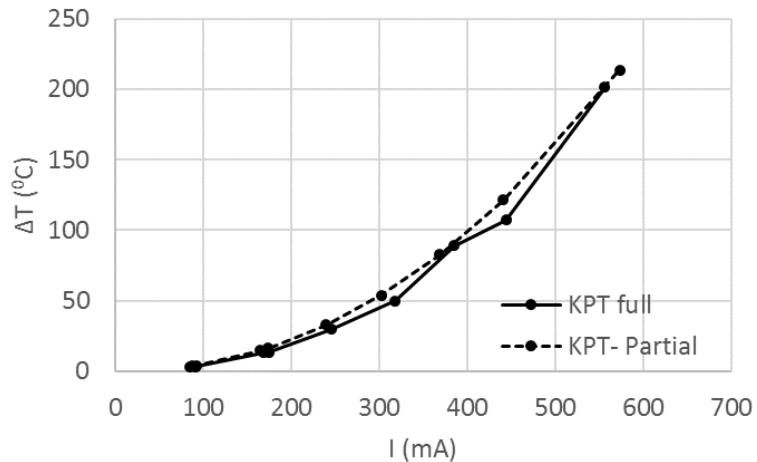


Figure 4.15 Follow-up of temperature at channel center under pulsed injected current a) fully covered channel and b) partially covered channel.

Evolution of the temperature rise (base temperature was removed from absolute temperature value recorded on the thermal measurements) at the centre of channel is shown in Figure 4.16. Almost the same behaviour is obtained. Partially covered channel might exhibit a slightly higher temperature that could be linked to the observation of modelling results (see Figure 4.9) indicating that covering the channel with Kapton decreases slightly the temperature.



*Figure 4.16 Comparison of temperature at channel center for fully and partially covered layer.*

The fully covered channel case corresponds to the wKPT case of the theoretical study. Both experimental and theoretical results are then represented in Figure 4.17 (we limited the graph to moderate current values since temperature rises above 100°C are not of concern for biological experiments). A good agreement is obtained.

From results presented in Figure 4.15, the rise time can also be evaluated. It is presented in Figure 4.18 for both cases. Comparing to the theoretical result (wKPT case) presented in Figure 4.10, we can first notice that experimental and theoretical mean rise time values are of the same order. However, experimental rise time (1.25 s) is lower than the theoretical one (1.75s). The major difference is observed of the trend of the curve versus injected current: increasing of current leads to a decrease of rise time in the modelling as the reverse is observed experimentally. Anyhow, this value between 1 s and 1.5 s is reasonable for conducting biological experiments since it is compatible with the reaction time of biomolecular events.

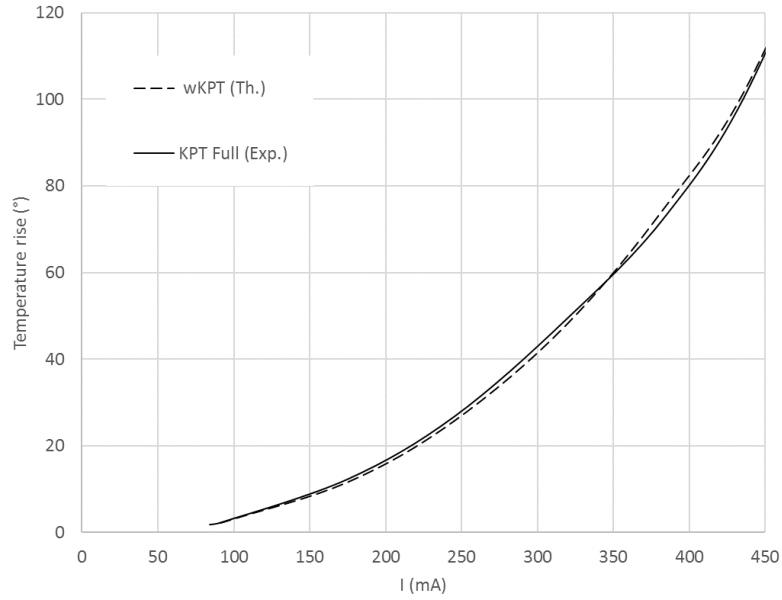


Figure 4.17 Comparison between experimental (KPT full) and theoretical (wKPT) temperature rises versus injected current.

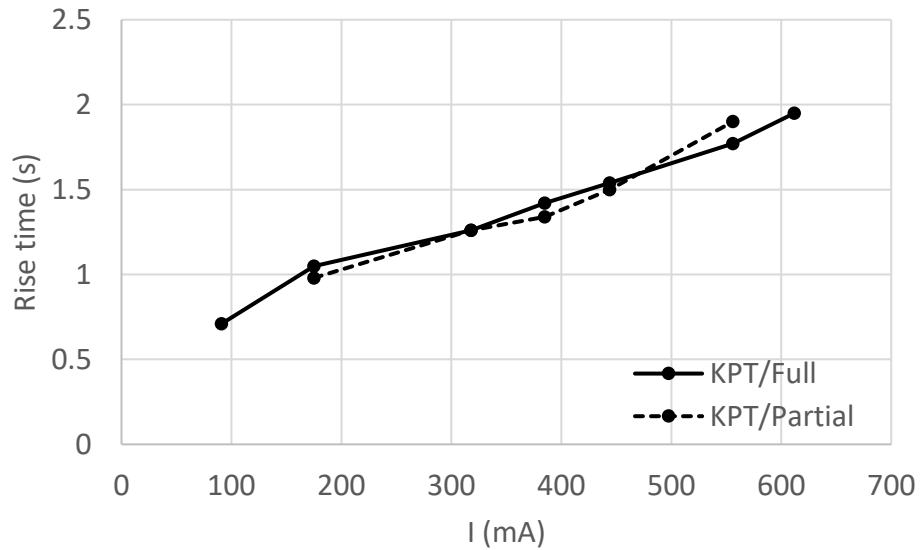


Figure 4.18 Experimental rise times versus injected current.

Analysing images like presented in Figure 4.14 can also give the cross-sectional temperature rise of the plasmonic channel. It is represented in Figure 4.19 for different injection currents; it is also compared to theoretical predictions (see Figure 4.8).

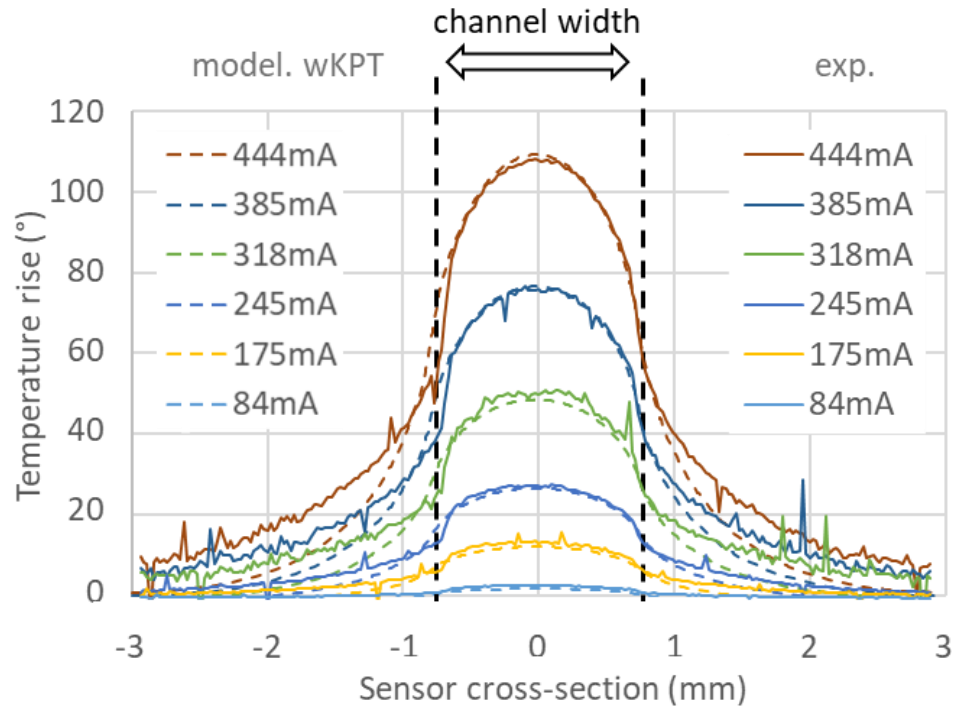


Figure 4.19 Cross-sectional temperature rise distribution versus injected current. .

It can be noticed that the temperature falls quickly at the sides of the plasmonic channel. This phenomenon gives a way for locally controlling the temperature of a plasmonic channel without affecting neighbour channels.

By comparing, the theoretical and experimental cross-sectional temperature profiles, are in good agreement within the channel width but, outside the channel, the experimental ones exhibit a lower temperature decrease. This can be linked to a too low  $C_p$  value for glass in the modelling. Nevertheless considering our sensor configuration with a channel separation of 4mm edge to edge (see § 4.2), no temperature crosstalk should be observed for the moderate temperature rises (around 60°C maximum value) that will be used in biological experiments.

#### 4.6 Thermal measurements on SPR experiment.

Thermal behaviour has been tested on the spectral interrogation bench presented in § 3.2. Two needle probes have been used in order to inject the current in the channels (Figure 4.20).

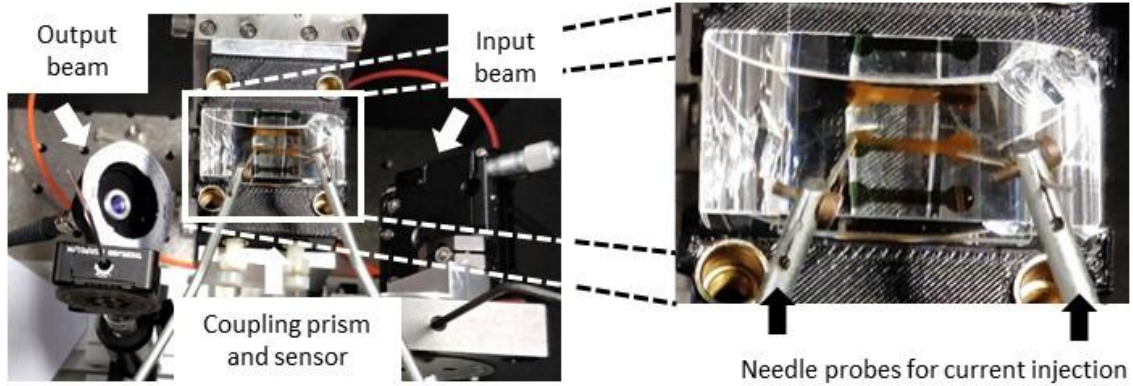


Figure 4.20: Top view of spectral interrogation scheme based SPR set-up including two needle probes mounted on micro-positioners for current injection (zoomed view on right).

For the thermal behaviour testing, a deionized water drop was deposited over a channel and current was injected into the plasmonic layer. The driving currents and corresponding temperatures are reported in Table 4.2. Maximum temperature rise is that at channel centre and mean temperature rise is the mean value of temperature over the full channel width taking into account the lateral profile shown in Figure 4.19. An algebraic mean value has been calculated which shall not be the right way to obtain this mean value but it gives an idea of the difference between maximum and mean value especially its evolution when absolute value of temperature is increasing.

Current (mA)	Maximum temperature rise (°C)	Mean temperature rise (°C)	Max-mean difference (°C)
0	0	0	0
100	6.3	4.2	2.1
150	12.1	8.3	3.8
200	19.8	15.8	4
250	30.1	26.0	4.1
300	44.0	38.6	5.4
350	61.9	54.1	7.8

Table 4.2 Driving currents and corresponding temperatures rises.

Figure 4.21 reports the modification of the refractive index that has been calculated from the experimental SPR measurement and the theoretical one. The reference refractive index is the one corresponding to 20°C that is the base temperature, i.e. without any current injection. The theoretical curve is obtained using the water refractive index variation versus

temperature given in [122]. For the experimental curves, both maximum and mean values of temperature (mean value is a "basic" algebraic mean value, it would not reflect the exact mean temperature value as would be determined by thermal laws) rise have been used as parameters (see Table 4.2). The variation of refractive index ( $\Delta RI$ ) is obtained from the plasmonic response shift using the calibration data presented in Figure 3.16. We can notice that a rather good agreement is obtained between experimental and theoretical curves as far as the mean value of temperature rise is taken into account. It has to be mentioned that no influence of current injection on the plasmonic response has been inserted in the calculations. Following the modelling presented in [123], no incidence on the part of the plasmonic response that is used for the determination of the plasmonic shift (bottom of response curve) should be expected. Nevertheless, such a modelling might be done, mainly to check if the influence of high current densities could explain the increasing discrepancy between experimental and theoretical curves when current (and so temperature) is increased.

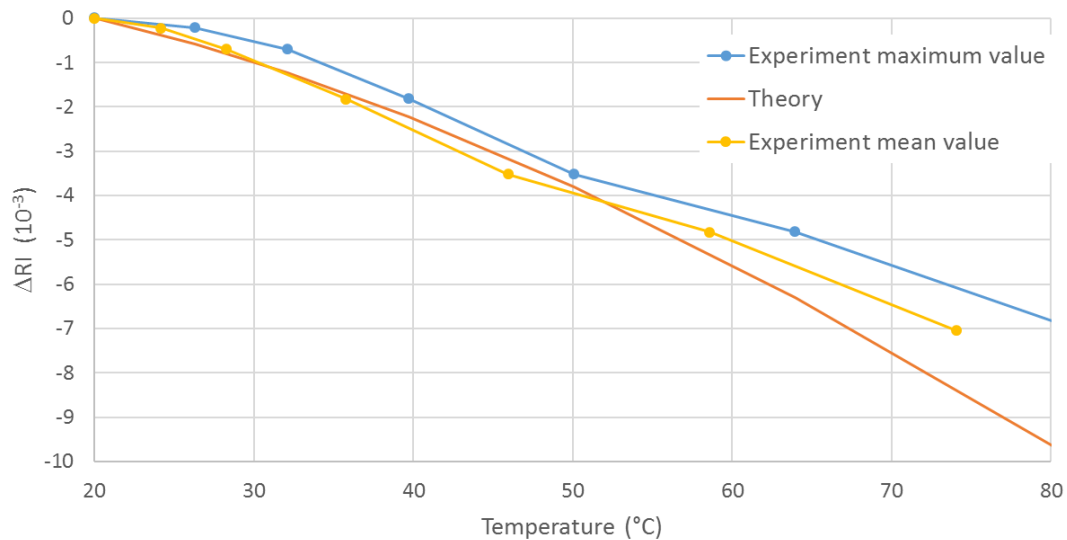


Figure 4.21 Variation of the refractive index of a heated water drop.

#### 4.7 Inbuilt-real time temperature sensor

In previous experiments, we demonstrated that the temperature rise due to current injection can be determined knowing the characteristics (dimensions, film resistivity) of the

plasmonic channel. Nevertheless, targeting a portable equipment working on fluidic solutions, several matters can be controversial:

- even if the temperature rise obtained by Joule's heating can be precisely determined, the absolute temperature is not. Up to now, ambient laboratory temperature has been used. It is known, commonly, with a precision that is lower than that of the Joule's heating and can then bring higher incertitude on the absolute temperature than the developed process. Moreover, integrating the whole bench in a portable equipment and outside operation will increase the incertitude of the temperature surrounding the sensing area.

- up to now, validation tests have been made using a drop of fluid. Using a real fluidics flow can modify the temperature since "fresh" fluid is continuously launched onto the sensor.

- as it has been seen on cross-sectional temperature profile on channel width which a zoom is shown on Figure 4.22, there is a temperature gradient from channel centre up to channel edges that put some uncertainty on the effective temperature of the sensed medium, moreover when a fluidics flow will be used. A consequence of this temperature gradient has been potentially pointed out in the results shown in Figure 4.21.

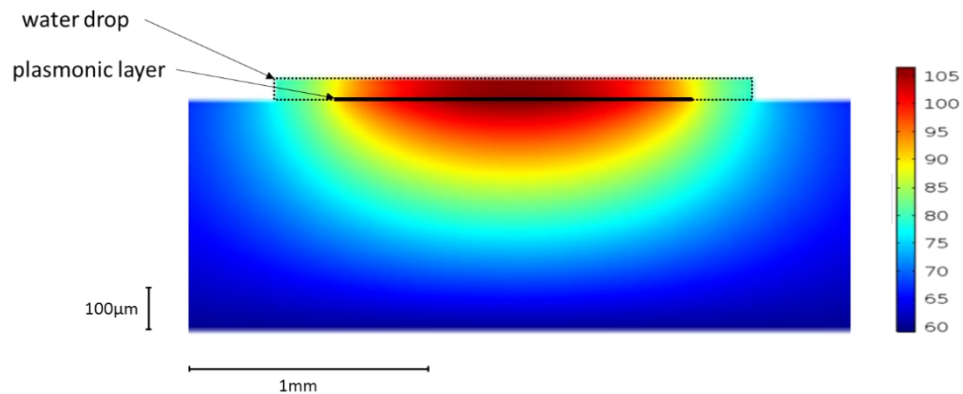


Figure 4.22 2D heatmap of the plasmonic layer close environment.

In order to circumvent those points, we decided to integrate a platinum (Pt) temperature sensor directly onto the channel that will be used to monitor the absolute temperature of the fluids at measurement point. The Pt resistor is commonly used as a temperature sensor since Pt has an accurate resistance/temperature relationship. Before implementing the

temperature sensor on the plasmonic channel, some tests have been made to calibrate the Pt film that will be used.

#### 4.7.1 Pt film calibration

IEC standard platinum has a temperature coefficient,  $\alpha$ , of  $0.003851 \text{ } \Omega/\text{ }^\circ\text{C}$  [124]. Nevertheless, this value can be dependent on the way platinum is fabricated. We decided to measure the temperature coefficient of the Pt material that we will use. Pt film was so deposited on a glass substrate using e-beam evaporation. Different  $300\mu\text{m}$ -wide wire lengths, from 1.5 mm to 20 mm were fabricated (see insert in Figure 4.24). The targeted thickness of the film was 50nm. Its observation by SEM was nevertheless slightly less, 45nm (Figure 4.23).

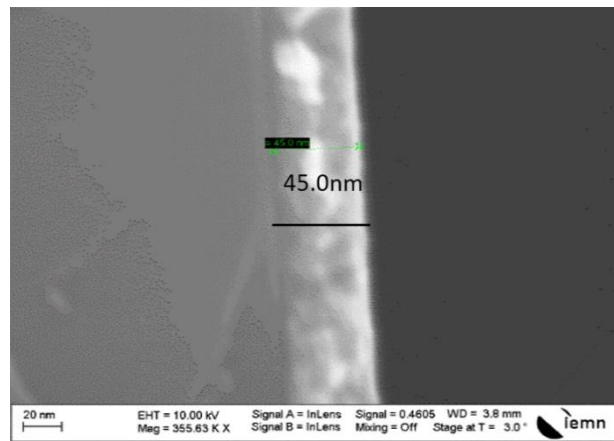


Figure 4.23 Thickness of Pt film

The resistance of fabricated Pt resistors ( $300\mu\text{m}$  wide, 2 to 20 mm long) was measured at room temperature ( $20^\circ\text{C}$ ) using a 4-probes system (Figure 4.24). The resistivity ( $@20^\circ\text{C}$ ) was determined to be  $1.72 \times 10^{-7} \text{ } \Omega\cdot\text{m}$ . Concurrently, the resistivity of a Pt film elaborated the same manner, but in a different processing batch, and deposited “full-wafer” on a glass slide was measured to be  $1.88 \times 10^{-7} \text{ } \Omega\cdot\text{m}$  using a resistivity measurement set-up. Those values are in good agreement taking into account the tolerance on film thickness due to fabrication.

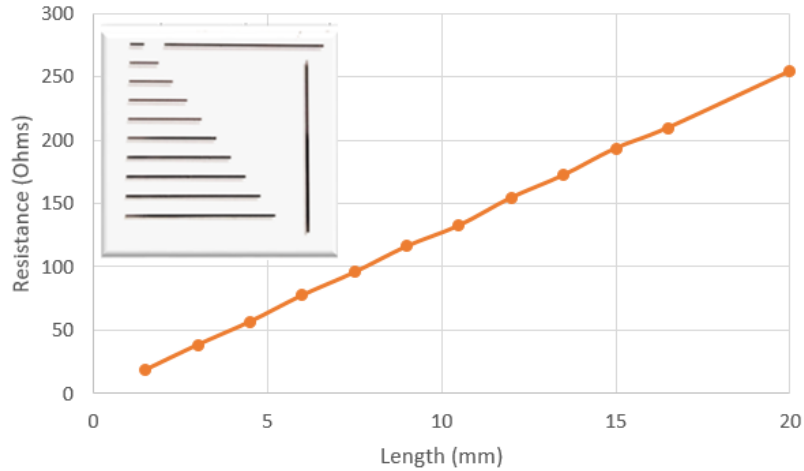


Figure 4.24 Measurement of 300  $\mu\text{m}$ -width Pt resistance for various lengths (@20°C and for a 45 nm-thick film).

Pt resistors as used in the SPR sensor (see Figure 4.26) were then measured versus temperature. They are 45nm thick, 1.5mm long and 75 $\mu\text{m}$  wide. For those dimensions, their expected resistance at room temperature (20<sup>0</sup>C) is  $80 \pm 3.5 \Omega$ .

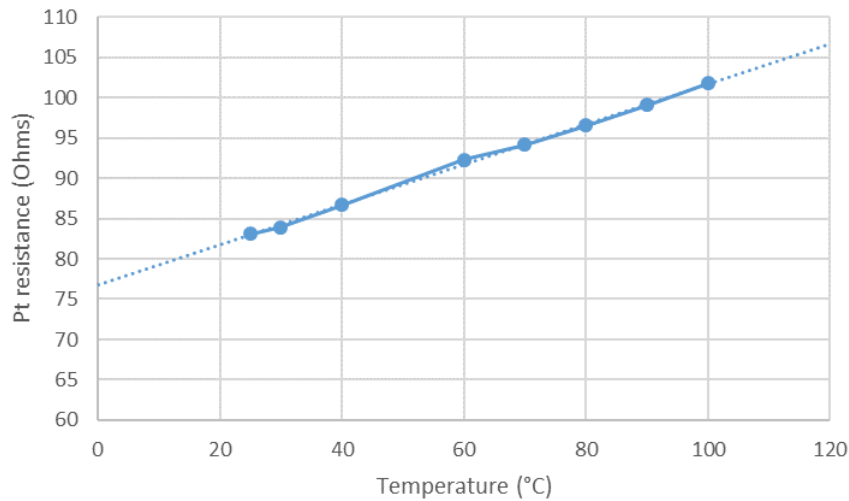


Figure 4.25 Calibration of Pt resistance.

For that purpose the sensor were placed on the hot plate of the thermal camera and needle probes were used to measure the Pt resistance on varying chuck temperature (Figure 4.25). The temperature coefficient,  $\alpha$ , has been determined to be  $3.2 \times 10^{-3} / ^\circ\text{C}$ , that is slightly less than the commonly used value ( $3.8 \times 10^{-3} / ^\circ\text{C}$ ) for Pt. This could be linked to the low temperature anneal that is here used (300°C) compared to the one that is used on usual Pt

thermistor (around 550-650°C) [125]. The resistance of Pt at room temperature, i.e. 20°C, is extrapolated to be 81.7Ω that leads to a Pt thickness close to 44 nm that is consistent with above measurements.

#### 4.7.2 Design and fabrication of the multichannel SPR sensor integrating temperature sensor

##### 4.7.2.1 Design

A small modification was made on channel/plasmonic layer design in order to add supplementary contact pads for current injection. A Pt sensor has been integrated on each channel. The resistor is placed on the center of the channel width and on one side of channel length. Its width and length are 75μm and 1.5mm, respectively. Considering the calibration reported in §4.7.1, the resistor value should so be 76.8 Ω at 0°C. As the sensing place is roughly at the middle of the channel length, further experiments (not made during this work) will allow to determine if temperature sensing would have any importance when made downstream or upstream the measurement zone.

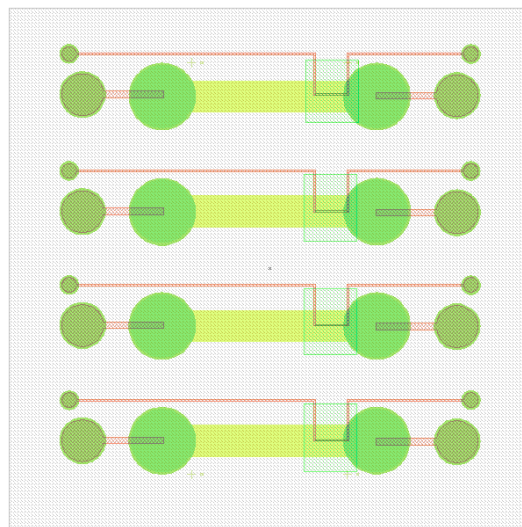


Figure 4.26 layout of one SPR channel including a temperature sensor

Figure 4.26 shows the layout of the sensor. Largest green circles are the place of fluidics in and out, smallest green circles are for DC probing (medium size is for current injection into the channel and small ones for Pt resistor measurement).

#### 4.7.2.2 Fabrication

Except the technological steps that are needed to fabricate the sensor, some other ones are added in order this sensor not to be short-circuited by either the plasmonic layer or the sensed fluid. Two steps of Atomic Layer Deposition (ALD) of an  $\text{Al}_2\text{O}_3$  film are then inserted for that purpose.

The integration of the Pt sensor requires much more fabrication steps than the basic one. Start of fabrication, i.e. obtaining a 4-channel sensor device is identical as the one presented in Figure 4.3a. Supplementary steps are the added to fabricate the temperature sensor:

- 1) full surface deposition of  $\text{Al}_2\text{O}_3$  (50nm) film by ALD technique at  $300^\circ\text{C}$
- 2) laser lithography for delimitating the  $\text{Al}_2\text{O}_3$  surface area (under Pt resistor and its connection) in order to avoid the Pt sensor short-circuited by the plasmonic layer
- 3) chemical etching of  $\text{Al}_2\text{O}_3$ . The photo resist developer solution (AZ-400K) is used for that purpose; the etching rate of  $\text{Al}_2\text{O}_3$  is non linear and 13 minutes are requested to etch completely the 50nm-thick film
- 4) laser lithography for delimitating the Pt sensor
- 5) metalization (e-beam evaporation) of Pt film (50 nm) and lift-off process
- 6) laser lithography for Pt resistor connection to pads
- 7) metalization (e-beam evaporation) of Au film (500 nm) and lift-off process
- 8) repeat of steps 1) 2) and 3) in order to avoid the Pt sensor short-circuited by the fluid

Figure 4.27 resumes the main fabrication steps.

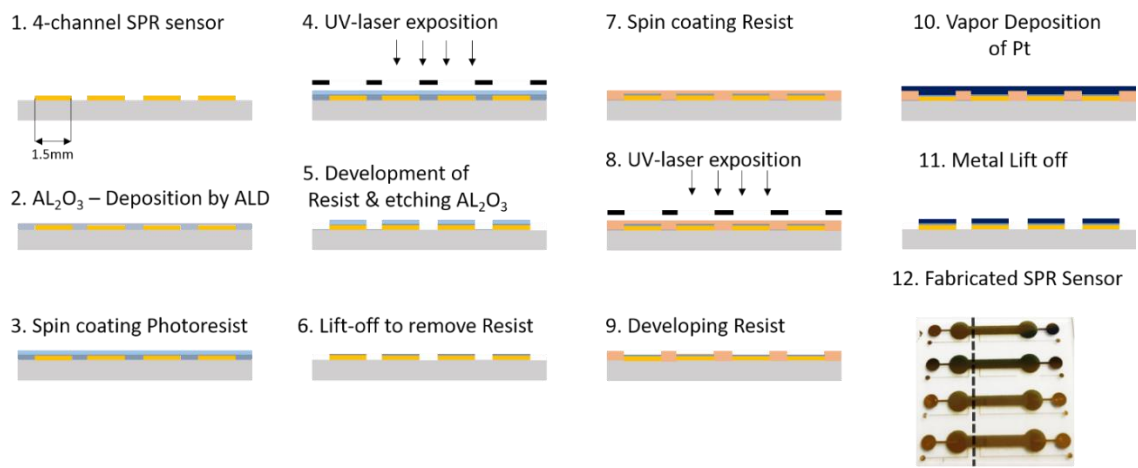


Figure 4.27 Main fabrication steps of multichannel sensor with integrated temperature sensor.

#### 4.7.3 Modelling of SPR sensor with Pt resistor.

The modelling has been built up based on the previously developed one on COMSOL (see § 4.4). Figure 4.28 represents the simulated structure (one channel). Identically to previous modelling scheme, modelling window has been narrowed in order to reduce calculation time.

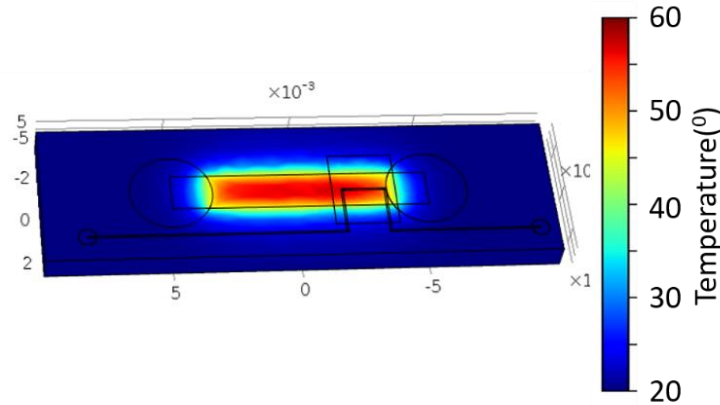


Figure 4.28 Heatmap of channel including Pt resistor under current injection, here it is 245mA.

The presence of  $\text{Al}_2\text{O}_3$  film has been investigated in order to check its effect on temperature gradient whatever it is between plasmonic layer and sensor or sensor and fluid since same thickness of  $\text{Al}_2\text{O}_3$  is used for both cases. The corresponding parameters are  $\rho = 3965 \text{ kg/m}^3$ ,  $K = 2.25 \text{ W/(m.K)}$  and  $C_p = 755 \text{ J/(Kg.K)}$ .

I (mA)	Difference in $\Delta T$ ( $^{\circ}\text{C}$ ) due to various $\text{Al}_2\text{O}_3$ thickness.							Tolerance $\pm$ $^{\circ}\text{C}$
	40nm	50nm	60nm	70nm	80nm	90nm	100nm	
84	1.505	1.511	1.514	1.512	1.514	1.516	1.512	0.0032
91	1.553	1.56	1.563	1.56	1.563	1.566	1.561	0.0037
168	0.221	0.245	0.256	0.247	0.254	0.264	0.248	0.0125
175	0.207	0.233	0.244	0.234	0.243	0.253	0.236	0.0133
245	0.495	0.443	0.419	0.44	0.423	0.402	0.437	0.0271
318	1.33	1.24	1.2	1.24	1.21	1.17	1.23	0.0464
385	0.8	0.66	0.6	0.65	0.61	0.55	0.64	0.0722
444	0.69	0.88	0.97	0.89	0.95	1.03	0.9	0.099

Table 4.3 Calculated temperature drop due to various thickness of  $\text{Al}_2\text{O}_3$  deposited on top of plasmonic layer.

As can be seen from Table 4.3, thin film of aluminium oxide affects slightly the temperature rise at the metal plasmonic channel. Proportionally, it impacts more low temperature increase (low injected current) than high injection levels.

#### 4.7.4 Thermal characterization

##### 4.7.4.1 Thermal IR imaging

The characterization set-up is the same as used in § 4.5.1.SPR sensor including Pt resistors was placed on the chuck of the thermal imaging system. Current was injected through the plasmonic channel and the rise in the temperature due to injected current was determined. A view of a sensor under test is shown in Figure 4.29a) in a case where two different currents are injected in adjacent channels. As for previous experiments, temperature at channel centre was recorded and compared to the modelled one (Figure 4.29b). Agreement between theoretical and modelled value is good and replicates that obtained on sensor without Pt resistor (see Figure 4.17). Such behaviour was almost predictable since the Pt resistor shall not modify the Joule's effect in the plasmonic layer.

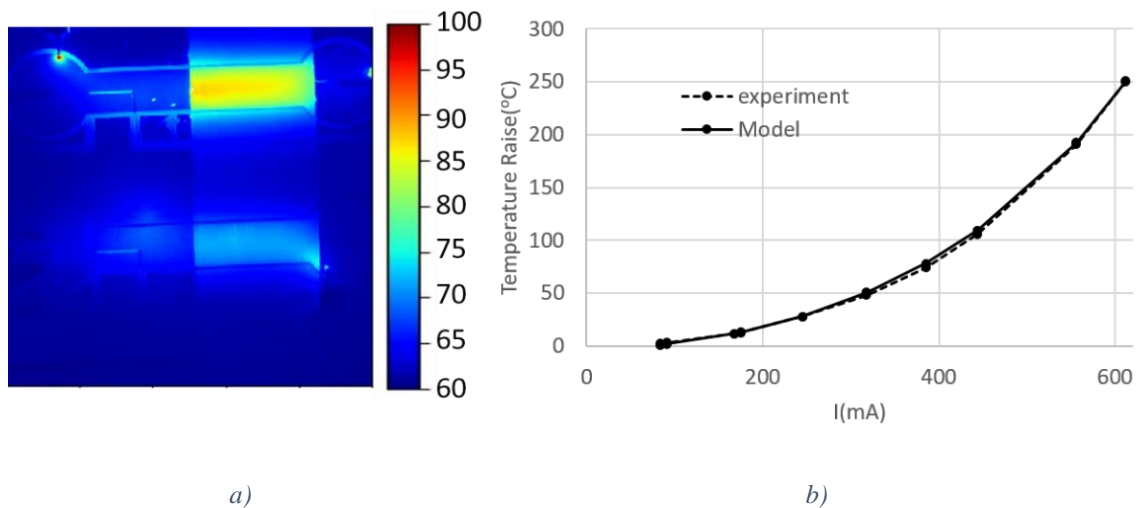


Figure 4.29 a) Thermal camera image for 245mA current injection in the first channel (top) and 168mA in the second channel (bottom), b) temperature raise at the centre of channel..

The temperature has been measured by the thermal IR imaging and jointly using the Pt sensor. The direct measurement of Pt sensor resistance value versus injected current is shown in Figure 4.30.

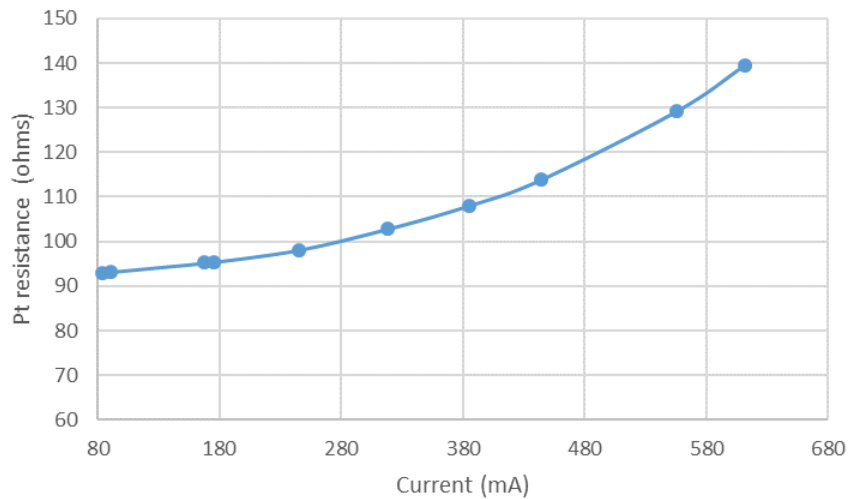


Figure 4.30 Pt sensor resistance value versus injected current.

From calibration data, those resistance values have been converted into temperature values and compared to temperature obtained under thermal imaging (Figure 4.31). We can see a good agreement between thermal IR imaging and Pt resistor determined values up to roughly 350 mA, i.e. temperature rise around 60°C.

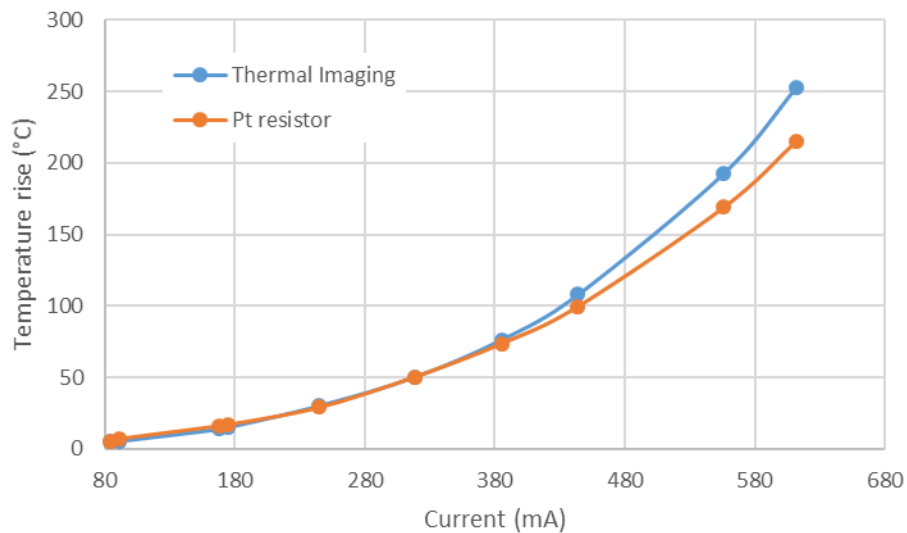


Figure 4.31 Compared temperature versus injected current from thermal imaging (value at channel centre) and thermal imaging measurements.

Comparing to SPR water experiments (see §4.6 and Figure 4.21), it can be noticed that this discrepancy between experimental results and theoretical predictions arise almost for the

same temperature range, i.e. around 50 – 60°C temperature rises. Applying the same "basic" correction to the measured temperature of the sensed medium, i.e. not taking the maximum value but a "mean" value, the temperature determined by the two methods correlate better (Figure 4.32).

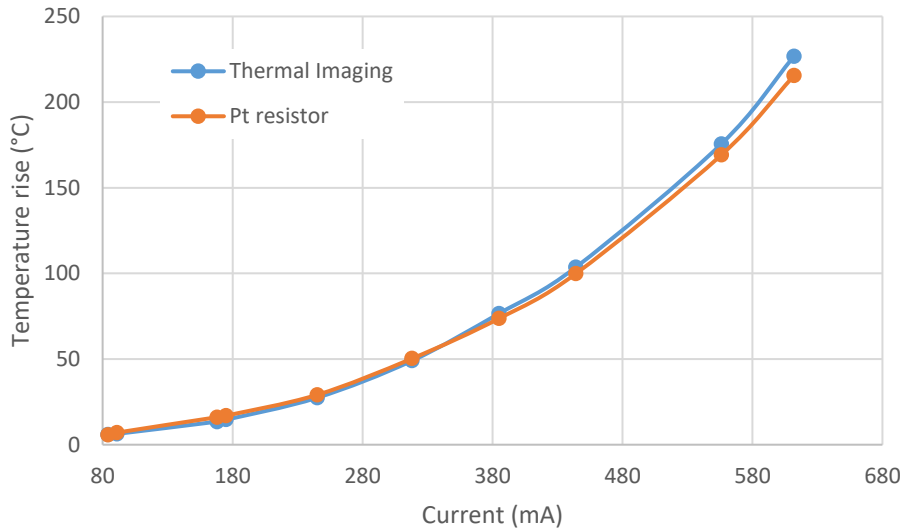


Figure 4.32 Compared temperature versus injected current from thermal imaging ("mean" value calculated using an algebraic mean formula) and thermal imaging measurements.

Increasing discrepancy is still observed for the higher temperature rises as it was also observed on SPR measurements reported in Figure 4.21. There are so some conclusions concerning those observations:

- as it could have been intuitively forecasted, the maximum temperature rise is not the real temperature of the sensed medium. Obviously, it is the simplest parameter to correlate modeling and thermal imaging temperature measurements,
- even if the current way calculating the real value of temperature within the sensed medium is not the right one (basic algebraic mean value calculation), it allows approaching much more the results obtained in SPR measurements and using the Pt sensor for high current levels and so high temperature range.
- always using this "mean" temperature assumption, the more and more pronounced bell-shape of the temperature cross-section profile over the channel width might explain the non-linear discrepancy that is observed,

- Pt sensor temperature measurements are more representative of the "real" temperature of the medium that SPR measurement is sensing and, more especially, for moderate temperature rises, i.e. up to 50-60 °C as it can be encountered in main biomolecular experiments.

#### 4.7.5 Improved 4-channel device design

In order to have a fluidics integrated design, the 4-channel layout has been modified. Effectively, a chemical bonding technique has been developed [126] to bond PDMS fluidics directly onto gold surface. The actual design of the 4-channel device that presents glass surface outside the channel, i.e. where PDMS fluidic stamp shall be bonded, do not allow this process to be used. The layout of the sensor has been modified to provide a gold surface almost everywhere and so allowing the PDMS stamp bonding.

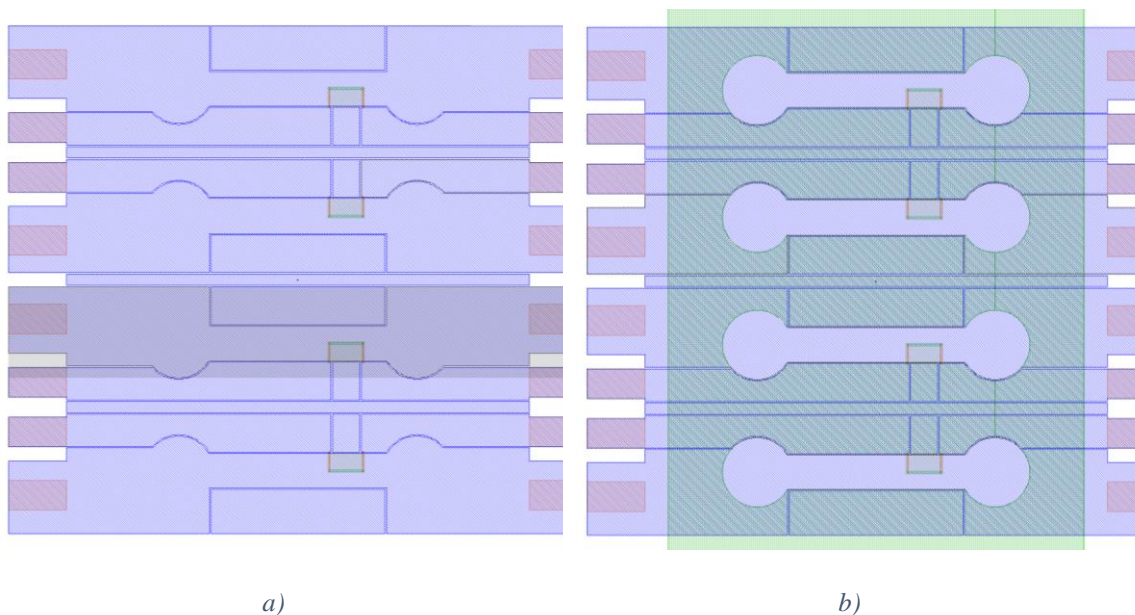
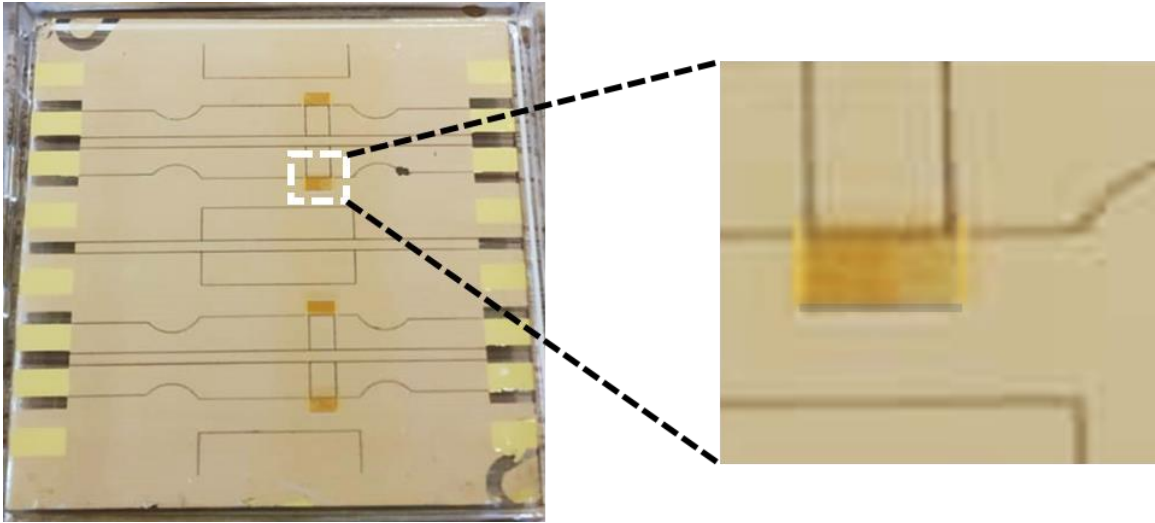


Figure 4.33 Modified 4-channel layout: a) electrical connections have been made wider in order to lower access resistances and electrical pads have been made compatible with commercial connector (here USB) to ease electrical connections of all channel and Pt sensors simultaneously on the experimental bench, b) PDMS fluidics cover is shown in order to visualize the SPR channels.

In order to facilitate the electrical connections which number becomes significant and may cause some congestion on test bench, electrical contact pads have been arranged as those existing on a USB connector. There are so 8 rectangular contact pads each side of the sensor

that can be all together connected using modified commercial USB connectors. Figure 4.33 shows the layout of this device and Figure 4.34 a picture of fabricated sensor. Except a different layout design, the fabrication steps are the same than for the previous 4-channel device (see § 4.7.2.2).



*Figure 4.34 Modified layout 4-channel SPR sensor with integrated temperature sensor on each channel. Zoom shows the Pt resistor sensing area (gold colour is related to the  $Al_2O_3$  surface area).*

## 4.8 Validation of multi-channel temperature operation

The other advantage of the Joule's heating is to afford the possibility controlling independently each channel temperature.

### 4.8.1 Experimental validation using thermal IR imaging

Current has been injected simultaneously in two adjacent channels (Figure 4.35). On these heatmaps, we can particularly notice a clear delimitation of heated zones. The corresponding temperature cross-sections are shown in Figure 4.36. On this figure, temperature rises are shown, i.e. base temperature of thermal IR imaging system has been subtracted.

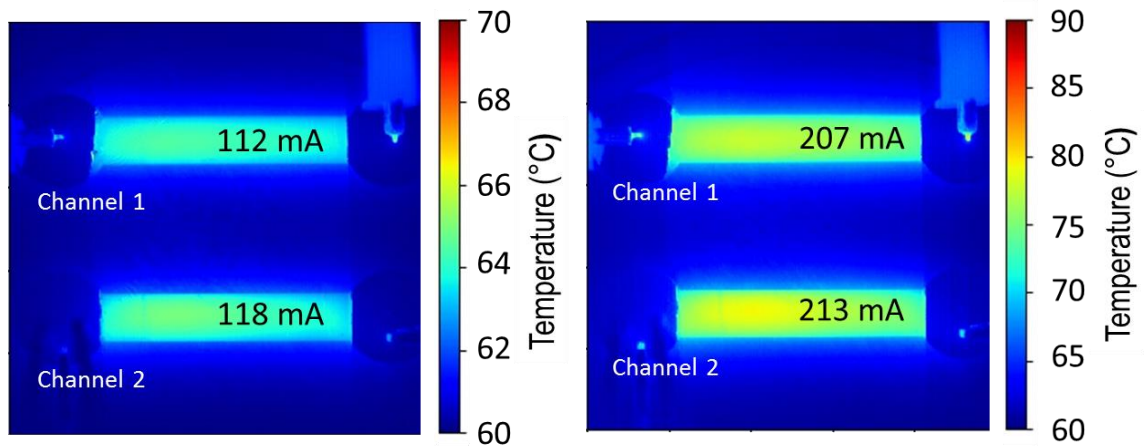


Figure 4.35 Slightly different currents are injected in two adjacent channels: heatmaps obtained under thermal IR imaging.

In Figure 4.36, this temperature delimitation is also clearly observed. It can also be observed a fine temperature control on each channel with no crosstalk.

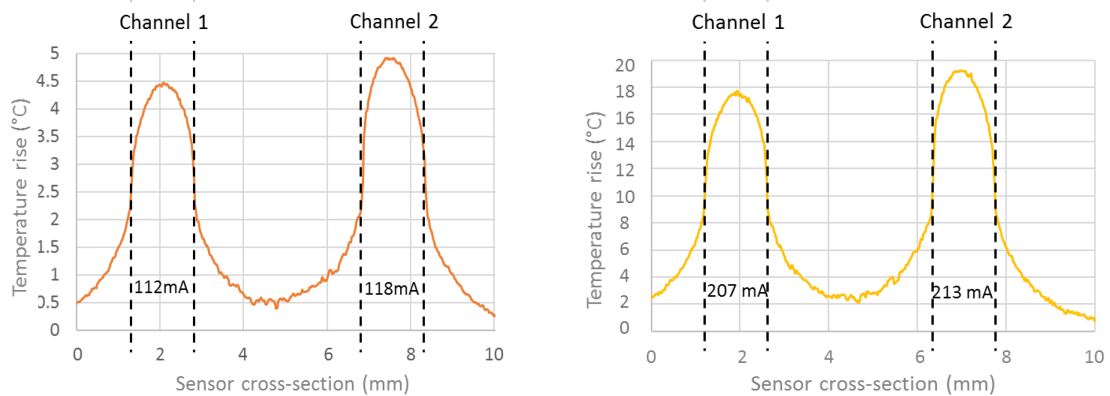


Figure 4.36 Corresponding temperature rise cross-section profiles of thermal IR images of Figure 4.35.

We saw in the modelling section (see for example Figure 4.19) that, for higher current injection levels, the temperature gradient outside the channel can lead to non-return to zero temperature rise. We injected a high current value in one channel, 355 mA, and checked the temperature crosstalk in an adjacent channel (Figure 4.37b). For those "extreme" conditions, a crosstalk of a mean value around 2°C is observed.

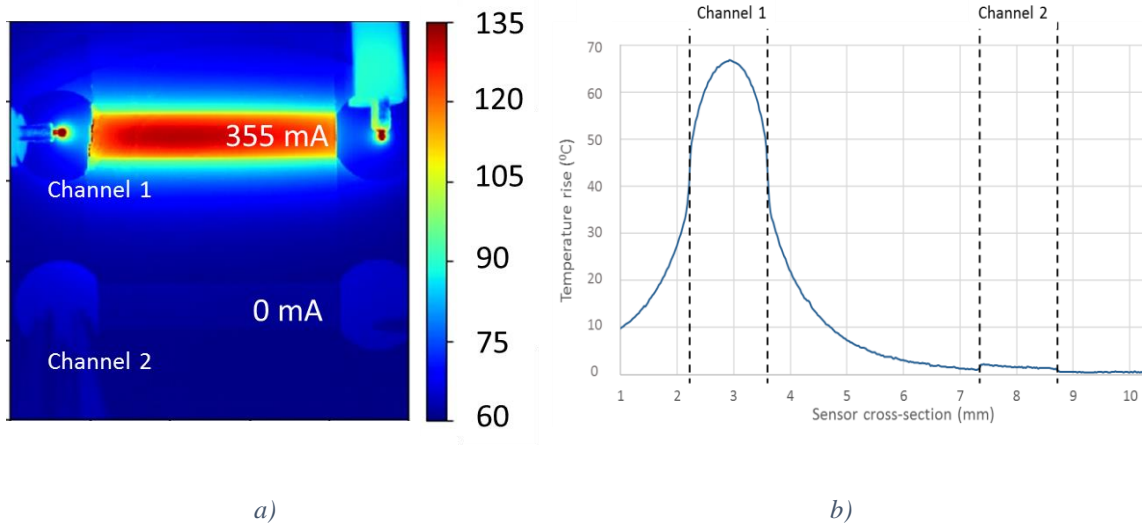


Figure 4.37 Evidence of crosstalk for high current levels a) heatmap, b) cross-section temperature rise profile

#### 4.8.2 Experimentation on the improved 4-channel design

In order to check experimentally the effect of layout design on temperature behaviour, two 4 channel sensors, one in each configuration, initial (Figure 4.26) and improved (Figure 4.33), were fabricated simultaneously in order that the thickness of the deposited metal layers are the same. This will allow comparing the temperature behaviour between both configurations, only related to layout considerations. Both sensors were placed on the chuck of the thermal IR imaging system and currents were injected simultaneously in two adjacent channels (Figure 4.38).

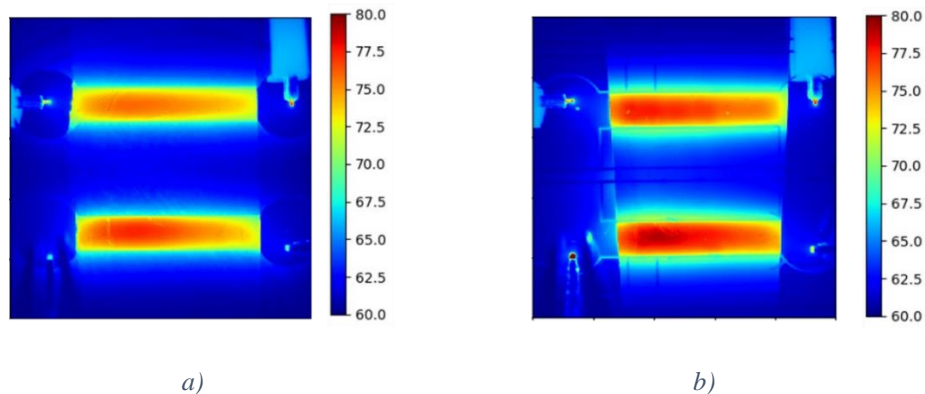


Figure 4.38 Thermal characterization of 4-channel sensor in a) initial and b) improved designs.

The Figure 4.39 represents the temperature profile on both kinds of sensors. Same current is injected in both channels, each time. We can notice that:

- temperature of sensor using improved design is higher than that of sensor using initial design. The difference is increasing as temperature rise increases,
- on improved sensor design, several drops of temperature can be observed. They correspond to the delimitation of the metallic layers. At those locations, the temperature drops to the temperature level of that of initial sensor, i.e. on temperature on glass substrate.

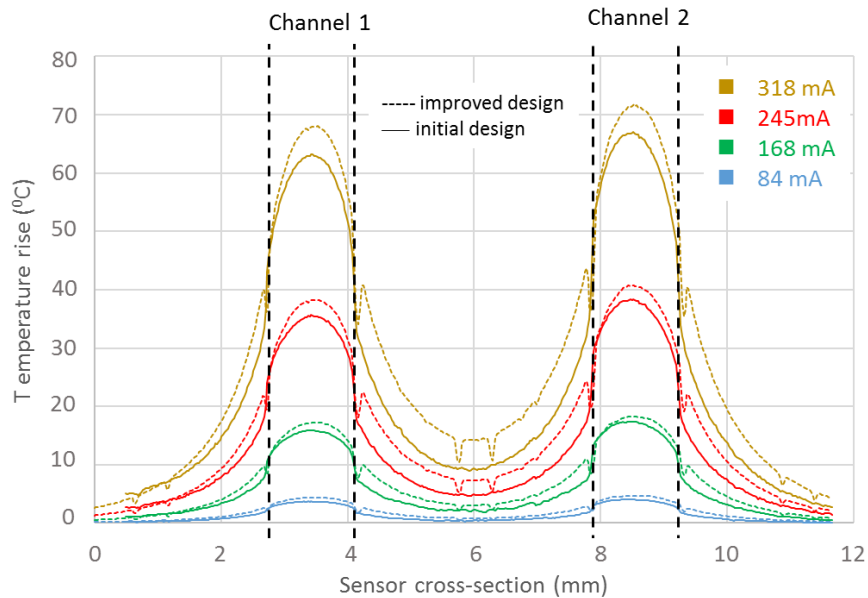


Figure 4.39 Compared evolution of temperature rise depending on sensor design.

Comparing both sensor configurations - initial design with metallic layer only at channel location and improved design with metallic layer almost everywhere, we can so notice a higher mean temperature level for the second one due to lower heat dissipation outside channels.

#### 4.9 Conclusion

In this chapter, we modelled and characterized the use of Joule's heating to control locally the temperature of a SPR channel. We also integrated a temperature sensor, i.e. a Pt resistor,

on the SPR channel in order to get live monitoring of temperature during SPR measurements.

We saw that:

- COMSOL modelling and thermal IR imaging of a SPR channel under current injection give results in good agreement,
- SPR measurements on a heated water drop as well as Pt sensor measurements gave a corresponding value of sensed medium,
- agreements between, on one hand, COMSOL and thermal IR imaging and, on the other hand, SPR and Pt sensor measurements are obtained. However, those two series of measurements do not correlate especially for high values of temperatures; this has been linked to the more and more pronounced bell-shape of the temperature profile across the channel. Taking into account a more realistic "mean" value of temperature (instead of maximum value that was taken for comparing COMSOL and thermal IR imaging results) tends to lower discrepancy at high levels of injection current. A more complete thermal behavior understanding shall be requested to fit perfectly experimental and theoretical values on this range (see Appendix C where a first approach has been launched). Nevertheless, a good agreement is obtained between all results up to temperature rises of 50-60°C that would be enough for most of practical biomolecular experiments.



## Chapter 5: USE OF POLYMER OPTICS FOR SPR

In this chapter, I will present two developments I investigated in order to lower experimental cost of SPR technique and so democratize its use. It was also targeting the possible single use sensor in order the non-specialist user getting free of all cleaning and regenerating issues.



## 5.1 Flexible SPR sensor

As we saw before, we have used a specific glass substrate (H-ZF1) for the sensor fabrication, due to its optical properties matching those of the coupling prism. We planned to fabricate a sensor that is flexible and also cheaper. Simultaneously, we will try to remove the use of matching index liquid for coupling the sensor with the prism that is always a delicate step of the experiment, especially envisaging the use of the system by a non-specialist user. So, we have fabricated a SPR sensor on a 3M™ optically clear adhesive (8213 series) [127] that allows to be set without any matching index fluid on the coupling optics and to be cut into any dimensions that suits the optical setup.

### 5.1.1 Modelling a tape based sensor

The support tape was modelled as a layer of 50  $\mu\text{m}$  thickness (given on manufacturer datasheet). First, both tape and glass-based sensors have been modelled as to be used on the angular interrogation set-up, i.e. at 1550 nm wavelength. Same gold layer, 35 nm-thickness, was used. Figure 5.1 shows the plasmonic response for water refractive index for both glass and tape sensors.

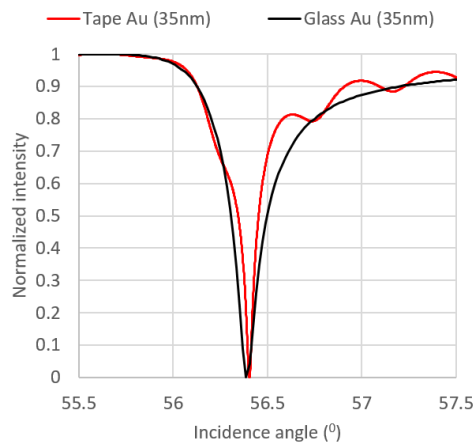


Figure 5.1 Modelled plasmonic response for the glass and tape sensor.

The refractive index of the tape in the near infrared region is 1.473. The coupling prism is always the same (H-ZF1) and its refractive index is 1.62 in the near infrared region. Contrary to when using a glass sensor made up of same material than prism, the use of a

tape sensor that presents a difference in refractive index generates interferences in the response curve (Figure 5.1). Due to this refractive index difference, the resonance angle is also slightly different, by  $0.017^\circ$ . In this modelling, using a tape sensor gives a resonance peak that is sharper compared to that using a glass sensor. The FWHM for the tape and glass sensor is calculated to be  $0.1065^\circ$  and  $0.191^\circ$ , respectively.

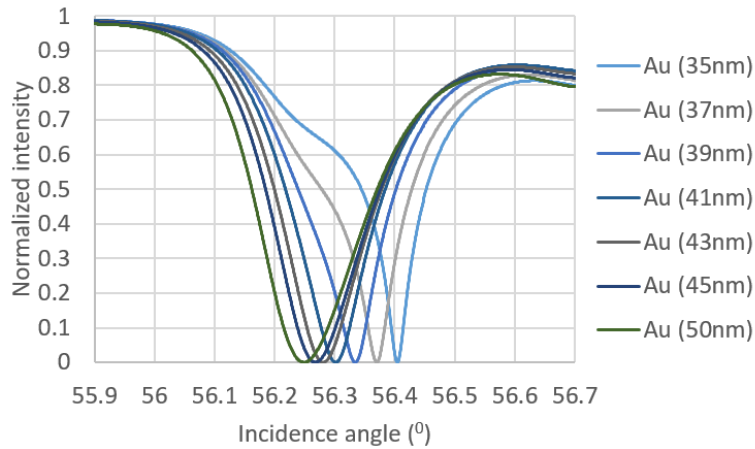


Figure 5.2 Plasmonic responses of tape sensor (1550nm, water, angular interrogation scheme) for different gold layer thicknesses.

Figure 5.2 represents the responses curve of tape sensor for various plasmonic film thicknesses. Sensed medium is water and wavelength is 1550nm in an angular interrogation scheme.

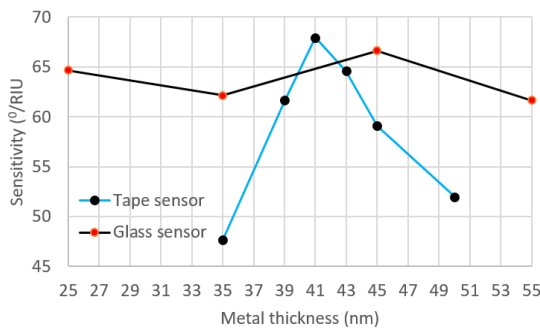


Figure 5.3 Sensitivity of tape sensor depending on plasmonic layer thickness.

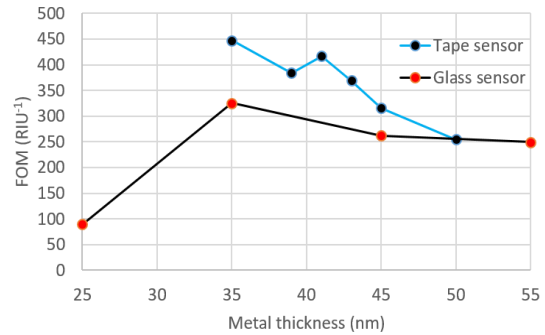


Figure 5.4 FOM values of tape sensor depending on plasmonic layer thickness.

As previously made, the refractive index corresponding to different ethylene glycol solutions have been simulated in order to determine the sensitivity of the sensor. Figure 5.3 and 5.4 shows the deduced sensitivity and FOM values, respectively.

### 5.1.2 Fabrication of tape sensor

The tape film has been just cut at desired dimensions, cleaned with isopropanol to remove any dust particles and air dried. Then the tape received the same metallic layer as a glass-based sensor, i.e. Ti/Au (2 nm:35 nm). Due to the flexibility of the tape, it must be fixed tight during metal deposition. If the mounting of the sample is not tight enough then the metal thickness can be irregular on the tape. The fabricated tape sensor is shown in the Figure 5.5a.

Since the tape is primarily an adhesive, it is backside covered by an adhesive layer (76  $\mu\text{m}$ ) protected by a release liner (50  $\mu\text{m}$ ). Depending on prism material, either those two are be removed (PDMS prism) or only the release liner (glass prism). The release liner is easily removed by peeling off. The adhesive layer is removed using alcohol. At the end of this process, the tape sensor is the only a 50 $\mu\text{m}$  flexible substrate with a plasmonic layer on one side.

### 5.1.3 SPR experiment using tape sensor

Sensor was put on the angular test bench (Figures 5.5 b). The tape sensor is simply deposited on the prism surface after removing the release liner. By using this type of sensor, it was not necessary to use optical matching index liquid to match, the sensor sticks on the prism surface. When observing the image on the CCD camera, vertical lines appear that might be due to interference patterns as observed on modelling results (Figure 5.6).

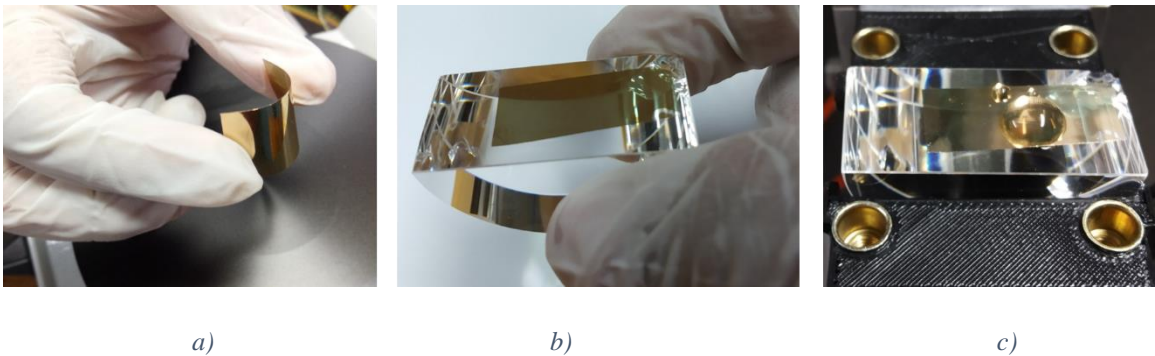


Figure 5.5 Tape sensor: a) after fabrication, b) deposited on the coupling prism and c) with a drop of water on top.

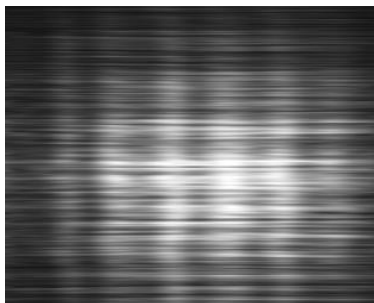


Figure 5.6 Output image of angular test bench when illuminating sensor at 1550 nm.

A drop of water was set on the sensor surface (see Figure 5.5c) to check if any plasmon can be obtained. Indeed, it was (Figure 5.7 a).

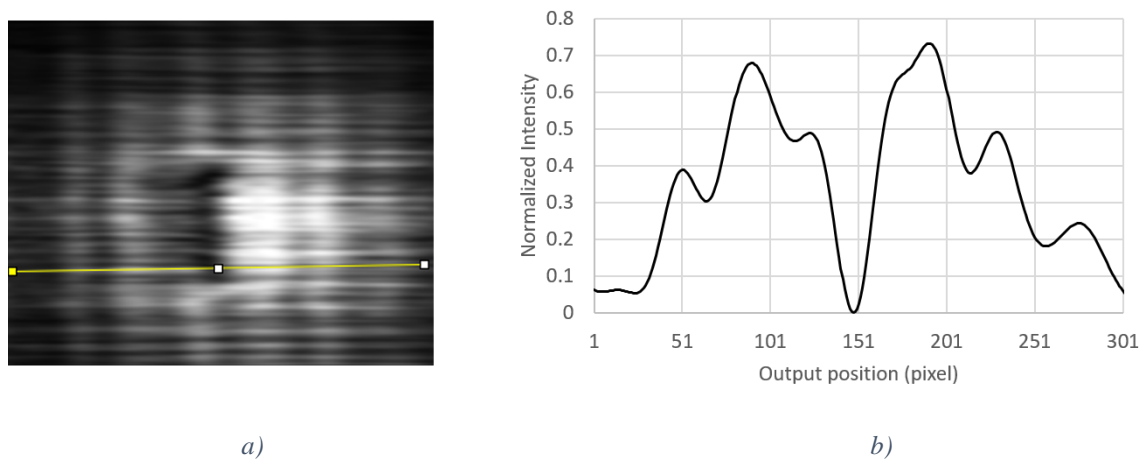


Figure 5.7 Plasmon observed using a drop of water on the tape sensor a) CCD camera image, b) response curve.

The image presents the moiré as previously observed without any water above and a plasmon dip appeared as soon we placed a small drop of water on top of sensor (Figure 5.7 a). The corresponding plasmonic curve reflects the moiré effect but, anyhow, the plasmon response can be clearly distinguished (Figure 5.7b).

This tape sensor was not implemented on the bench with a microfluidics interface. So to measure its sensitivity, we have just used the various ethylene glycol solutions as drops on the sensor surface. Successive concentrations were deposited as drops and after roughly one minute they were removed with a help of absorbing paper. The shift in the plasmonic resonance peak is recorded in function of time as shown in the plot Figure 5.8.

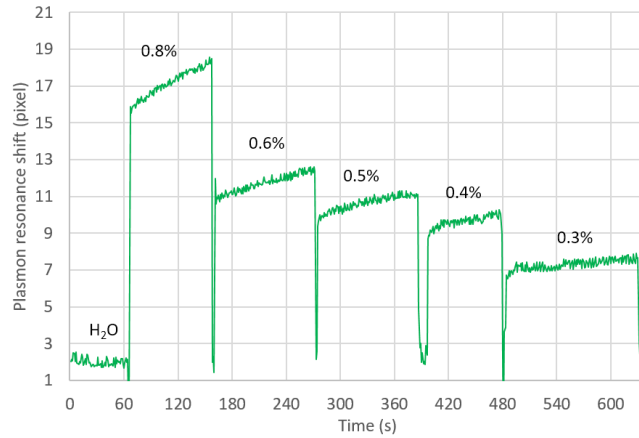


Figure 5.8 Plasmonic response shift versus different ethylene glycol solutions.

Figure 5.9 shows the comparison of experimental and theoretical plasmonic curves. As for glass sensor previously, the gold thickness shall have been increased up to 37nm to perfect the matching of curves.

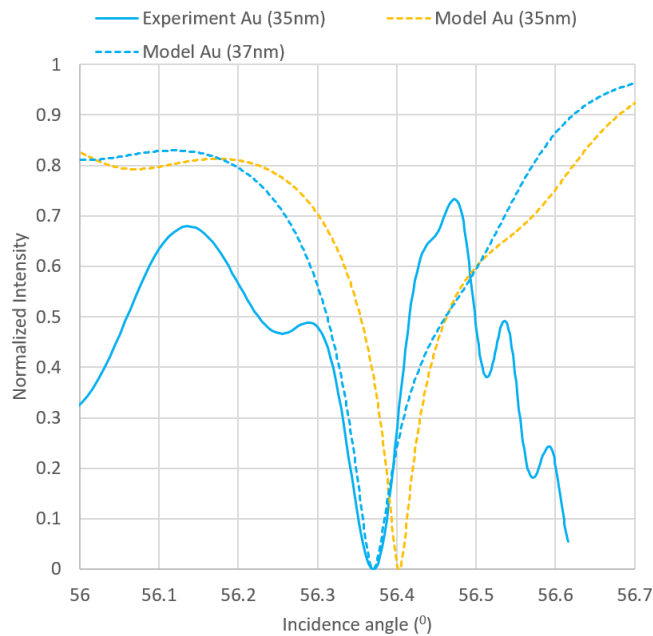


Figure 5.9 Comparison of experimental and theoretical plasmonic responses for tape sensor.

The experimental sensitivity has been calculated replacing ethylene glycol solutions by their respective difference of optical refractive index with that of water and pixel position by its correspondence in angle deviation (Figure 5.10). The sensitivity value is  $53.54^\circ/\text{RIU}$  that matches the predicted value.

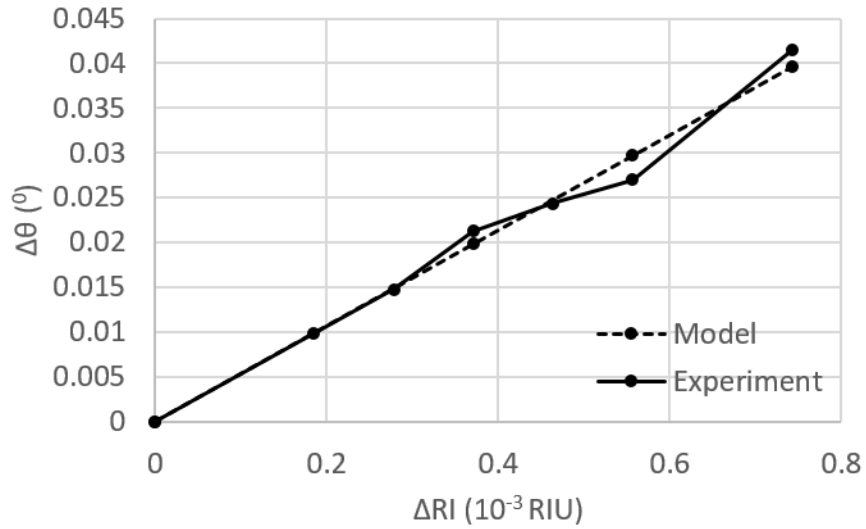


Figure 5.10 Theoretical and experimental sensitivity values of tape sensor.

Two sensors, one on glass substrate and one on tape substrate were fabricated within the same fabrication batch in order obtaining the same metallic layer thickness. Figure 5.11 shows the comparison of experimental sensitivity. The sensitivity of glass sensor ( $66.91^\circ/RIU$ ) is noticed to be slightly higher than that of tape sensor ( $53.54^\circ/RIU$ ).

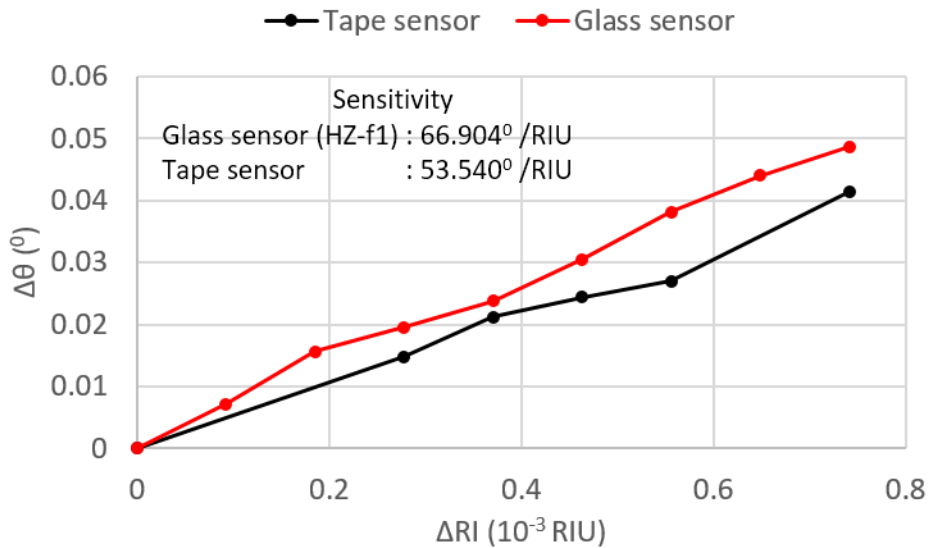


Figure 5.11 Sensitivity comparison of glass and tape sensor.

In order to remove interference phenomenon as well as trying achieving polymer coupling, the use of a PDMS prism was investigated. This is reported in the next paragraph.

## 5.2 Optical coupling prism using PDMS

### 5.2.1 Modelling

Microfluidics that is used is based PDMS (PolyDiMethylSiloxane) material (see Appendix A). Owing to its ease and versatility in fabrication, we decided trying its use for the fabrication of an optical coupling prism. In the PhD progress, the first sensor to be tested with a PDMS prism was the glass (H-ZF1) sensor. So the plasmonic response was calculated by using the combination PDMS prism/glass sensor. The refractive index of the PDMS in the visible wavelength region is 1.4 (as a reminder, H-ZF1 refractive index is 1.639 in visible wavelength region). Here we have modelled the plasmonic response in spectral interrogation scheme. Figure 5.12 shows the plasmonic response using PDMS prism and glass sensor when nothing is set on sensor, i.e. for air as sensed medium. In order to best match with our experimental conditions, the resonance angle for air plasmon was chosen to  $48.25^\circ$  (obviously, this angle changes with the spectral region the plasmonic response is desired to appear).

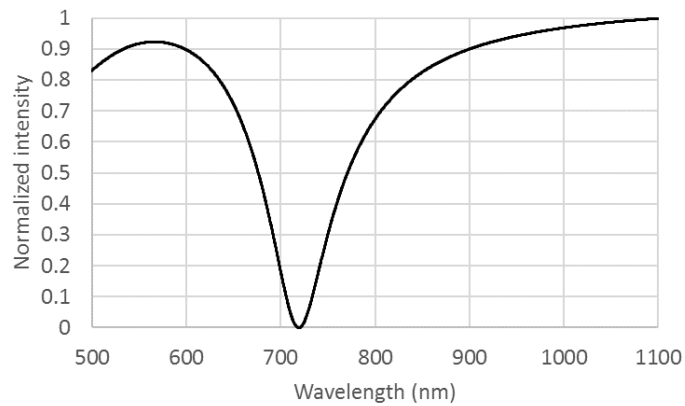


*Figure 5.12 Calculated plasmonic response for air.*

We compare this response with a full glass (H-ZF1), i.e. prism and sensor, scheme. Figure 5.13 shows the comparison of the calculate air plasmon using glass and PDMS prism (sensor is glass). It can be seen that the air plasmon for both the materials shows the same

shape and intensities. Nevertheless, achieving the same spectral response requires the incidence angle to be changed; it is  $39.84^\circ$  for H-ZF1 prism and  $48.25^\circ$  for PDMS prism.

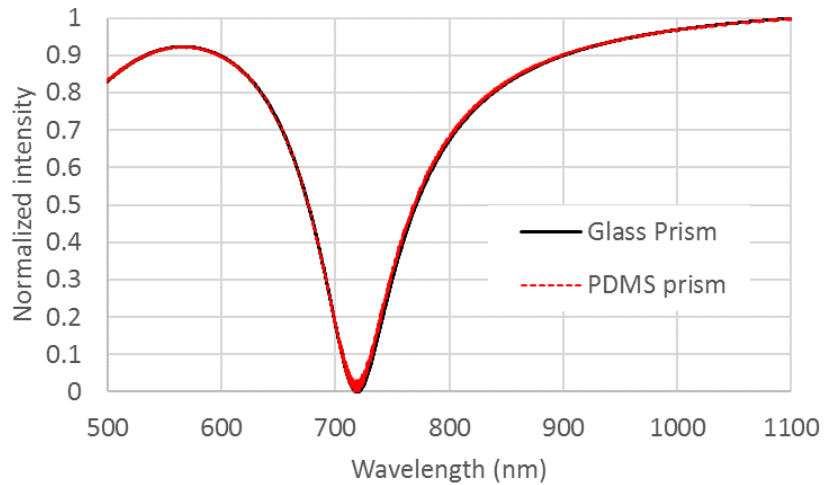


Figure 5.13 Comparison of calculated air plasmon using glass and PDMS prism for  $39.84^\circ$  and  $48.25^\circ$  injection angle, respectively.

We have considered the limitations of our spectral interrogation system (roughly, 500 nm to 1100 nm) and have simulated the shift of air plasmon versus an incidence angle change (Figure 5.14). In order to be located in the maximum amplitude of our experimental bell-shaped system response (around 700-850 nm wavelength range), the incidence angle shall be within the  $48^\circ \pm 0.5^\circ$  angle range.

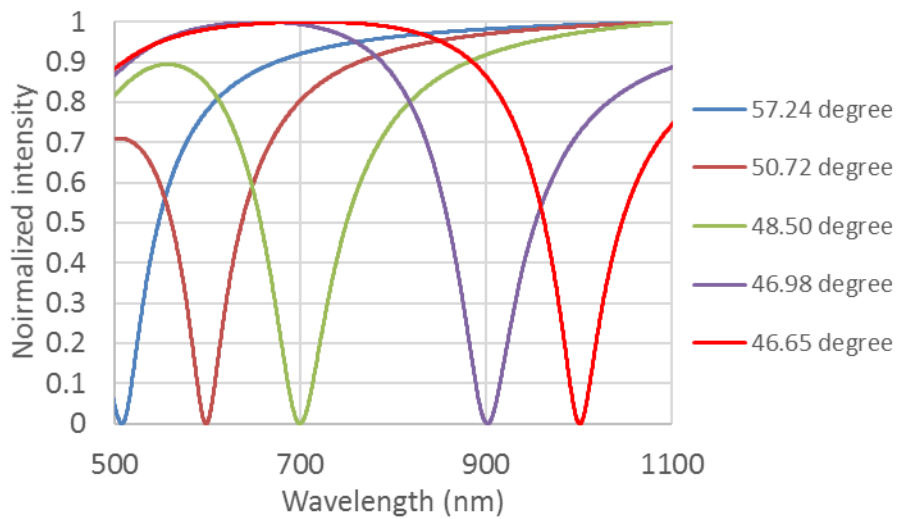


Figure 5.14 Plasmonic response shift versus incidence angle (sensed medium is air).

Concerning water, and more generally fluid medium, plasmonic response was not achievable using the combination PDMS prism – glass sensor since incidence angle is too small. To observe it, either PDMS has to be directly metalized or a substrate having same refractive index as PDMS has to be used. Then, we have modelled the water plasmon for a PDMS prism that would have been metallized directly. To get the plasmonic peak within the experimental spectrum, an incidence angle close to  $84.8^\circ$  is then requested (Figure 5.15).

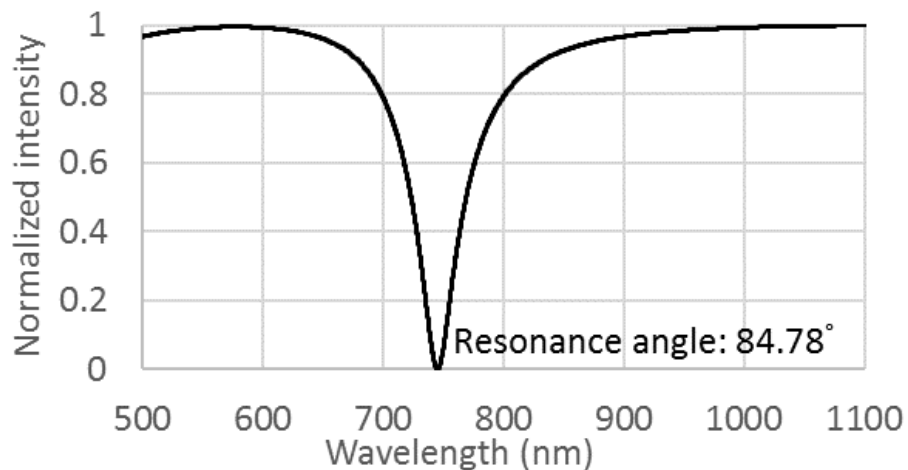


Figure 5.15 Water plasmon for PDMS prism directly metalized with plasmonic layer (incidence angle is  $84.78^\circ$ ).

The experimental implementation is shown in § 5.2.4.

### 5.2.2 Fabrication of PDMS prism

In order to be inserted with minor modifications of the optical set-up, the facet angle of the prism was designed to be  $60^\circ$ . This allows the height of the prism handling system not to be hardly modified changing glass prism to PDMS prism. A 3D printing technique was used to fabricate the prism mould. Such as, the roughness of 3D printed mould is disastrous having optical quality facets. In order achieving those - input and output facets as well as top surface - the corresponding side walls of the mould have been fitted with silicon wafer pieces.



*Figure 5.12 Mould for PDMS prism.*

In order avoiding the PDMS (preparation of PDMS is detailed in Appendix A) from sticking to the surface of silicon and easing the demoulding of the prism, 10nm of Teflon was deposited (using PECVD) on silicon pieces before their assembling with the 3D mould. So the two angled facets (input and output facets) were covered with a Teflon coated silicon piece. Likewise the larger opening (sensor surface) was also covered with a piece of silicon. The so "silicon coated" mould was put upside-down (larger opening at bottom) and the PDMS solution was poured into using the smaller opening (prism base). The PDMS filled mould is then kept inside oven at 70°C for 2 hours in order to enhance the polymerization process. After two hours the sample is removed from the oven and then the PDMS prism was removed slowly from the mould by removing the silicon piece over the large opening and pushing gently the opposite face. Views of de-moulded prism are shown in Figure 5.13.



*Figure 5.13 Fabricated PDMS prism.*

### 5.2.3 Using PDMS prism (with a glass sensor)

The fabricated PDMS prism was then fixed on the spectral interrogation setup in order to observe air plasmon. Owing to PDMS surface properties, the glass sensor was deposited

on the prism surface without any matching index liquid. The incident beam was almost horizontal ( $2^\circ$  towards horizontal plane) in order to achieve the resonance angle (around  $85^\circ$  on Figure 5.15) taking into beam deflection at air-prism interface. Figure 5.14 shows the spectral interrogation setup with the fabricated PDMS prism and glass sensor.

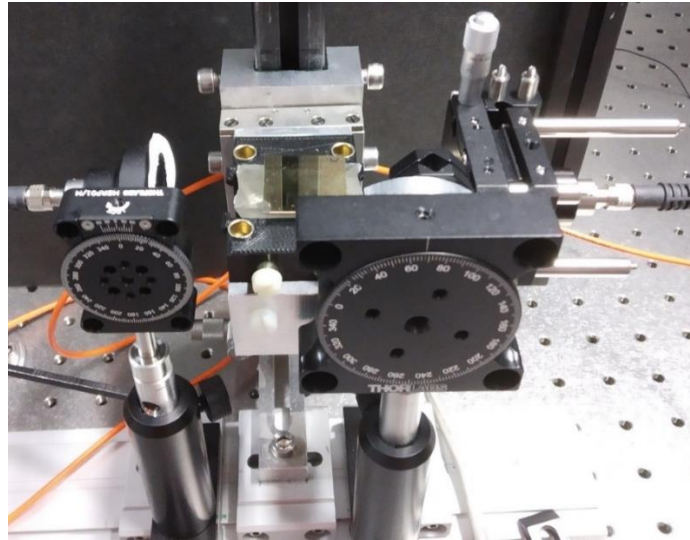


Figure 5.14 Spectral interrogation optical setup embedding the PDMS prism.

Figure 5.14 shows the observed air plasmon. The experimental response is focused on the bottom of the response peak. This explains the saturated spectrometer response in the upper band. Moreover the theoretical response spectrum does not take into account the bell-shaped response of the experimental system, a flat (without plasmon presence) response is modelled all over the band.

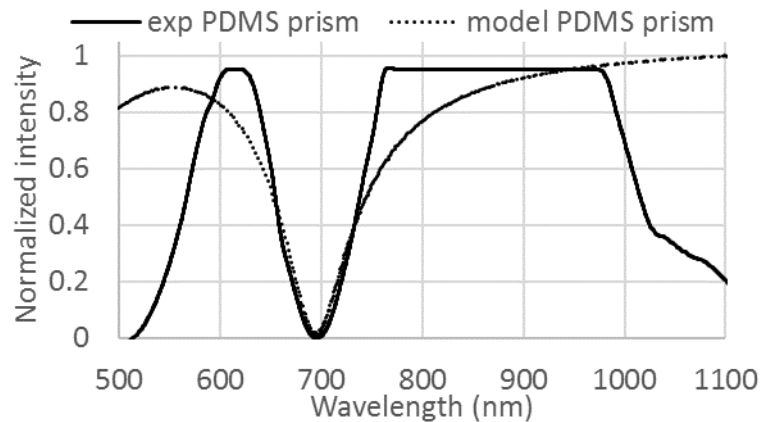


Figure 5.15 Comparison between theoretical and response curves of glass sensor on PDMS prism for air as sensed medium.

This plasmonic response using PDMS prism was compared with using a glass prism. Figure 5.16 shows the comparison of air plasmon using both prisms, either experimental or theoretical. In order plasmonic peak to be located at same wavelength, incidence angle is  $40.04^\circ$  for glass prism and  $48.25^\circ$  for PDMS prism. Good agreement is obtained correlating the bottom of the responses, larger correlation cannot really be made since theoretical curves do not take the bell-shaped form of the experimental spectrum.

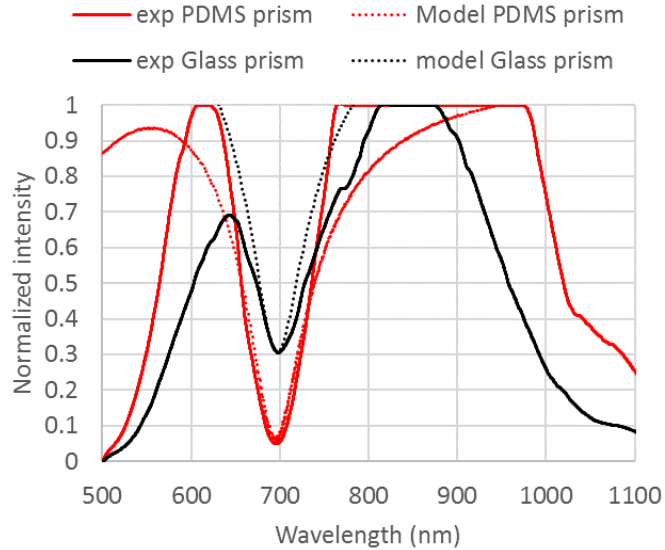


Figure 5.16 Experimental (solid lines) and theoretical (dotted lines) of air plasmonic responses using glass and PDMS prisms.

#### 5.2.4 Using PDMS prism (with a flexible sensor)

As seen in §5.2.1, water plasmon using a PDMS prism can only be observed if PDMS prism is directly metallized. Nevertheless, the prism being more than 1 cm high, it cannot be inserted within the e-beam evaporator. We decided so to use a thin (2mm) PDMS film that will be metallized (Figure 5.17). As the coupling prism is made of PDMS and owing to self-sticking properties of PDMS, it was possible to fix the PDMS sensor over the PDMS prism without any matching index liquid. In order to get to parallel surface with optical quality, the same fabrication method as for the prism was used, i.e. two silicon wafer pieces that were previously Teflon coated were placed on both sides of a 3D mould.

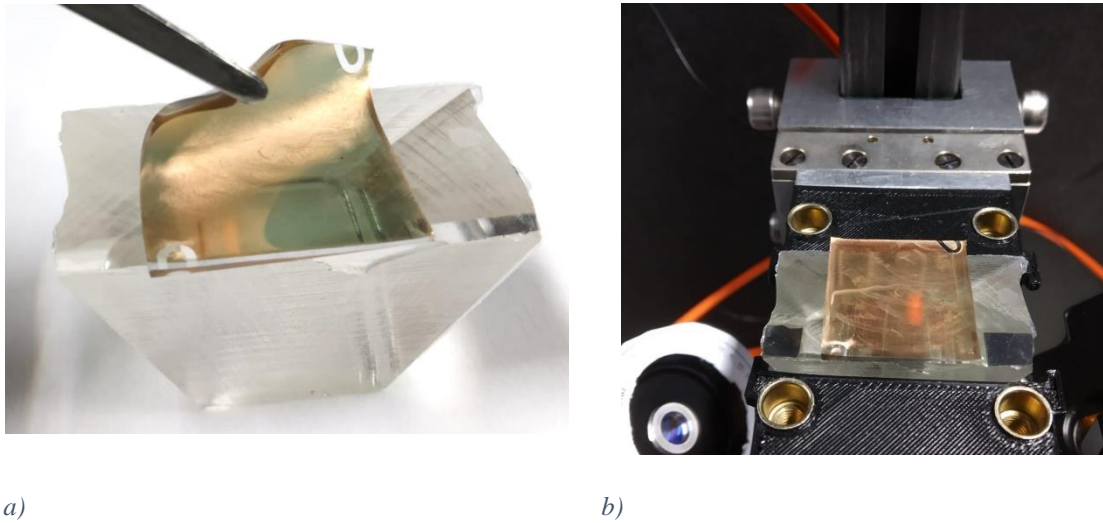


Figure 5.17 Metalized PDMS sensor that was used as a plasmonic layer on the PDMS prism: a) self-sticking on PDMS prism, b) setting-up in the spectral interrogation bench.

In such conditions, the plasmonic response obtained for air sensed medium (Figure 5.18) is rather badly defined (Figure 5.18). We do not have a clear explanation for the observed phenomenon. We can nevertheless challenge the quality of the interface between prism and sensor that we initially supposed to be seamless.

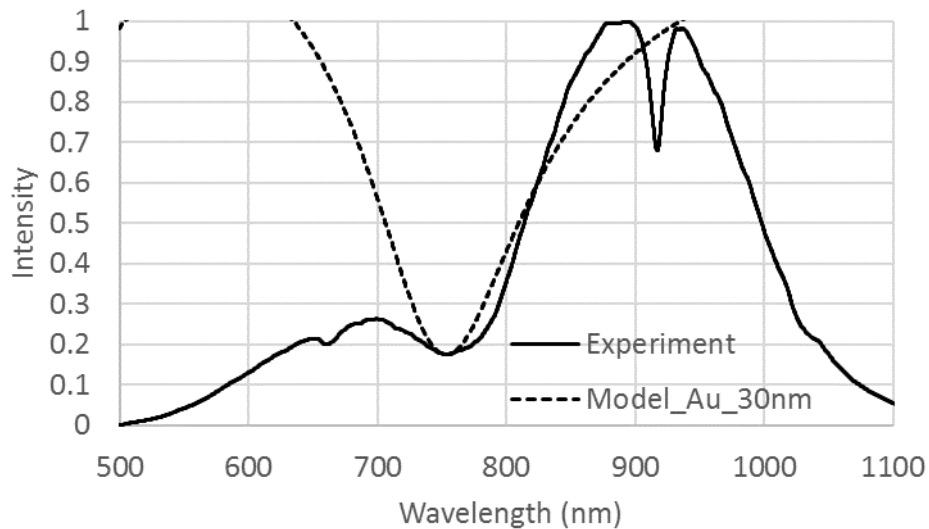


Figure 5.18 Comparison of experimental and theoretical plasmonic responses using a PDMS prism coupled to a PDMS sensor (sensed medium is air, incidence angle is  $48.17^\circ$ ).

In order trying to clear this phenomenon we decided to use the tape sensor (see § 5.1) in combination with the PDMS prism (Figure 5.19). The incidence angle was fixed at  $47.98^\circ$ .



Figure 5.19 Tape sensor on PDMS prism.

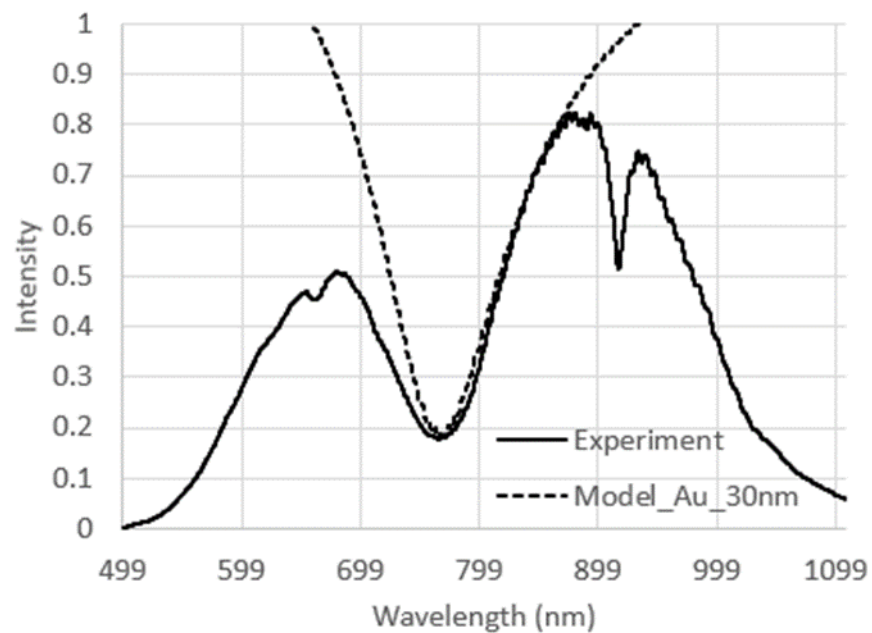
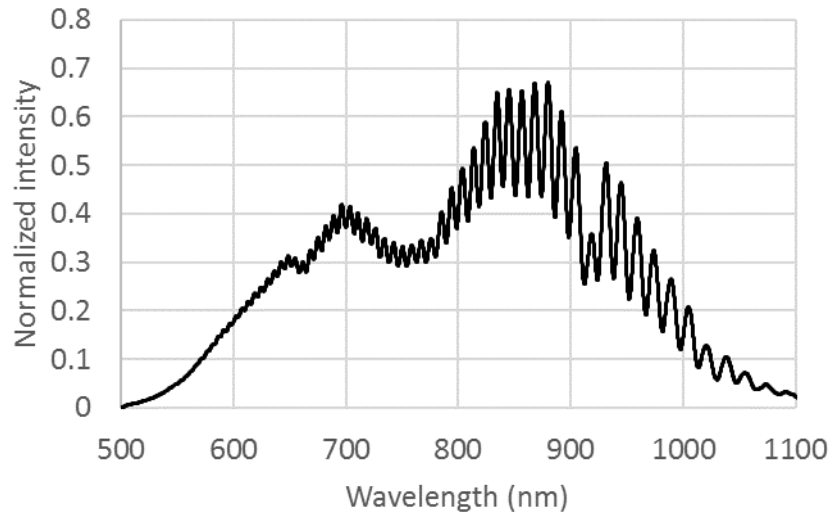


Figure 5.20 Measured air plasmon using PDMS prism and tape sensor.

Figure 5.20 shows the comparison of the measured air plasmon and modelled air plasmon with PDMS-tape configuration. A clearer response is obtained than using the PDMS sensor.

Water plasmon was also measured (Figure 5.21) but the result was not so convincing. Interferences appeared, may be due to the numerous successive use of the tape sensor that finally degrade its adherence to the prism.



*Figure 5.21 Plasmonic response of a water drop using tape sensor and PDMS prism*

### 5.3 Conclusion

We reported there the use of polymer based optical components in order decreasing the cost of elementary tests.

We first investigated a SPR sensor made on a flexible tape. We characterized it on the angular tests bench at 1550nm. Even if interferences occur due to refractive index difference between tape and glass coupling optics, sensitivity lower but in the order of that obtained with a glass sensor have been recorded.

Secondly, we investigated a coupling prism made of PDMS material. Using a glass sensor only allows to measure air as sensed medium. Using the previous tape sensor allows also air plasmon to be measured. Water plasmon even if existing was not so clearly observed. Astonishingly, a PDMS based sensor did not provide convincing results.

For those experiments, PDMS prism angle was 60°. Changing this angle might allow to ease the experiments since incidence angles, especially for refractive indexes of water or so (i.e. biological solutions), were here too large.

Tape sensors have also been fabricated using the channelled design used for temperature control (see § 4.2) (Figure 5.22).



*Figure 5.22 Flexible 4 channel tape sensor.*

## Chapter 6: BIMETALLIC SPR SENSOR FABRICATION

In this chapter, I will show the fabrication of bi-metallic SPR sensor and compare the experimental results of both Au and Ag/Au SPR sensors.

As the metal combination of Ag/Au (30 nm: 5nm) gave the better modelling results (see Chapter 2), the primary goal of fabrication process was to make such sensors.

They have been measured on both experimental set-ups and their experimental results compared to that of Au sensors.



## 6.1 Fabrication of bimetallic Ag/Au sensor:

Bimetallic sensors are fabricated the same way that classical gold sensor (see § 4.2) except the deposition step that is here shared into Ti (2 nm), Ag (30 nm) and Au (5 nm). Once the substrate was metallized, the metal thickness was checked observing a cross-section under scanning electron microscope. For that characterization we used a piece of a silicon wafer that was jointly metallized with the sensor. From the SEM image, a thickness around 45nm could be determined (but observation was not so easy) instead of 37nm that shall have been deposited. Nevertheless, it is all the more difficult to differentiate Ag and Au on SEM pictures. In order trying to determine the thickness of each layer, we tried to model the plasmonic response of water and to compare it with experimental result (Figure 6.1). Effectively, the modelled plasmonic curve for a Ag/Au (30 nm:5 nm) does not fit with the experimental curve but when the thickness of Au was slightly changed to 10nm the modelled plasmonic curve fits fine with the experimental one. The variation of the thickness of the Au film is nevertheless within the tolerance of the deposition process for such low thicknesses.

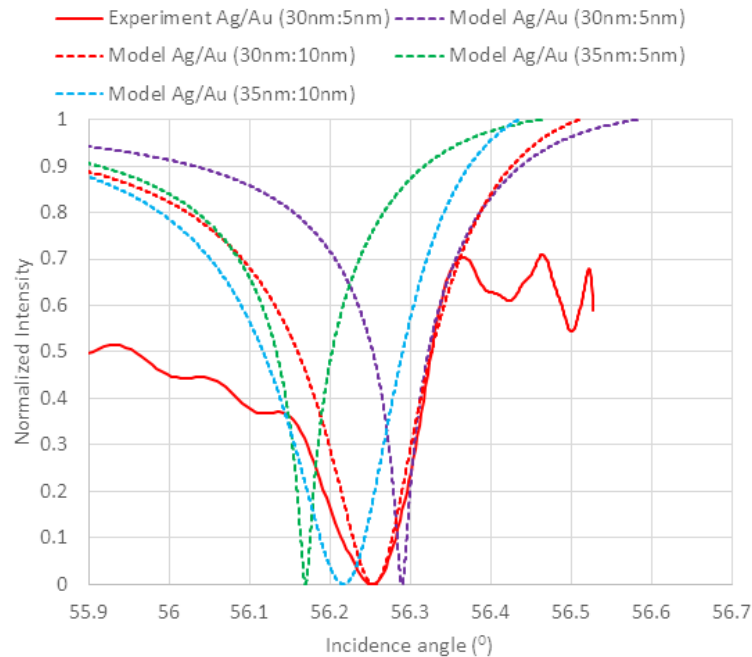


Figure 6.1 Comparison of theoretical and experimental bi-metallic plasmonic responses of water.

The best fit is obtained for a thickness of 30 nm and 10 nm for Ag and Au, respectively. These values will be used for further modelling.

This sensor has been declined into a 4-channel sensor (Figure 6.2)



Figure 6.2 4 channel Ag/Au sensor (here with fluidic facilities).

## 6.2 Experiments on angular bench at 1550nm

### 6.2.1 Calibration

For the calibration, same protocol using ethylene-glycol solutions as for classical Au sensor has been used (see Chapter 3). The sensorgram that is then obtained is represented in Figure 6.3.

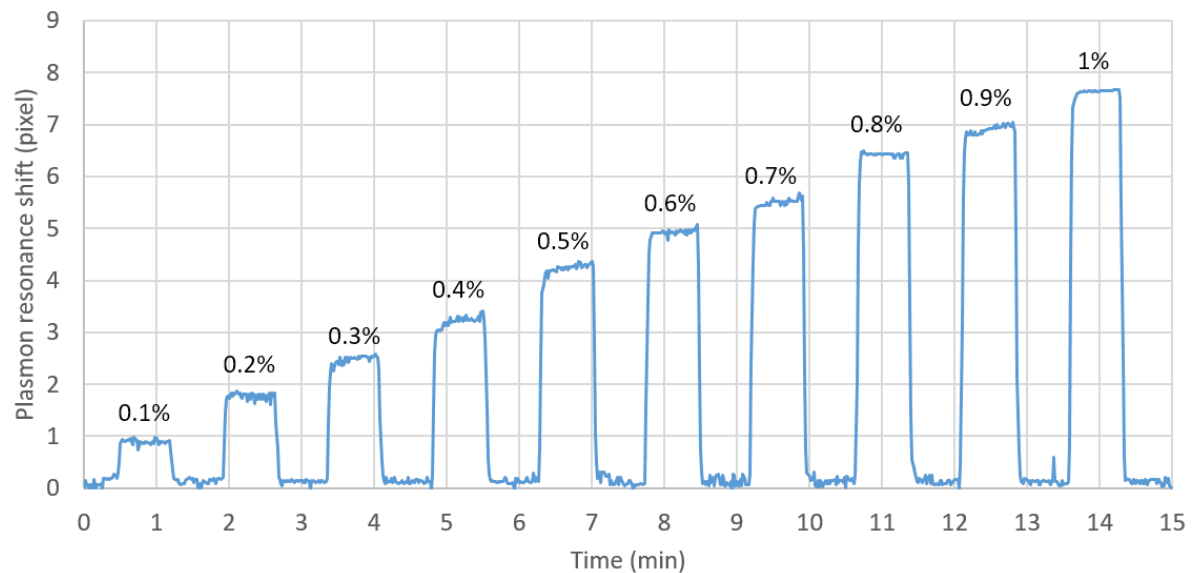


Figure 6.3 Measured sensorgram for different concentrations of ethylene glycol solutions in water.

Sensitivity has been calculated and compared to the theoretical prediction using a Ag/Au (30 nm:10 nm) sensor (Figure 6.4). Sensitivity value of 68.43° has been achieved that is in good agreement with theory.

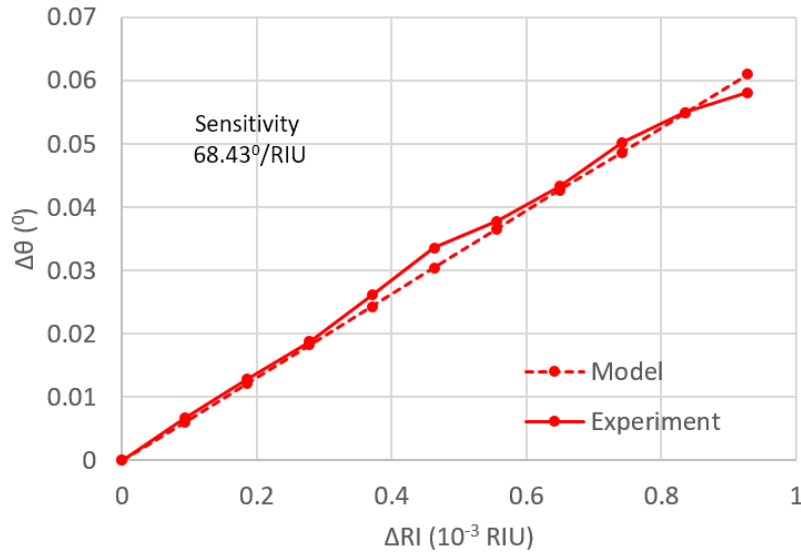


Figure 6.4 Sensitivity of Ag/Au (30 nm:10nm) sensor.

### 6.2.2 Comparison between gold and bi-metallic sensor

The experimental plasmonic responses for sensors using classical Au and bi-metallic Ag/Au layer were compared with each other (Figure 6.5a) and with theoretical predictions (Figure 6.5b). The theoretical results have been made using the layer thicknesses that maximize the fitting between experiment and theory. The discrepancy that appears is linked to fabrication tolerance.

The sensitivity of both sensors has been evaluated (Figure 6.6). From this comparison, both sensors exhibit almost the same sensitivity value, 68.43°/RIU and 65.05°/RIU for Ag/Au and Au sensor, respectively. There is not a so high difference between both sensitivity values but, as mentioned in § 2.3.5, the penetration depth of silver based layers is higher when compared to gold layers. Anyway, for the detection of molecular interactions that are

located at the close interface level, achieving a higher penetration depth might not reflect an increase of sensitivity, and may be, may induce the reverse effect.

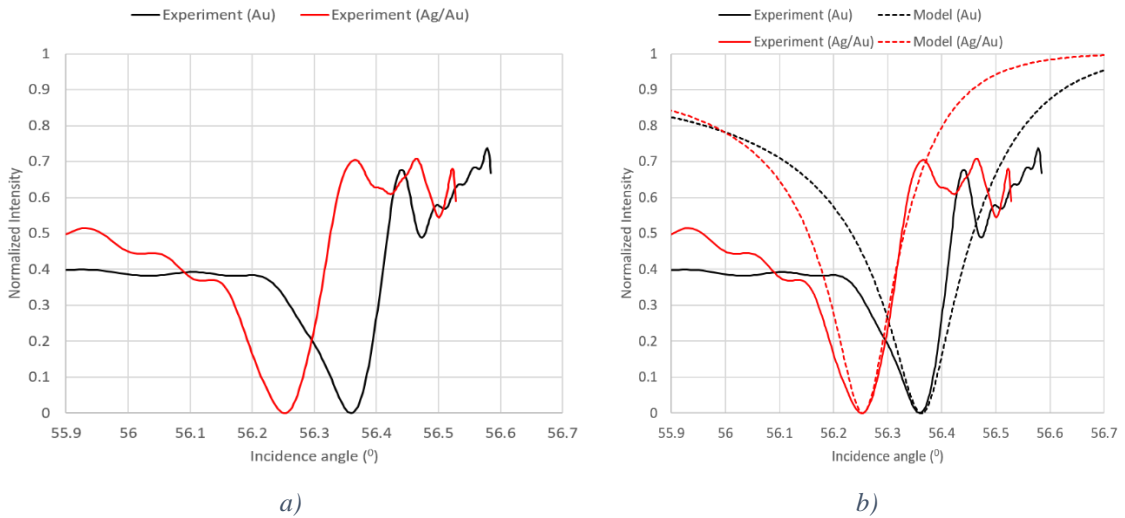


Figure 6.5 Plasmonic responses of Au and bi-metallic Ag/Au sensor for water a) experimental results, b) comparison of experimental and modelling results (experimental results mention the desired film thickness, theoretical results mention the thickness that match the observed experimental results).

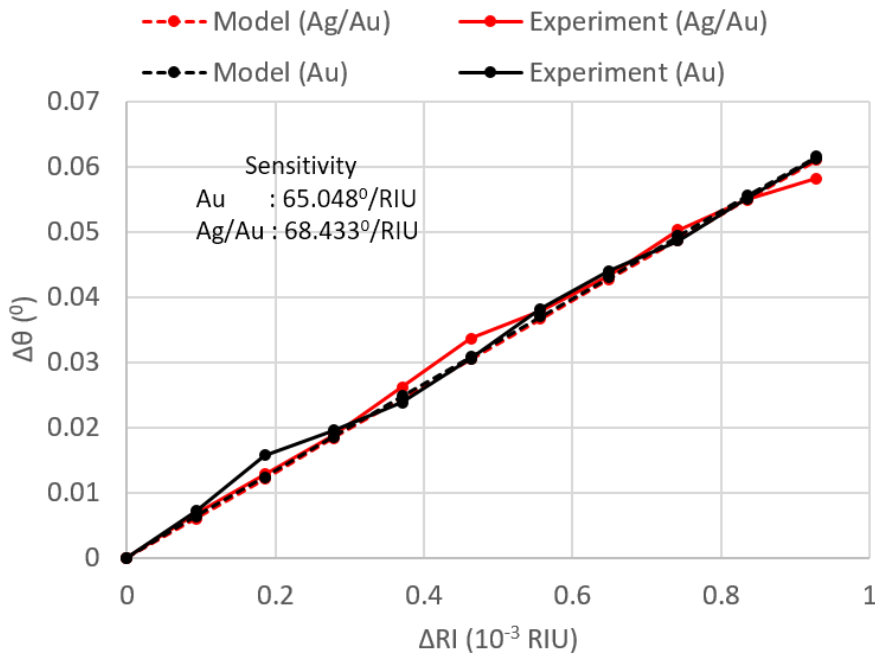


Figure 6.6 Deduced experimental sensitivity value for Au and Ag/Au sensors (theoretical evolutions are also reported for comparison).

From the baseline of a sensorgram (Figure 6.7b), the standard deviation can be evaluated at 0.037 to be compared to 0.028 (Figure 6.7a) obtained for Au sensor. Taking the same

assumption that in § 3.1.2, i.e. that the minimum detectable signal is that providing a signal at least twice the amplitude of the noise level, the minimum detectable signal will be  $1.13 \times 10^{-5}$  RIU ( $8.60 \times 10^{-6}$  RIU was obtained for Au sensor).

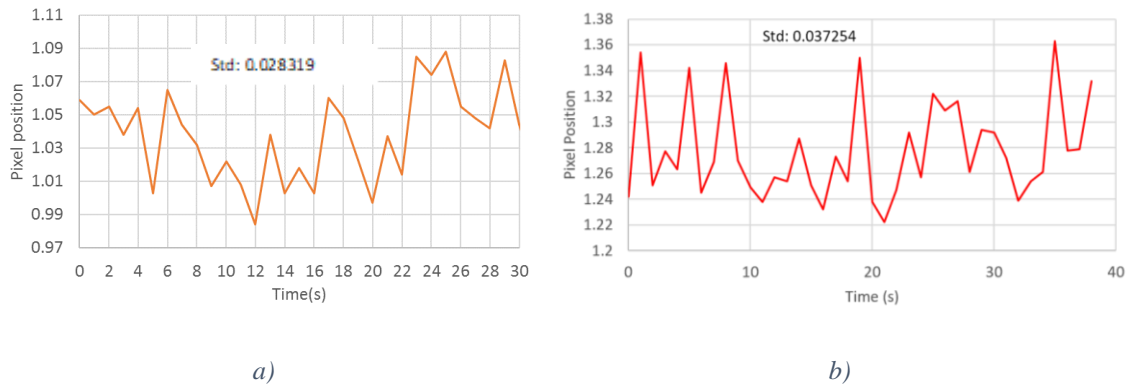


Figure 6.7 Fluctuations of detection baseline for a) Au and b) Ag/Au sensors.

## 6.3 Experiments on spectral bench in the visible range

### 6.3.1 Calibration

Same calibration protocol as above mentioned was made on the spectral interrogation bench. The sensitivity was calculated the same way as in Chapter 3 (Figure 6.8). An experimental sensitivity of 2108.6 nm/RIU was calculated to be compared to 2041.7 nm/RIU that is obtained by modelling. Here too a good agreement is obtained between both results.

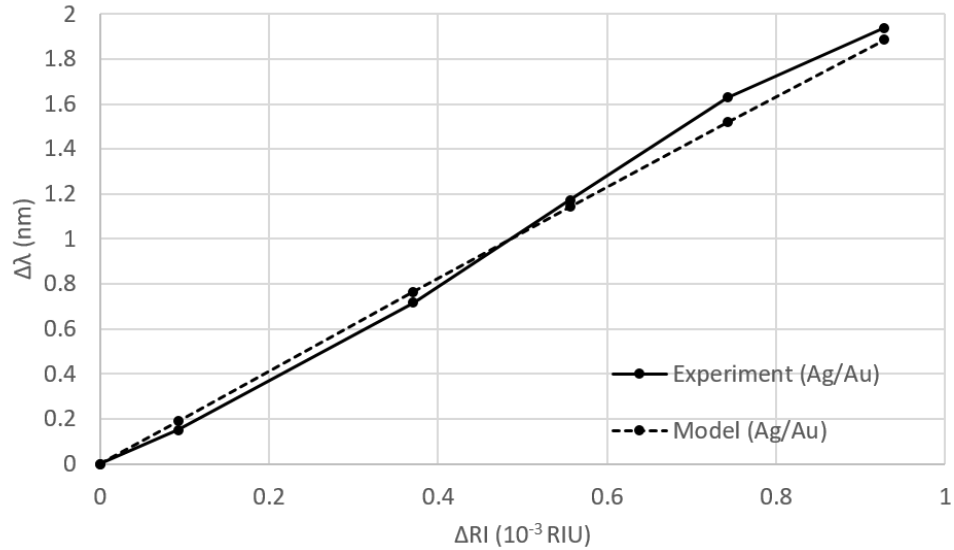


Figure 6.8 Experimental sensitivity comparison with modelling.

### 6.3.2 Comparison between gold and bi-metallic sensor

The sensitivity of both sensors has been compared (Figure 6.9). From this comparison, both sensors exhibit also almost the same sensitivity value as previously obtained using angular interrogation scheme (see § 6.2). Sensitivity values of 2108.6 nm/RIU and 1965.5 nm/RIU for Ag/Au and Au sensor, respectively.

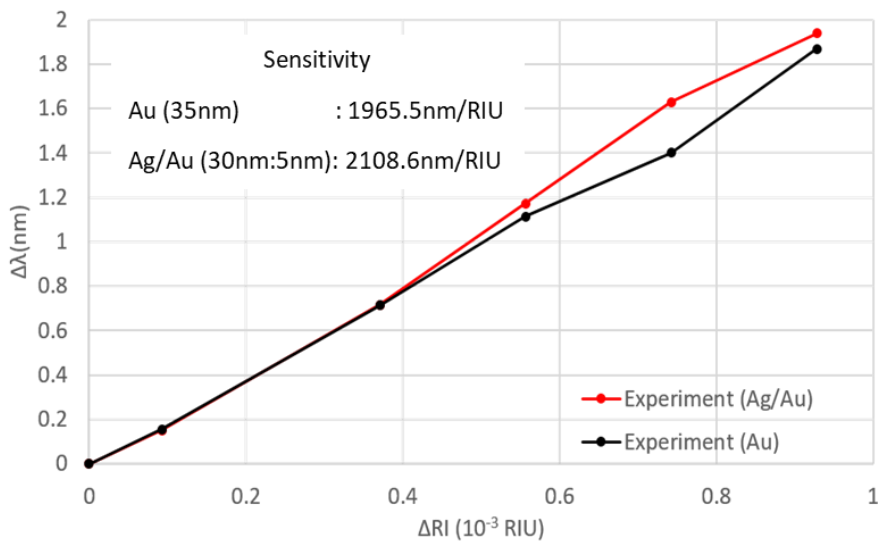


Figure 6.9 Deduced experimental sensitivity value for Au and Ag/Au sensors.

Identically to the angular interrogation set-up, noise level has been evaluated from the baseline of a sensorgram (Figure 6.10b), the standard deviation can be evaluated at 0.054 to be compared to 0.024 (Figure 6.10a) obtained for Au sensor. Taking the same assumption that in § 3.1.2, i.e. that the minimum detectable signal is that providing a signal at least twice the amplitude of the noise level, the minimum detectable signal will be  $5.5 \times 10^{-5}$  RIU against  $2.4 \times 10^{-5}$  RIU for Au sensor.

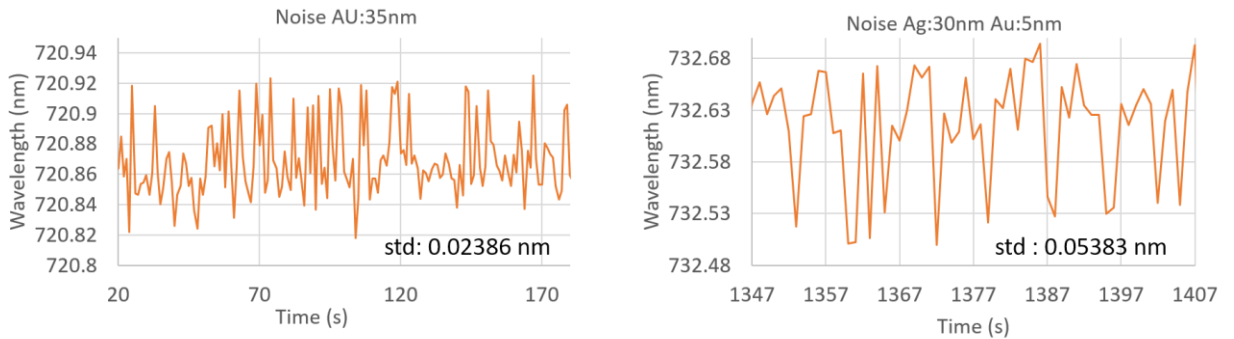


Figure 6.10 experimental noise level comparison for both Au and bimetallic sensor.

## 6.4 Conclusion:

Experiments using bi-metallic silver/gold sensors were performed on both the interrogation optical setups and the results were compared with the modelling. No particularly noticeable difference on the sensitivity of the SPR system, whatever it is, including either a bimetallic or an Au sensor has been recorded. As seen in chapter using silver as a plasmonic layer might improve the penetration depth of the plasmonic wave into the sensed dielectric medium but this can result in an opposite effect on the sensitivity in biomolecular interaction monitoring. Effectively, the bulk optical refractive index will then have a higher impact on measurement since biomolecular events are located at the very close distance from interface due to surface functionalization (nevertheless, this also depends on the size of the molecules to be detected).



## CONCLUSION AND PERSPECTIVES

### Conclusion

As mentioned in Chapter 1, the aim of this thesis work was to develop a SPR bio-sensing system approach ultimately dedicated to be part of a portable detection system. Keeping this in mind, I have first worked on the modelling of plasmonic response in the angular interrogation scheme working at 1550nm wavelength and tuned the various parameters which can improve the performance of the system and came up with the simulation results as shown in the Table C.1.

Modelling			
Angular interrogation scheme (1550nm)			
Sensor type	FWHM (°)	Sensitivity (°/RIU)	FOM (RIU <sup>-1</sup> )
Au	0.093	66.4	714.0
Ag/Au	0.077	65.6	846.3
Tape	0.046	53.4	1148.0

Table C.1 Modelling results on various performance characteristics with three different types of sensors.

From the Table C.1, it can be seen that the FOM value which was calculated using the plasmonic curve FWHM and the sensitivity that has been calculated using refractive indexes that can be replicated in the experimental part (ethylene-glycol solutions).

Experimental			
Angular interrogation scheme (1550nm)			
Sensor type	FWHM (°)	Sensitivity (°/RIU)	FOM (RIU <sup>-1</sup> )
Au	0.097	65.0	669.9
Ag/Au	0.101	66.4	653.8
Tape	0.053	53.5	1006.4

Table C.2 Experimental results that were determined using the three different plasmonic sensors.

The calculations of FWHM and FOM for modelling and the experiments were made in the same way in order both the results could be compared. Further all the three types of sensors were fabricated, and experiments were performed on an angular interrogation bench working at 1550 nm. The corresponding results are shown in the Table C.2. As already obtained in the modelling section, the FOM value was higher for the tape sensor when compared to the other two types of sensors (Au and Ag/Au). Fabrication of the SPR tape sensor was a novel advancement in the field of SPR biosensors. As this is a flexible use and throw sensor that can be used directly on the coupling optics without any need of additional requirements like matching index oil. This sensor could also reduce the cost of the system. The "classical" sensor type, using either Au or Ag/Au plasmonic layer exhibited almost same characteristics. It has nevertheless to be noted that the performance of Ag/Au sensor is highly depending on its composition (modelling results) and that reproducing it at experimental level requires high process control. Calculating FWHM on experimental curves is also somehow tricky since white level is often biased by experimental conditions.

I developed then a spectral interrogation scheme set-up since this kind of interrogation scheme was more particularly envisaged for the design of the portable equipment. I calculated the plasmonic responses like previously for the angular interrogation scheme (Table C.3).

<b>Modelling</b>			
Spectral interrogation (500-1100nm)			
Sensor type	FWHM (nm)	Sensitivity (nm/RIU)	FOM (RIU <sup>-1</sup> )
Au	53	1987.5	37.5
Ag/Au	43	2041.7	47.5

*Table C.3 Calculated performance characteristics of two different plasmonic sensors.*

Here the modelling results show that the FOM for bimetallic Ag/Au is higher than that of Au sensor. I developed the spectral interrogation optical setup which is 3 times smaller than the angular interrogation setup as this was to be converted into a portable system. The

system was built and validated by performing various experiments as will be discussed further. Table C.4 shows the measured performance of those sensors in the spectral interrogation system.

<b>Experimental</b>			
Spectral interrogation (500-1100nm)			
Sensor type	FWHM (nm)	Sensitivity (nm/RIU)	FOM (RIU <sup>-1</sup> )
Au	53.4	1965.5	36.8
Ag/Au	46	2108.6	45.8

*Table C.4 Experimental using the two different plasmonic sensors (Au and Ag/Au).*

As can be seen the experimental results are almost in agreement with the calculation that were performed before.

All those results allow to compare sensors on a specific bench, comparison of performance between different interrogation schemes is not really significant since data are completely different. Concerning the plasmonic layer type, we saw that its composition does not greatly impact the performance in the near-IR domain that is not the case in the visible domain.

As a portable SPR system will developed for the detection of pathogens, one of the main problems that could affect the systems sensitivity is temperature. This is the reason some of the commercially available SPR bio-sensing systems are facilitated with a temperature control. And due to this temperature control system, the system becomes bulky and its implementation in a portable system almost unrealistic. So, I investigated the use of Joule's heating using the plasmonic layer as heater. The sensor is then declined as a 4-channel sensor in order to control the temperature independently. COMSOL modelling has been used to predict behaviour, thermal IR imaging to validate the results experimentally. Good agreement has been obtained comparing those results. Experimental heating of a drop of water showed that refractive index of hot water could be measured and positively compared to theoretical values up to temperature rises of around 30°C. This temperature range should be sufficient for the follow-up of most of biomolecular events. For particular ones, such as

DNA strands de-hybridization, that should require higher temperature rises some discrepancy is observed. This has been confirmed using an integrated Pt sensor as temperature monitor. Due to the bell-shaped temperature profile across a channel that is more and more pronounced as temperature rises, the mean value that seems more probably to be measured by the Pt sensor as well as the SPR measurement is less and less close to the maximum temperature (at mid channel) that was taken previously to compare results. Taken such a mean value improve the agreement between modelled and measured temperatures. It was also shown that for practical cases of biomolecular interactions, i.e. for temperature rises of some tens of degrees, the 4-channel design we used allows independent control of temperature on the different channels. An improved design of this 4-channel sensor integrating temperature monitoring on each channel has been fabricated. The use of USB-type electrical connectivity allows to insert the sensor into the spectral interrogation set-up while connecting all heaters and temperature sensors (Figure C.1).

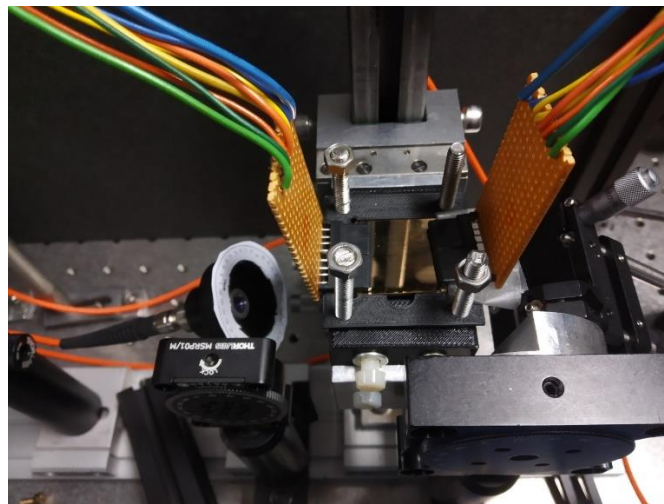


*Figure C.1 Spectral bench with 4-channel sensor integrating with temperature sensors inserted*

The use of polymer optics has also been investigated. A tape sensor allows reaching a sensitivity close to that of a glass sensor. Its use does not require refractive index matching fluid and simplifies the use on the field. A polymer prism has also been tested that could lower the overall cost of the coupling system.

## Perspectives

The spectral bench has been integrated by the MULTITEL partner of the BIOSENS project. An overall view is shown in Figure P.1, a descriptive view in Figure P.2. MULTITEL included a proprietary 4-channel spectrometer allowing 4 simultaneous measurements. Sensor type is the 4-channel sensor described in this work.



Figure P.1 Portable SPR system developed by project partner MULTITEL.

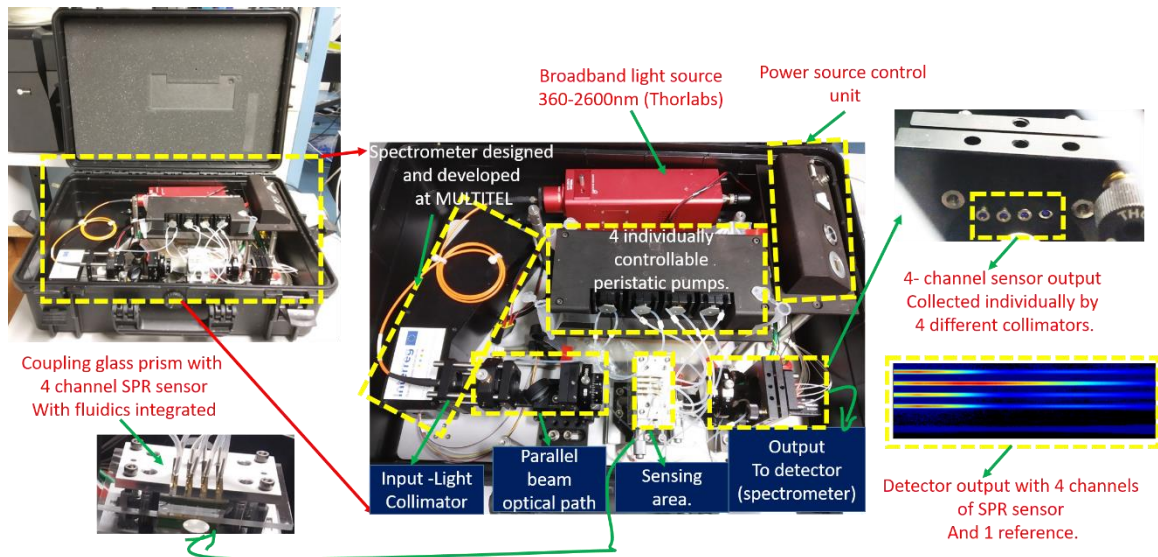
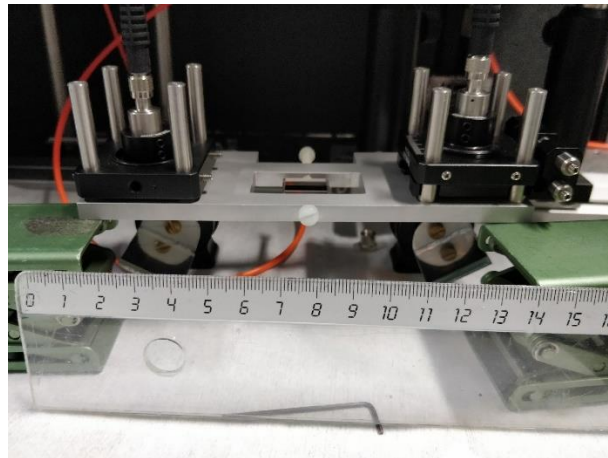


Figure P.2 Portable SPR detection equipment including a 4-channel spectrometer.

Up to now, the temperature control and monitoring have not been inserted, this can be a perspective for the improvement of measurement capabilities of this system. The portable system is currently used within the BIOSENS project for pathogens detection, i.e. *Zymoseptoria Tritici* in the agricultural domain and *Candida Albicans* in the medical domain [129].

A tentative for integrating even higher the SPR sensing head has been made (Figure P.3). Optical input and output are out of plane and micro-mirrors are used to direct respective optical beams that are now vertical. The coupling place has been kept enough free around to insert the sensor with temperature control facilities. Halogen lamp is planned to be replaced by a broadband LED source. Unfortunately, this system could not have been tested during the PhD for lack of time.



*Figure P.3 Integrated SPR sensing head prototype.*

The fluidic integration is also a primary concern of system integration. It has been handled by an other student of the BIOSENS project [129].

Polymer optics shows encouraging preliminary results. It could reduce the price of the portable system and of tests as well as it is easy to use. The fabricated PDMS prism and the results obtained using different sensors coupled on the PDMS prism are shown in Figure P.4.

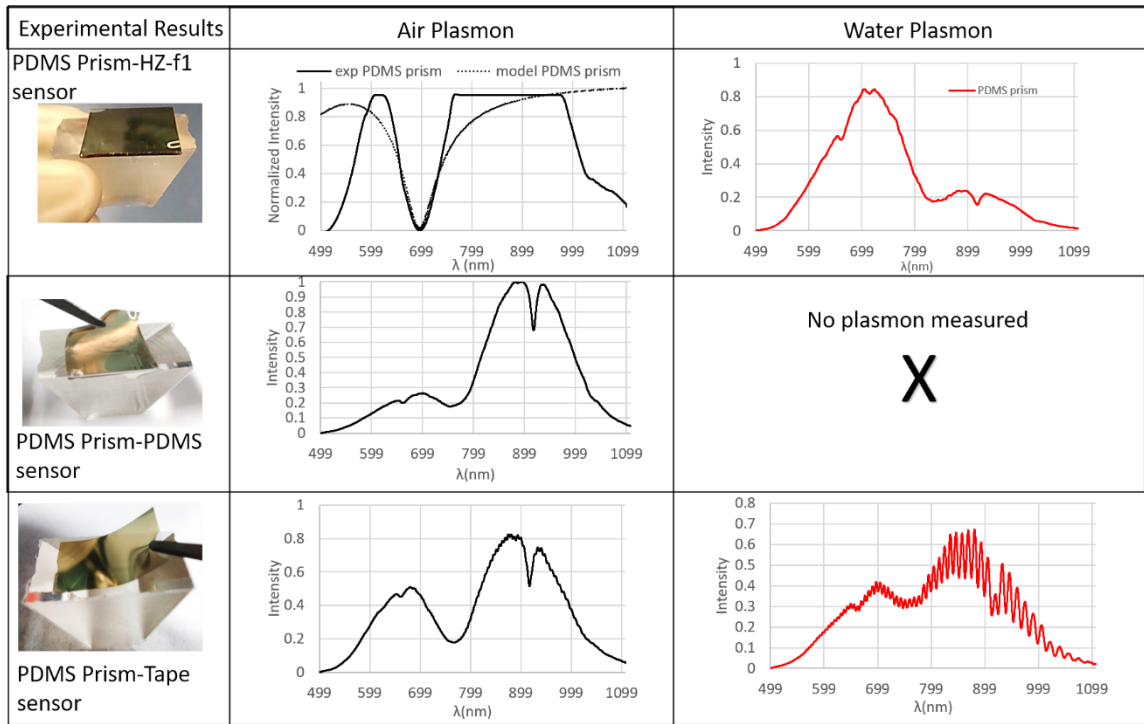


Figure P.4 PDMS prism and results obtained for water and air by coupling different plasmonic sensors.

The use of higher refractive index polymer materials has to be investigated in order to validate the use for fluids. Up to now, results for air medium are only conclusive that limit the applicability of such an approach.



## APPENDICES



## Appendix A: Fabrication of PDMS microfluidics

PDMS based microfluidics have been used under the form of a 4-channel cover that is physically (on glass using Corona effect) or chemically (on Au surface) [128] bonded to the sensor surface. The channel width is 1.5mm and 1 cm long. Two larger circular areas are provided at each end; they are located at injection places.

To fabricate the PDMS covers a mould using SU8 photo resist is firstly fabricated. This mould was fabricated on a 3" silicon (Si) wafer. We were interested to have fluidics channel depth around 250  $\mu\text{m}$  and so equivalent SU8 resist thickness. First the Si wafer was cleaned using 10% hydro fluoric acid to remove oxides from the surface. After cleaning the wafer was dried using nitrogen and set on hotplate for dehydration. Si wafer is then spin coated with a SU8-2075 resist. The parameters used for the spin coating are as follows: speed of 500rpm, acceleration of 100rpm/s for 3s keeping the cover of the spin coater open and in a second stage speed of 2500rpm, acceleration of 100rpm/s for 15s. By utilizing those two stages for spin coating we ensure that the resist slowly covers all the area of the wafer homogeneously. For post-bake process, we used two hotplates at different temperatures (65°C and 95°C) in order that SU8 photoresists does not show cracks. First step is using a hot plate at 65°C in contact for 3minutes. Second, the sample is transferred to the hot plate at 95°C for 8 minutes, in contact. After hot plate removal, the sample is placed at room temperature for 15 minutes to cool down so that the resist relaxes. Laser lithography is used for patterning. The laser power was 100% at 50mm/s speed and a 10  $\mu\text{m}$  spot was used since no high precision is here requested. Post-bake during 15min at 95°C is done before development. We used two beakers filled with SU8 and developed in one beaker for 15 minutes and continued to develop using the second beaker for other 15 minutes. By doing this we can be sure that the removed resist goes away from the substrate without being re-deposited on it. After those 30 minutes of development the sample was cleaned using isopropanol solution for 30s and then dried using nitrogen. Once dried, the sample is placed inside a temperature controllable heater and again post baked. A thermal ramp process is used: it was set to increase by 10°C/min from room temperature up to of 75°C, to maintain 75°C for 2 hours and then the cool down is made using the reverse temperature ramp. After this SU8 hardening process, the SU8 mould is coated with a thin layer of Teflon using

plasma deposition. The recipe to deposit Teflon uses  $\text{CHF}_3$  plasma at 180W and 150mT for 1 minute to get 50nm-thick Teflon film on the surface of the SU8 mould. Teflon is deposited in order to protect PDMS from sticking to the surface of the SI wafer.

The fabricated SU8 mould for PDMS fluidics is shown in Figure A:1.

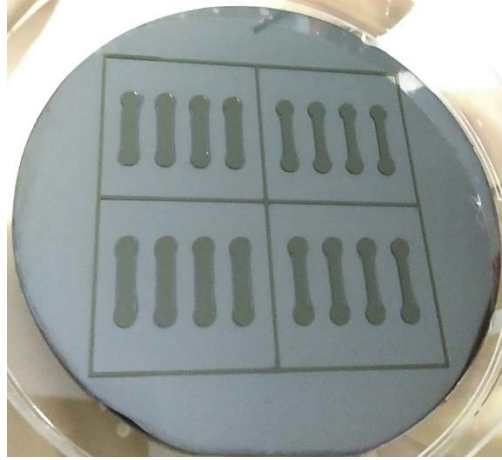


*Figure A: 1 Fabricated SU8 mould.*

The SU8 mould is set into a plastic Petri dish using a double-sided scotch tape. This is fixed strongly so that the SU8 mould does not move during the PDMS preparation. To prepare the PDMS solution we weight 30gram of polymer (silicon elastomer) in a beaker and add 3g of silicon elastomer curing agent. This solution is then stirred vigorously till it shows up with lot of bubbles. It is then inserted into a vacuum chamber for degassing for 30 minutes. During the degassing process, bubbles disappear, and the solution become transparent. PDMS solution is then removed from degassing chamber and slowly poured into the Petri dish containing the SU8 mould. A film thickness of about 3mm is made. A bake at  $70^{\circ}\text{C}$  for 2 hours is made in order to enhance the polymerization process. After removal from the oven, the PDMS layer is peeled off slowly from the mould.

To fix the PDMS on the sensor surface, two techniques were used depending if sensor surface was 4-channel patterned or fully Au covered. In the first case, both PDMS and glass were treated using a Corona plasma and then pressed together for 1 minute. Then the bonding is ensured by placing in the oven for 1 hour at  $70^{\circ}\text{C}$ . In the second case, Au and PDMS surfaces are chemically treated instead of using Corona plasma [128].

## Appendix B: On the particular use of Al<sub>2</sub>O<sub>3</sub> layer

As Al<sub>2</sub>O<sub>3</sub> film is deposited full surface on the plasmonic layer before its etching, we did an experiment using such a "bi-layer". SPR sensor was so composed by a 35nm-thick Au plasmonic layer and a 40nm-thick Al<sub>2</sub>O<sub>3</sub> film on top. It was placed on the spectral interrogation setup and a drop of water was deposited on part of the beam line. So, one part of the output signal was corresponding to the plasmonic response of water and the other one to that of air. Using an incidence angle of 60.1°, two plasmons were observed in the same spectral bandwidth, corresponding respectively to the refractive index of water and air (Figure B:1). Despite the huge difference in refractive index, and owing to the degraded sensitivity value of the sensor due to the Al<sub>2</sub>O<sub>3</sub> film, both responses can be simultaneously recorded.

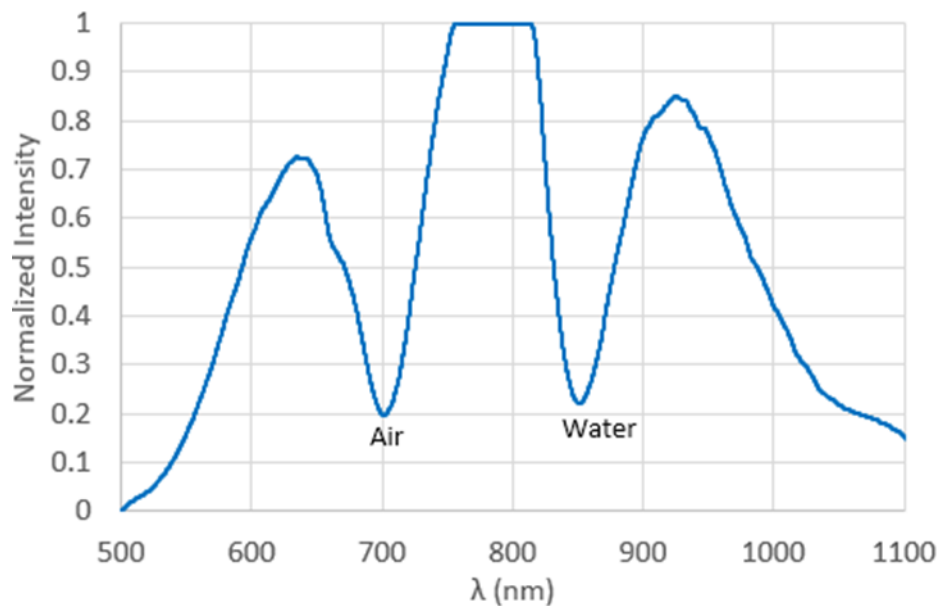
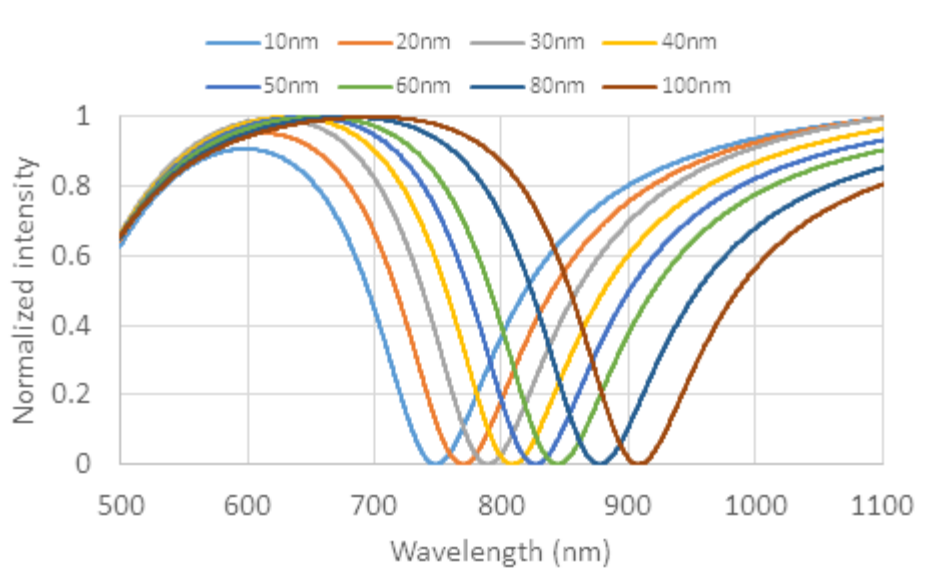


Figure B:1 Experimentally measured air and water plasmons at the same time.

The Al<sub>2</sub>O<sub>3</sub> film impacts greatly the penetration depth of the plasmonic wave into the dielectric medium and reduces so the sensitivity of the system to its refractive index. Although the practical use can be extremely limited, it allows to determine the rough refractive index of a completely unknown solution.

So further modelling was performed to analyse the plasmonic properties due to Al<sub>2</sub>O<sub>3</sub> as a sensing layer on SPR sensor.

The first modelling were performed in the spectral interrogation scheme where the incidence angle was varied according to the plasmonic layer thickness in order the plasmonic curve falls at 750nm wavelength spectrum. The first plasmonic layer was fixed to 35nm Au and the thickness of  $Al_2O_3$  was varied from 10nm to 50nm and the plasmonic response were compared as shown in Figure B: 2.



*Figure B: 2 Calculated plasmonic response for water using the sandwich resonance layers Au/ $Al_2O_3$  (35nm:varying).*

From the Figure B:2 it can be noticed that by changing the thickness of  $Al_2O_3$  above the plasmonic layer, the plasmonic peak shifts towards higher wavelengths; that is fully understandable since plasmonic wave is more and more propagating within  $Al_2O_3$  medium and less and less in sensed medium due to its limited penetration length.

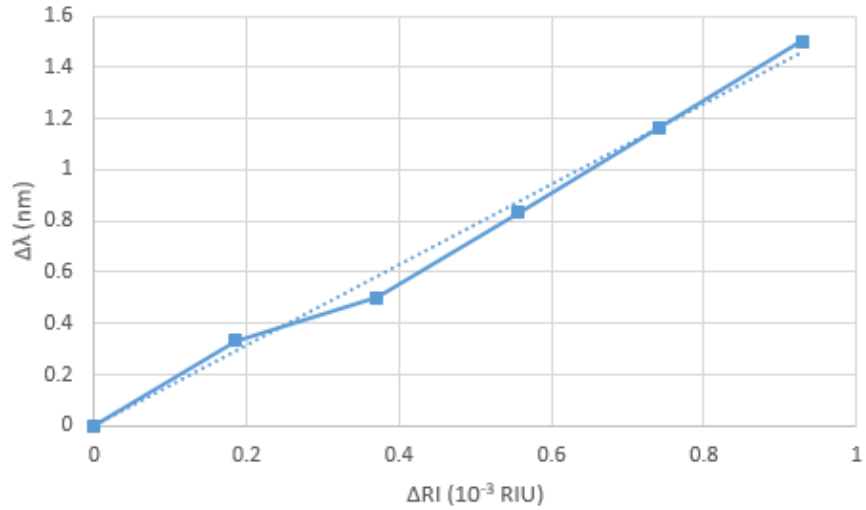


*Figure B: 3 Calculated sensitivity for Au/Al<sub>2</sub>O<sub>3</sub> (35nm:40nm) sandwich sensor.*

The sensitivity of the Au/Al<sub>2</sub>O<sub>3</sub> (35nm:40nm) were modelled and shown in Figure B: 3. For this calculation we have used different refractive index of ethylene glycol (as made for the system calibration (see Chapter 3)). The calculated sensitivity is 1568.8nm/RIU which is roughly a quarter less than using just Au as plasmonic layer.



## Appendix C: On the response curves for high temperature

As mentioned in Chapter 4, section 4.6, in order obtaining a better fit between experimental and theoretical sensitivity values upon temperature, an algebraic mean value has been calculated. Obviously, it must not be the right way to obtain the real thermal behaviour.

Looking more deeply in the plasmonic responses of a water drop versus temperature (Figure C:1) and comparing them with theoretical predictions (made for maximum temperature that is recorded over the channel cross-section), it can be noticed:

- good agreement for low temperatures, i.e. up to some 30°C (so 10°C temperature rises),
- FWHM broadening for higher temperatures and increasing discrepancy in the plasmonic peak position.

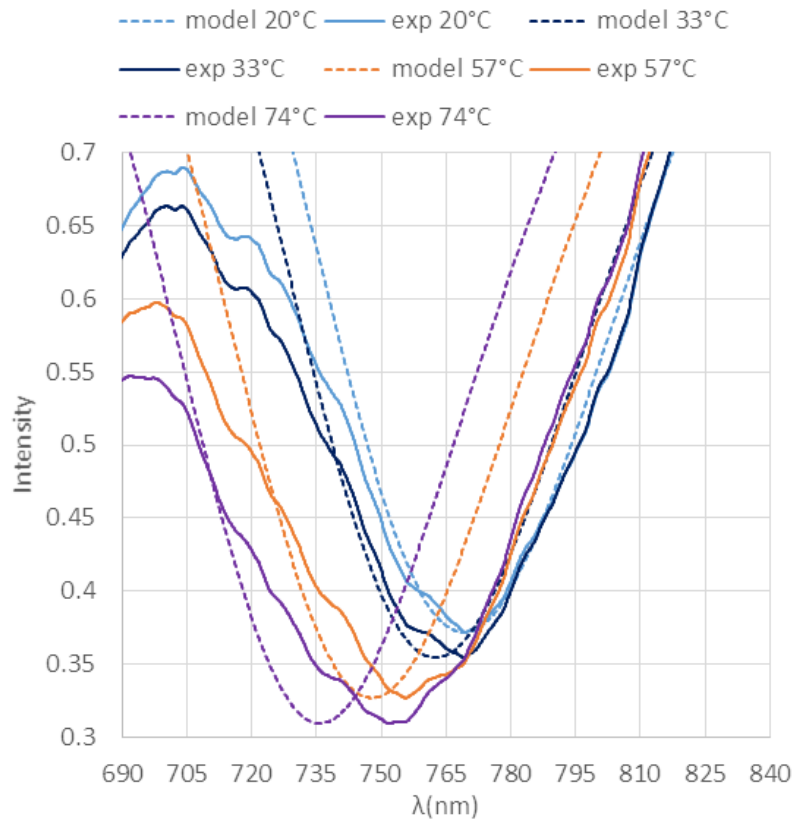


Figure C:1 Experimental (—) and theoretical (---) plasmonic responses of a water drop versus temperature.

The experimental plasmon shift is lower when compared to the modelled one. That effectively supports the assumption taken in § 4.6 where a mean, so lower, temperature value was set for the sensed medium. We try to match experimental and theoretical

plasmonic shifts by fitting the experimental curves with theoretical ones calculated at different temperatures (Figure C:2).

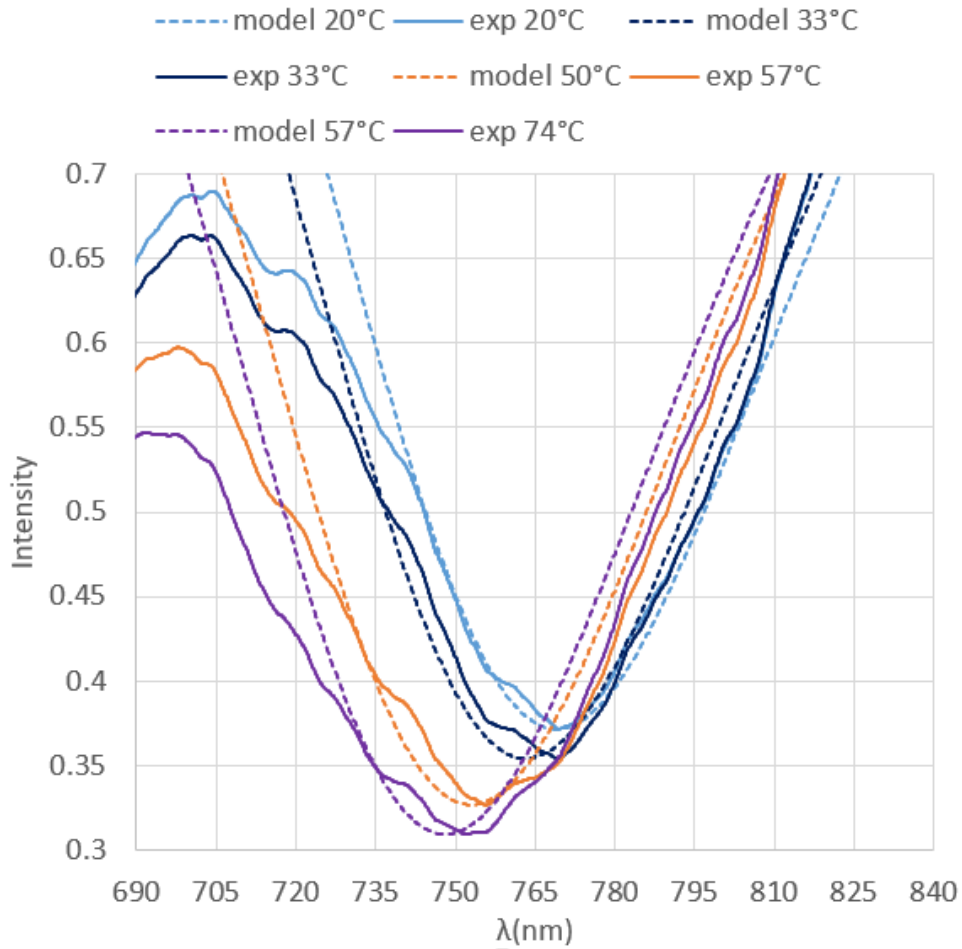


Figure C:2 Matching experimental plasmonic responses with modelling ones by adjusting the simulated temperature.

Same conclusions than drawn in § 4.6 and same range of temperature differences that shown in Table 4.2 arise. If those values are injected in the modelling, a better fitting with the experimental curve is obtained (Figure C:3).

However, this does not reproduce the broadening of the experimental response curve. It has been reported that the change of the relative electric permittivity of gold with the temperature also affects the resolution of the SPR measurements [81]. The modelling should so be revised in order to include it. We also seen (Figure 4.22) that temperature that is sensed all across the channel is not homogeneous. Broadening can also be due to the superposition of several response curves at different temperatures.

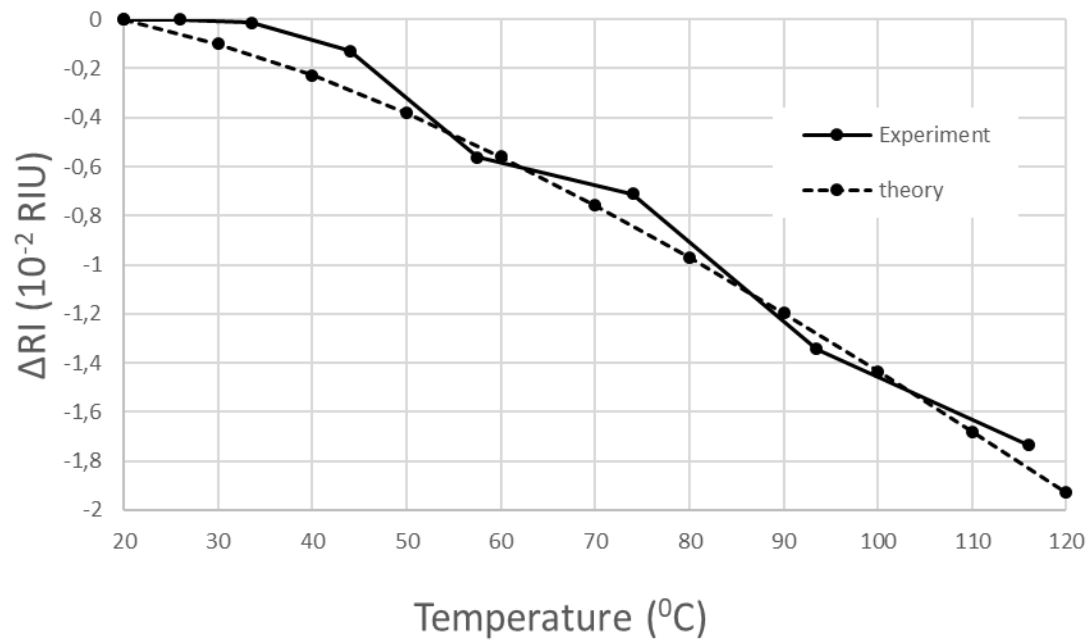


Figure C:3 Modelling of water drop refractive index difference versus temperature. Here, the modelled temperature is that fitting as much as possible the experimental plasmonic peak shift (contrary to Figure 4.21 where maximum channel temperature was used).



## Appendix D: On the effect of current injection on polarization

The experiment reported in § 4.6, i.e. measuring the plasmonic response of a water drop heated by current injection and using the spectral interrogation set-up was made using air as sensed medium and the angular interrogation set-up. During this experiment, we observed that the shift of the air plasmon with temperature was not measurable. First, the change of refractive index of air with temperature [128] is much less than that of water and reaches the limit of detection of our system. Second, the plasmonic response contrast was decreasing when injecting current. So, to appreciate what would be the reason of such a behaviour, we fixed the polarization of the impinging light beam and tried to adjust the polarization of the reflected light beam from the sensor surface. So as current is increased, polarization of output light beam shall be modified in order retrieving the highest contrast on the plasmonic response (Figure D:1).

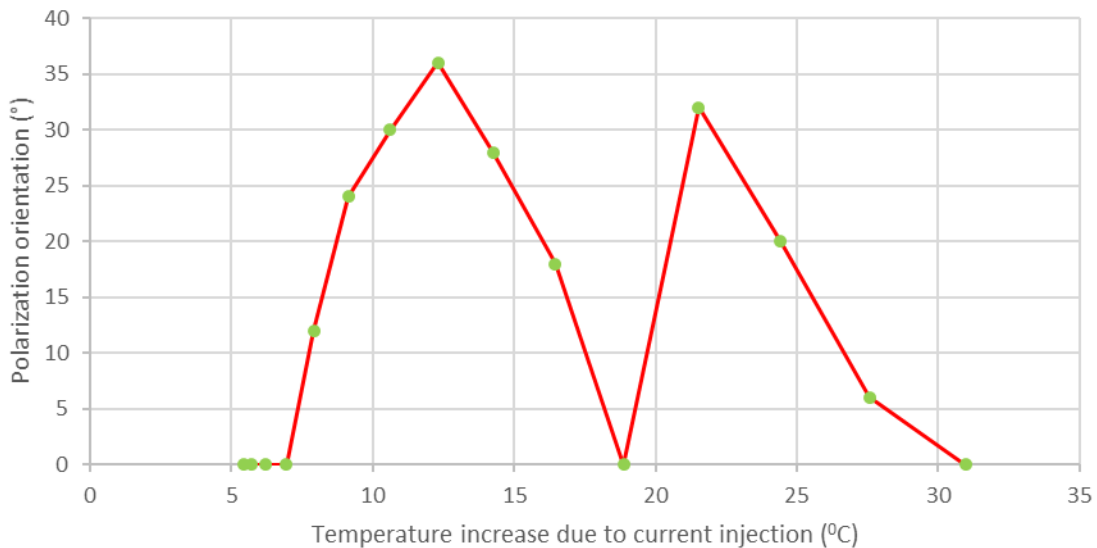


Figure D:1 Requested input light polarization modification in order to retrieve a full plasmonic response (angular interrogation set-up).

Further investigations must be done in order to determine what could be the cause of this phenomenon:

- thermal expansion of gold layer,
- drift velocity of injected carriers,
- .....



## REFERENCES

- [1] S. Subrahmanyam, S. A. Piletsky and A. P. F. Turner, “Application of natural receptors in sensors and assays” *Anal. Chem.*, Vol. 74(16) pp. 3942–3951, 2002, doi: 10.1021/ac025673+.
- [2] N. J. Sheikh and O. Sheikh, “Forecasting of biosensor technologies for emerging point of care and medical IoT applications using bibliometrics and patent analysis,” in *2016 Portland International Conference on Management of Engineering and Technology (PICMET)*, 2016, pp. 3082–3093, doi: 10.1109/PICMET.2016.7806585.
- [3] X. Luo and J. J. Davis, “Electrical biosensors and the label free detection of protein disease biomarkers primary” *Chem. Soc. Rev.*, Vol. 13 pp. 5944–5962, 2013, doi: 10.1039/c3cs60077g.
- [4] S. Roy and Z. Gao, “Nanostructure-based electrical biosensors” *Nanotoday*, Vol.4(4) pp. 318–334, 2009, doi: 10.1016/j.nantod.2009.06.003.
- [5] N. R. Shanmugam, “A review on ZnO-based electrical biosensors for cardiac biomarker detection” *Future Science*, vol. 3(4), 2017. doi: 10.4155/fsoa-2017-0006
- [6] Y. Lu, S. Peng, D. Luo and A. Lal, “Low-concentration mechanical biosensor based on a photonic crystal nanowire array” *Nat. Commun.*, Vol. 2, p. 578, 2011, doi: 10.1038/ncomms1587.
- [7] J. L. Arlett, E. B. Myers and M. L. Roukes, “Comparative advantages of mechanical biosensors” *Nat. Nanotechnol.*, Vol. 6(4) pp. 203–215, 2011, doi: 10.1038/nnano.2011.44.
- [8] C. Ziegler, “Cantilever-based biosensors” *Analytical and Bioanalytical Chemistry*, Vol.379(7-8) pp.946-959, doi: 10.1007/s00216-004-2694-y.
- [9] P. Damborsky, J. Svitel and J. Katrlík, “Optical biosensors” *Essays in Biochemistry*, Vol.60(1) pp. 91–100, 2016, doi: 10.1042/EBC20150010.
- [10] C. S. Huertas, O. Calvo-Lozano, A. Mitchell and L. M. Lechuga, “Advanced

- Evanescent-Wave Optical Biosensors for the Detection of Nucleic Acids : An Analytic Perspective” *Frontiers in Chemistry*, Vol.7 pp.1–25, 2019, doi: 10.3389/fchem.2019.00724.
- [11] R. Peltomaa, B. Glahn-Martínez, E. Benito-Peña and M. C. Moreno-Bondi, “Optical Biosensors for Label-Free Detection of Small Molecules” *Sensors* Vol. 18(12) 4126, 2018, doi: 10.3390/s18124126.
- [12] R. W. Wood, “XLII. On a remarkable case of uneven distribution of light in a diffraction grating spectrum” *Proc. of the Physical Society of London*, Vol.18(1) pp. 269-275, doi: 10.1088/1478-7814/18/1/325.
- [13] J. Su, “Label-Free Biological and Chemical Sensing Using Whispering Gallery Mode Optical Resonators : Past , Present , and Future” *Sensors*, Vol.17(3) 540, 2017, doi: 10.3390/s17030540.
- [14] K. I. Chen, B. R. Li and Y. T. Chen, “Silicon nanowire field-effect transistor-based biosensors for biomedical diagnosis and cellular recording investigation” *Nanotoday*, Vol. 6(2) pp. 131–154, 2011, doi: 10.1016/j.nantod.2011.02.001.
- [15] K. Kim *et al.*, “Silicon nanowire biosensors for detection of cardiac troponin I (cTnI) with high sensitivity” *Biosens. Bioelectron.*, Vol.77 pp. 695–701, 2016, doi: 10.1016/j.bios.2015.10.008.
- [16] R. Ahmad, T. Mahmoudi, M. S. Ahn and Y. B. Hahn, “Recent advances in nanowires-based field-effect transistors for biological sensor applications,” *Biosens. Bioelectron.*, Vol.100 pp. 312–325, 2018, doi: 10.1016/j.bios.2017.09.024.
- [17] M. Rubtsova, G. Presnova, D. Presnov, V. Krupenin, V. Grigorenko and A. Egorov, “Biosensor Based on a Nanowire Field-effect Transistor for the Determination of Prostate Specific Antigen” *Procedia Technol.*, Vol.27, pp. 234–235, 2017, doi: 10.1016/j.protcy.2017.04.099.
- [18] X. Fan, S. Sang, J. Hu, P. Li, G. Li, and W. Zhang, “Recent development of silicon nanowire FET biosensor for DNA detection,” *Proc. 2012 Int. Conf. Comput. Meas. Control Sens. Network, C. 2012*, pp. 201–205, 2012, doi: 10.1109/CMCSN.2012.52.

- [19] H. H. Kim, H. J. Jeon, H. K. Cho, J. H. Cheong, H. S. Moon and J. S. Go, “Highly sensitive microcantilever biosensors with enhanced sensitivity for detection of human papilloma virus infection” *Sensors Actuators, B Chem.*, Vol.221 pp. 1372–1383, 2015, doi: 10.1016/j.snb.2015.08.014.
- [20] C. Ziegler, “Cantilever-based biosensors” *Anal. Bioanal. Chem.*, Vol.379(7–8) pp. 946–959, 2004, doi: 10.1007/s00216-004-2694-y.
- [21] J. Pei, F. Tian and T. Thundat, “Glucose Biosensor Based on the Microcantilever” *Anal. Chem.*, Vol.76(2) pp. 292–297, 2004, doi: 10.1021/ac035048k.
- [22] R. Raiteri, M. Grattarola, H.-J. Butt and P. Skladal, and “Micromechanical cantilever-based biosensors” *Sensors Actuators B Chem.*, Vol.79(2-3) pp. 115–126, 2001. doi: 10.1016/S0925-4005(01)00856-5
- [23] M. C. Dixon, “Quartz crystal microbalance with dissipation monitoring: Enabling real-time characterization of biological materials and their interactions” *J. Biomol. Tech.*, Vol.19(3) pp. 151–158, 2008.
- [24] W. Liao, F. Wei, D. Liu, M. X. Qian, G. Yuan and X. S. Zhao, “FTIR-ATR detection of proteins and small molecules through DNA conjugation” *Sensors Actuators, B Chem.*, Vol.114(1), pp. 445–450, 2006, doi: 10.1016/j.snb.2005.06.021.
- [25] T. J. Moore and B. Sharma, “Direct Surface Enhanced Raman Spectroscopic Detection of Cortisol at Physiological Concentrations” *Anal. Chem.*, Vol.92(2) pp. 2052–2057, 2020, doi: 10.1021/acs.analchem.9b04532.
- [26] J. Ju, W. Liu, C. M. Perlaki, K. Chen, C. Feng and Q. Liu, “Sustained and Cost Effective Silver Substrate for Surface Enhanced Raman Spectroscopy Based Biosensing” *Sci. Rep.*, Vol.7(1), pp. 1–11, 2017, doi: 10.1038/s41598-017-07186-9.
- [27] A. K. Gaigalas *et al.*, “The Development of Fluorescence Intensity Standards” *J. Res. Natl. Inst. Stand. Technol.*, Vol.106(2) pp. 381–389, Apr. 2001, doi: 10.6028/jres.106.015.
- [28] L. Smith, M. Kohli, and A. M. Smith, “Expanding the Dynamic Range of Fluorescence Assays through Single-Molecule Counting and Intensity Calibration”

- J. Am. Chem. Soc.*, Vol.140(42) pp. 13904–13912, 2018, doi: 10.1021/jacs.8b08879.
- [29] D. Axelrod, “Evanescent excitation and emission in fluorescence microscopy” *Biophys. J.*, Vol.104(7) pp. 1401–1409, 2013, doi: 10.1016/j.bpj.2013.02.044.
- [30] C. Chen and J. Wang, “Optical biosensors: An exhaustive and comprehensive review” *Analyst*, Vol.145(5) pp. 1605–1628, 2020, doi: 10.1039/c9an01998g.
- [31] X. Yao *et al.*, “Sub-attomole oligonucleotide and p53 cDNA determinations via a high-resolution surface plasmon resonance combined with oligonucleotide-capped gold nanoparticle signal amplification” *Anal. Biochem.*, Vol. 354(2) pp. 220–228, 2006, doi: 10.1016/j.ab.2006.04.011.
- [32] G. García-Martínez *et al.*, “Development of a Mass Sensitive Quartz Crystal Microbalance (QCM)-Based DNA Biosensor Using a 50 MHz Electronic Oscillator Circuit” *Sensors*, Vol.11 pp. 7656–7664, 2011, doi: 10.3390/s110807656.
- [33] P. S. Waggoner, M. Varshney and H. G. Craighead, “Detection of prostate specific antigen with nanomechanical resonators” *Lab Chip*, Vol.9(21) pp. 3095–3099, 2009, doi: 10.1039/b907309b.
- [34] Y. C. Kwon *et al.*, “Development of a surface plasmon resonance-based immunosensor for the rapid detection of cardiac troponin I” *Biotechnol. Lett.*, Vol.33(5) pp. 921–927, 2011, doi: 10.1007/s10529-010-0509-0.
- [35] J. Lee, W. Shen, K. Payer, T. P. Burg and S. R. Manalis, “Toward attogram mass measurements in solution with suspended nanochannel resonators” *Nano Lett.*, Vol.10(7) pp. 2537–2542, 2010, doi: 10.1021/nl101107u.
- [36] C. Ricciardi *et al.*, “Immunodetection of 17 $\beta$ -estradiol in serum at ppt level by microcantilever resonators” *Biosens. Bioelectron.*, Vol.40(1) pp. 407–411, 2013, doi: 10.1016/j.bios.2012.08.043.
- [37] G.-J. Zhang *et al.*, “Silicon nanowire biosensor for highly sensitive and rapid detection of Dengue virus” *Sensors Actuators B Chem.*, Vol.146(1) pp. 138–144, 2010, doi: <https://doi.org/10.1016/j.snb.2010.02.021>.

- [38] G. Presnova *et al.*, “Biosensor based on a silicon nanowire field-effect transistor functionalized by gold nanoparticles for the highly sensitive determination of prostate specific antigen” *Biosens. Bioelectron.*, Vol.88 pp. 283–289, 2017, doi: 10.1016/j.bios.2016.08.054.
- [39] C. A. Vu and W. Y. Chen, “Field-effect transistor biosensors for biomedical applications: Recent advances and future prospects” *Sensors*, Vol.19(19), 2019, doi: 10.3390/s19194214.
- [40] P. Ambhorkar *et al.*, “Nanowire-based biosensors: From growth to applications” *Micromachines*, Vol.9(12) pp. 1–19, 2018, doi: 10.3390/mi9120679.
- [41] R. F. Dutra and L. T. Kubota, “An SPR immunosensor for human cardiac troponin T using specific binding avidin to biotin at carboxymethyl-dextran-modified gold chip” *Clin. Chim. Acta*, Vol.376(1–2) pp. 114–120, 2007, doi: 10.1016/j.cca.2006.07.029.
- [42] J. Jose, M. Park and J. C. Pyun, “E. coli outer membrane with autodisplayed Z-domain as a molecular recognition layer of SPR biosensor” *Biosens. Bioelectron.*, Vol.25(5) pp. 1225–1228, 2010, doi: 10.1016/j.bios.2009.09.025.
- [43] “Biosensor Market Size, Technology, Trends and Growth | Global Industry Forecast 2025” [Online]. Available: <https://www.marketresearchfuture.com/reports/biosensor-market-1228>. [Accessed: 22-Oct-2020].
- [44] F. J. Gruhl, B. E. Rapp and K. Länge, “Biosensors for diagnostic applications” *Adv. Biochem. Eng. Biotechnol.*, Vol.133, pp. 115–148, 2013, doi: 10.1007/10\_2011\_130.
- [45] R. Bhadoria and H. Singh, “Recent advances of biosensors in biomedical sciences” *International Journal of Drug Delivery*, Vol.3(4) pp. 571–585, 2011, doi: 10.5138/506.
- [46] L. Teixeira and D. Agnol, “Recent Advances in Biosensor Technology for Potential Applications – An Overview” *Front. Bioeng. Biotechnol.*, Vol.4, pp. 1–9, 2016, doi:

10.3389/fbioe.2016.00011.

- [47] J. P. Bahamonde, H. N. Nguyen, S. K. Fanourakis and D. F. Rodrigues, “Recent advances in graphene-based biosensor technology with applications in life sciences” *J. Nanobiotechnology*, Vol.16 pp. 1–17, 2018, doi: 10.1186/s12951-018-0400-z.
- [48] J. Kim, A. S. Campbell, B. E.-F. de Ávila and J. Wang, “Wearable biosensors for healthcare monitoring” *Nat. Biotechnol.*, Vol.37(4) pp. 389–406, 2019, doi: 10.1038/s41587-019-0045-y.
- [49] C. Gouvea, “Biosensors for health applications” *Biosensors for Health, Environment and Biosecurity*, 2011, doi: 10.5772/17103.
- [50] J. Masson, “Surface Plasmon Resonance Clinical Biosensors for Medical Diagnostics” 2017, doi: 10.1021/acssensors.6b00763.
- [51] B. M. Paddle, “Biosensors for chemical and biological agents of defence interest” *Biosens. Bioelectron.*, Vol.11(11) pp. 1079–1113, 1996, doi: 10.1016/0956-5663(96)82333-5.
- [52] Opportunities in Biotechnology for Future Army Applications. 2001.
- [53] S. F. F. Torriani, J. P. E. Melichar, C. Mills, N. Pain, H. Sierotzki and M. Courbot, “Zymoseptoria tritici: A major threat to wheat production, integrated approaches to control” *Fungal Genet. Biol.*, Vol.79 pp. 8–12, 2015, doi: 10.1016/j.fgb.2015.04.010.
- [54] I. Freestone, N. Meeks, M. Sax and C. Higgitt, “The Lycurgus Cup - A Roman nanotechnology” *Gold Bull.*, Vol.40(4) pp. 270–277, 2008, doi: 10.1007/BF03215599.
- [55] P. Manley, S. Burger, F. Schmidt and M. Schmid, “Design Principles for Plasmonic Nanoparticle Devices” *Progress in non-linear nano-optics* pp. 223–247, 2015, doi: 10.1007/978-3-319-12217-5\_13.
- [56] E. Martinsson and D. Aili, “Refractometric Sensing Using Plasmonic Nanoparticles,” *Encyclopedia of Nanotechnology*, B. Bhushan, Ed. Dordrecht:

Springer Netherlands, 2016, pp. 3432–3440.

- [57] R. W. Wood, “Diffraction gratings with controlled groove form and abnormal distribution of intensity” *London, Edinburgh, Dublin Philos. Mag. J. Sci.*, Vol. 23(134) pp. 310–317, 1912, doi: 10.1080/14786440208637224.
- [58] Lord Rayleigh, “On the Dynamical Theory of Gratings” *Proc. R. Soc. London. Ser. A, Contain. Pap. a Math. Phys. Character*, Vol.79(532) pp. 399–416, 1907.
- [59] A. Hessel and A. A. Oliner, “A New Theory of Wood’s Anomalies on Optical Gratings” *Applied Optics*, Vol.4(10) pp. 1275-1297 1965, doi: 10.1364/AO.4.001275.
- [60] U. Fano, “The Theory of Anomalous Diffraction Gratings and of Quasi-Stationary Waves on Metallic Surfaces ( Sommerfeld’s Waves)” *Journal of the Optical Society of America*, Vol.31(3) pp.213-222, 1941, doi: 10.1364/JOSA.31.000213.
- [61] G. Isfort, K. Schierbaum and D. Zerulla, “Polarization dependence of surface plasmon polariton emission” *Phys. Rev. B*, Vol.74(3) p. 33404, 2006, doi: 10.1103/PhysRevB.74.033404.
- [62] E. Kretschmann and H. Raether, “Radiative Decay of Non Radiative Surface Plasmons Excited by Light” *Zeitschrift fur Naturforsch. - Sect. A J. Phys. Sci.*, Vol.23(12) pp. 2135–2136, 1968, doi: 10.1515/zna-1968-1247.
- [63] Y. Ma *et al.*, “Integrated color filter and polarizer based on two-dimensional superimposed nanowire arrays” *J. Appl. Phys.*, Vol.116(4) 044314, 2014, doi: 10.1063/1.4891804.
- [64] V. M. Agranovich and D. L. Mills, “Surface Polaritons, Electromagnetic Waves at Surfaces and Interfaces” North-Holland, Amsterdam and New York, 1982,
- [65] J. C. Quail, J. G. Rako, H. J. Simon and R. T. Deck, “Optical Second-Harmonic Generation with Long-Range Surface Plasmons,” *Phys. Rev. Lett.*, Vol.50(25) pp. 1987–1989, 1983, doi: 10.1103/PhysRevLett.50.1987.
- [66] H. Raether, "Surface Plasmons on Smooth and Rough Surfaces and on Gratings",

Vol. 111 of Springer Tracts in Modern Physics. 1988.

- [67] M. S. Golden, A. C. Bjornes and R. M. Georgiadis, “Distance- and wavelength-dependent dielectric function of Au nanoparticles by angle-resolved surface plasmon resonance imaging” *J. Phys. Chem. C*, Vol.114(19) pp. 8837–8843, 2010, doi: 10.1021/jp101850d.
- [68] S. Deng, P. Wang and X. Yu, “Phase-Sensitive Surface Plasmon Resonance Sensors : Recent Progress and Future Prospects” *Sensors*, Vol.17(12) 2819, 2017, doi: 10.3390/s17122819.
- [69] N. Olson and J. Bae, “Biosensors-publication trends and knowledge domain visualization” *Sensors*, Vol.19(11) 2615, 2019, doi: 10.3390/s19112615.
- [70] W.-K. Kuo, C.-H. Chang and C.-J. Wu, “Phase detection sensitivity enhancement of grating-coupled surface plasmon resonance (SPR) sensor using non-zero azimuth angle incident light” *Plasmon. Met. Nanostructures Their Opt. Prop. X*, Proc. SPIE Vol.8457 845730, 2012, doi: 10.1117/12.927748.
- [71] R. B. M. Schasfoort, “Chapter 1. Introduction to Surface Plasmon Resonance” *Handb. Surf. Plasmon Reson.*, pp. 1–26, 2017, doi: 10.1039/9781788010283-00001.
- [72] X. Yao *et al.*, “Sub-attomole oligonucleotide and p53 cDNA determinations via a high-resolution surface plasmon resonance combined with oligonucleotide-capped gold nanoparticle signal amplification” *Anal. Biochem.*, Vol.354(2) pp. 220–228, Jul. 2006, doi: 10.1016/j.ab.2006.04.011.
- [73] A. B. Taylor and P. Zijlstra, “Single-Molecule Plasmon Sensing: Current Status and Future Prospects” *ACS Sensors*, Vol.2(8) pp. 1103–1122, 2017, doi: 10.1021/acssensors.7b00382.
- [74] P. Kvasnička, K. Chadt, M. Vala, M. Bocková and J. Homola, “Toward single-molecule detection with sensors based on propagating surface plasmons” *Opt. Lett.*, Vol.37(2) pp. 163-165, 2012, doi: 10.1364/ol.37.000163.
- [75] S. Ahmad *et al.*, “An overview of sensitivity and selectivity of biosensors for environmental applications” *Tools, Techniques and Protocols for Monitoring*

- Environmental Contaminants, pp. 53–73, 2019, doi: 10.1016/B978-0-12-814679-8.00003-0.
- [76] Y. H. Huang, H. P. Ho, S. Y. Wu and S. K. Kong, “Detecting Phase Shifts in Surface Plasmon Resonance: A Review” *Advances in Optical technologies*, Vol. 2012 471957, 2012, doi: 10.1155/2012/471957.
- [77] E. Wijaya, “Design and optimization of Surface Plasmon Resonance (SPR) biosensors” <http://www.theses.fr>, Dec. 2012.
- [78] J. Hottin, E. Wijaya, L. Hay, S. Maricot, M. Bouazaoui, and J. P. Vilcot, “Comparison of Gold and Silver/Gold Bimetallic Surface for Highly Sensitive Near-infrared SPR Sensor at 1550 nm” *Plasmonics*, Vol.8(2) pp. 619–624, 2013, doi: 10.1007/s11468-012-9446-1.
- [79] S. Szunerits, N. Maalouli, E. Wijaya, J. P. Vilcot, and R. Boukherroub, “Recent advances in the development of graphene-based surface plasmon resonance (SPR) interfaces” *Anal. Bioanal. Chem.*, Vol.405(5) pp. 1435–1443, 2013, doi: 10.1007/s00216-012-6624-0.
- [80] E. Wijaya *et al.*, “Surface plasmon resonance-based biosensors: From the development of different SPR structures to novel surface functionalization strategies” *Curr. Opin. Solid State Mater. Sci.*, Vol.15(5) pp. 208–224, 2011, doi: 10.1016/j.cossms.2011.05.001.
- [81] M. Zekriti, “Temperature Effects on the Resolution of Surface-Plasmon-Resonance-Based Sensor” *Plasmonics*, Vol.14(3), pp. 763–768, 2019, doi: 10.1007/s11468-018-0855-7.
- [82] S. Zeng, D. Baillargeat, H. P. Ho and K. T. Yong, “Nanomaterials enhanced surface plasmon resonance for biological and chemical sensing applications” *Chem. Soc. Rev.*, Vol.43(10) pp. 3426–3452, 2014, doi: 10.1039/c3cs60479a.
- [83] S. I. Bozhevolnyi, “Dynamic components utilizing long-range surface plasmon polaritons” *Nanophotonics with Surface Plasmons*, V. M. Shalaev and S. Kawata, Eds. Amsterdam: Elsevier, 2007, pp. 1–34.

- [84] H. Kano, D. Nomura and H. Shibuya, “Excitation of surface-plasmon polaritons by use of a zeroth-order Bessel beam” *Appl. Opt.*, Vol.43(12) pp. 2409–2411, 2004, doi: 10.1364/AO.43.002409.
- [85] A. Otto, “Excitation of nonradiative surface plasma waves in silver by the method of frustrated total reflection” *Zeitschrift für Phys.*, Vol.216(4) pp. 398–410, 1968, doi: 10.1007/BF01391532.
- [86] C. J. Powell and J. B. Swan, “Effect of Oxidation on the Characteristic Loss Spectra of Aluminum and Magnesium” *Phys. Rev.*, Vol.118(3) pp. 640–643, 1960, doi: 10.1103/PhysRev.118.640.
- [87] R. H. Ritchie, “Plasma Losses by Fast Electrons in Thin Films” *Phys. Rev.*, Vol.106(5) pp. 874–881, 1957, doi: 10.1103/PhysRev.106.874.
- [88] E. Sugawara and H. Nikaido, “Properties of AdeABC and AdeIJK efflux systems of *Acinetobacter baumannii* compared with those of the AcrAB-TolC system of *Escherichia coli*” *Antimicrob. Agents Chemother.*, Vol.58(12) pp. 7250–7257, 2014, doi: 10.1128/AAC.03728-14.
- [89] A. Hille *et al.*, “Second Harmonic Generation from Metal Nano-Particle Resonators: Numerical Analysis on the Basis of the Hydrodynamic Drude Model” *J. Phys. Chem. C*, Vol.120(2) pp. 1163–1169, 2016, doi: 10.1021/acs.jpcc.5b08348.
- [90] J. Hampson, “Determination of electrical conductivity parameters of metals from infrared measurements” *Infrared Phys.*, Vol.4(3) pp. 171–186, 1964, doi: 10.1016/0020-0891(64)90023-5.
- [91] A. I. Galuza and A. B. Beznosov, “Optical functions of the Drude model: Transformation of the spectra over wide ranges of parameters” *Low Temp. Phys.*, Vol.27(3) pp. 216–227, 2001, doi: 10.1063/1.1355519.
- [92] A. I. Galuza and A. B. Beznosov, “Optical functions of the Drude model: transformation of the spectra over wide ranges of parameters” *Low Temp. Phys.*, Vol.27(3) pp. 216–227, 2001, doi: 10.1063/1.1355519.
- [93] H. A. Lorentz, *The Theory of Electrons and Its Applications to the Phenomena of*

Light and Radiant Heat. Dover Publications, 2003.

- [94] A. V Sokolov, *Optical Properties of Metals*. American Elsevier Publishing Company, 1967.
- [95] S. Maegawa, J. Yamaguchi, F. Itoigawa and T. Nakamura, “Discussion on Surface Plasmon Resonance Technique in the Otto Configuration for Measurement of Lubricant Film Thickness” *Tribol. Lett.*, Vol.62(2) pp. 1–14, 2016, doi: 10.1007/s11249-016-0659-x.
- [96] N. A. S. Omar *et al.*, “Quantitative and selective surface plasmon resonance response based on a reduced graphene oxide–polyamidoamine nanocomposite for detection of dengue virus E-proteins” *Nanomaterials*, Vol.10(3) pp. 1–14, 2020, doi: 10.3390/nano10030569.
- [97] E. Desimoni and B. Brunetti, “About Estimating the Limit of Detection by the Signal to Noise Approach,” *Pharm. Anal. Acta*, Vol.6(4) 1000355, 2015, doi: 10.4172/2153-2435.1000355.
- [98] E. Reprinted, “Electronically Reprinted from October 2003,” *October*, vol. 15, no. 7, 2003.
- [99] “The Limit of Detection | Chromatography Online.” [Online]. Available: <https://www.chromatographyonline.com/view/limit-detection>. [Accessed: 25-Oct-2020].
- [100] Z. Liu, G. Liu, X. Liu and G. Fu, “Plasmonic sensors with an ultra-high figure of merit” *Nanotechnology*, Vol.31(11) 115208, 2019, doi: 10.1088/1361-6528/ab5a00.
- [101] Q. Q. Meng, X. Zhao, C. Y. Lin, S. J. Chen, Y. C. Ding and Z. Y. Chen, “Figure of merit enhancement of a surface plasmon resonance sensor using a low-refractive-index porous silica film” *Sensors*, Vol.17(8) 1846, 2017, doi: 10.3390/s17081846.
- [102] “Refractive index of CDGM - ZF (Dense flint) - H-ZF1.” [Online]. Available: <https://refractiveindex.info/?shelf=glass&book=CDGM-ZF&page=H-ZF1>. [Accessed: 25-Oct-2020].

- [103] G. M. Hale and M. R. Querry, "Optical Constants of Water in the 200-nm to 200- $\mu\text{m}$  Wavelength Region" *Appl. Opt.*, Vol.12(3) pp. 555-563, 1973, doi: 10.1364/ao.12.000555.
- [104] L. Kai-Qun *et al.*, "Temperature Effects on Prism-Based Surface Plasmon Resonance Senso," *Chinese Phys. Lett.*, Vol.24(11) pp. 3081-3084, 2007, doi: 10.1088/0256-307x/24/11/018.
- [105] H. P. Chiang *et al.*, "Effects of temperature on the surface plasmon resonance at a metal-semiconductor interface" *Thin Solid Films*, Vol. 515(17) pp. 6953-6961, 2007, doi: 10.1016/j.tsf.2007.02.034.
- [106] R. Gupta, M. J. Dye, and W. A. Weimer, "Preparation and characterization of surface plasmon resonance tunable gold and silver films" *J. Appl. Phys.*, Vol.92(9) pp. 5264-5271, 2002, doi: 10.1063/1.1511275.
- [107] Y. Sun, D. Song, Z. Li, Y. Bai and H. Zhang, "Surface plasmon resonance biosensor based on Hg/Ag-Au film" *Anal. Bioanal. Chem.*, Vol.387(5) pp. 1875-1882, 2007, doi: 10.1007/s00216-006-1042-9.
- [108] <https://www.cargille.com/matching-liquids/> (Accessed 8 July 2020), "Matching Liquids - Cargille Labs." [Online]. Available: <https://www.cargille.com/matching-liquids/>. [Accessed: 25-Oct-2020].
- [109] E. T. Fogg, A. N. Hixson and A. R. Thompson, "Densities and Refractive Indexes for Ethylene Glycol-Water Solutions" *Anal. Chem.*, Vol.27(10) pp. 1609-1611, Oct. 1955, doi: 10.1021/ac60106a033.
- [110] "Refractive index of  $\text{C}_2\text{H}_4(\text{OH})_2$  (Ethylene glycol) - El-Kashef." [Online]. Available: <http://www.refractometer.pl/refraction-datasheet-ethylene-glycol>. [Accessed: 25-Oct-2020].
- [111] "Laser lithography system | Dilase 650." [Online]. Available: <https://www.kloe-france.com/en/laser-lithography/photolithography-systems/direct-laser-writing/dilase-650>. [Accessed: 26-Oct-2020].
- [112] NanoFab, "NanoFab Tool: Bruker Dektak XT contact profilometer | NIST."

- [Online]. Available: <https://www.nist.gov/laboratories/tools-instruments/nanofab-tool-bruker-dektak-xt-profilometer>. [Accessed: 26-Oct-2020].
- [113] J. R. Sambles and K. C. Elsom, “The temperature dependence of the electrical resistivity of gold films” *Solid State Commun.*, Vol.52(4) pp. 367–370, 1984, doi: [https://doi.org/10.1016/0038-1098\(84\)90015-2](https://doi.org/10.1016/0038-1098(84)90015-2).
- [114] J.W.C. Vries “Temperature-dependent resistivity measurements on polycrystalline SiO<sub>2</sub>-covered thin nickel films” *Thin Solid Films*, Vol.150(2-3) pp. 209–215, 1987, doi: [10.1016/0040-6090\(87\)90092-7](https://doi.org/10.1016/0040-6090(87)90092-7).
- [115] C. R. Tellier and A. J. Tossier, “The temperature coefficient of resistivity of polycrystalline radio frequency sputtered aluminium films” *Thin Solid Films*, Vol.43(3) pp. 261–266, 1977, doi: [10.1016/0040-6090\(77\)90287-5](https://doi.org/10.1016/0040-6090(77)90287-5).
- [116] M. Kaviany and A. Kanury, *Principles of Heat Transfer*, vol. 55, no. 5. 2002.
- [117] D. G. Brooks and J. Adam, *Trace Currents and Temperatures Revisited*. 2015.
- [118] “Accurate Thermal Analysis, Including Thermal Coupling Of On-Chip Hot Interconnect.” [Online]. Available: <https://semiengineering.com/accurate-thermal-analysis-including-thermal-coupling-of-on-chip-hot-interconnect/>. [Accessed: 26-Oct-2020].
- [119] W. J. Palm, “Wavelength and temperature dependence of continuous-wave laser absorptance in Kapton<sup>®</sup> thin films” *Opt. Eng.*, Vol.51(12). 121802, 2012, doi: [10.1117/1.oe.51.12.121802](https://doi.org/10.1117/1.oe.51.12.121802).
- [120] “InfraScope™ Systems | QFI Corporation.” [Online]. Available: <http://www.quantumfocus.com/products-2/infrascopetm/>. [Accessed: 26-Oct-2020].
- [121] T. Okada, R. Ishige, and S. Ando, “Analysis of thermal radiation properties of polyimide and polymeric materials based on ATR-IR spectroscopy” *J. Photopolym. Sci. Technol.*, Vol.29(2) pp. 251–254, 2016, doi: [10.2494/photopolymer.29.251](https://doi.org/10.2494/photopolymer.29.251).
- [122] A. N. Bashkatov and E. A. Genina, “Water refractive index in dependence on

temperature and wavelength: a simple approximation” SPIE Proceedings Volume 5068, Saratov Fall Meeting 2002: Optical Technologies in Biophysics and Medicine IV pp. 393–395, 2003, doi: 10.1117/12.518857.

- [123] K. Y. Bliokh, F. J. Rodríguez-Fortuño, A. Y. Bekshaev, Y. S. Kivshar and F. Nori, “Electric-current-induced unidirectional propagation of surface plasmon-polaritons” *Opt. Lett.*, Vol.43(5) pp. 963-966, 2018, doi: 10.1364/ol.43.000963.
- [124] “RTD Products | Industry Standards.” [Online]. Available: <http://www.rtd-products.co.uk/industry-standards.html>. [Accessed: 26-Oct-2020].
- [125] R. J. Corruccini, “Annealing of platinum for thermometry,” *J. Res. Natl. Bur. Stand. (1934)*., Vol.47(2) p. 94, 1951, doi: 10.6028/jres.047.013.
- [126] M. T. Bakouche *et al.*, “Leak-free integrated microfluidic channels fabrication for surface plasmon resonance applications,” *J. Micromechanics Microengineering*, Vol.30(12) 125003, 2020, doi: 10.1088/1361-6439/abb991.
- [127] “3M™ 8213 Adhésif Transparent - 305 mm x 30 m.” [Online]. Available: [https://www.3mfrance.fr/3M/fr\\_FR/notre-societe-fr/tous-les-produits-3M/~3M-8213-Adhésif-Transparent-305-mm-x-30-m/?N=5002385+3291511840&preselect=3293786499&rt=rud](https://www.3mfrance.fr/3M/fr_FR/notre-societe-fr/tous-les-produits-3M/~3M-8213-Adhésif-Transparent-305-mm-x-30-m/?N=5002385+3291511840&preselect=3293786499&rt=rud). [Accessed: 27-Oct-2020].
- [128] P.E. Ciddor "Refractive index of air: new equations for the visible and the infrared," *Applied Optics*, Vol. 35(9), pp. 1566-1573 (1996) doi:10.1364/AO.35.001566
- [129] M.T Bakouche "Fonctionnalisation de surface et développement de biocapteurs SPR microfluidiques pour la détection du *Zymoseptoria Tritici* et de *Candida Albicans*", PhD thesis, University of Lille, May 2021
- [130] B. Koo, C.E. Jin, M. Bae, Y. Jang, J.Y. Kim, S.H. Kim, Y. Shin, Yong., "Detection of *Coxiella burnetii* Using Silicon Microring Resonator in Patient Blood Plasma" *Micromachines*, Vol.10 p. 427, 2019, doi: 10.3390/mi10070427.
- [131] S. Esfahani, J.P. Specht, G. Jolly, M. Cole, J.W. Gardner, "Solidly Mounted Resonator (SMR) Sensors for Biomedical Applications" *Proceedings*, Vol. 56(1),

11, 2020. doi:10.3390/proceedings2020056011

- [132] B.G. Andryukov, N.N. Besednova, R.V. Romashko, T.S. Zaporozhets, T.A. Efimov, "Label-Free Biosensors for Laboratory-Based Diagnostics of Infections: Current Achievements and New Trends", *Biosensors*, Vol. 10(2), 11, 2020. doi:10.3390/bios10020011
- [133] S. Yoshida, S. Ishihara, T. Arakawa, Y. Kokubun, "Highly sensitive optical biosensor based on silicon-microring-resonator-loaded Mach–Zehnder interferometer" *Japanese Journal of Applied Physics*, Vol. 56(4S), 04CH08, 2017. doi: 10.7567/JJAP.56.04CH08.
- [134] F. Chien, S. Hsu, and C. Hsu, "Microring Resonator Biosensor Sensitivity Enhancement through Higher Order Interferograms," *Optical Sensors and Sensing Congress (ES, FTS, HISE, Sensors)*, OSA Technical Digest (Optical Society of America, 2019), paper STu3C.4.

## Résumé:

Mon travail de thèse s'inscrivait dans celui, plus général, de développement d'un système de détection biologique portable affichant sensibilité, précision et répétabilité et dont le champ d'applications visait les domaines médicaux et phytosanitaires. Ce système est basé sur le principe physique de base qui est la Résonance Plasmonique de Surface. Le but était alors de démocratiser cette technique au niveau du chevet du patient ou du champ. Dans ce contexte et dans le cadre du projet INTERREG FWVL BIOSENS, je me suis plus particulièrement attaché à l'étude de différentes innovations au niveau du capteur. Parmi toutes les techniques de détection biologique, la technique de mesure à base de SPR a déjà été amplement étudiée car elle présente des avantages indéniables comme sa sensibilité, sa mesure en temps réel ou encore la non-nécessité de marquage des molécules. Bien que cette technique soit donc bien connue dans le domaine de la détection, la température de tout échantillon influe sur son indice optique, qui est la seule valeur détectée par un tel capteur, et peut donc être interprétée comme le résultat d'une interaction biologique. Ceci amène un réel défi dans le cas d'un système portable pour lequel l'intégration d'une enceinte thermostatée est source d'encombrement et de consommation énergétique. Un capteur SPR 4 canaux a été développé et la température des échantillons est directement contrôlée par chauffage par effet Joule de la couche plasmonique elle-même. Le fonctionnement de ce type de chauffage a été modélisé sous COMSOL et la caractérisation expérimentale a montré qu'il ne perturbait pas le principe de détection. De l'eau a été chauffée par injection de courant et la variation d'indice optique obtenue comparée à la théorie. Nous avons aussi démontré qu'il était possible de contrôler en température indépendamment chacun des quatre canaux sans apparition d'interférence thermique. De manière à contrôler plus finement la température, un capteur de température a aussi été intégré au niveau de la couche plasmonique. Ce contrôle de la température peut alors être utilisé soit pour maintenir une température constante au niveau des échantillons soit pour déterminer l'effet de la température sur une interaction biologique. De manière à diminuer le coût du capteur, un capteur sur film plastique a été fabriqué et testé. Il a permis d'obtenir une réponse plasmonique sur l'air et l'eau. L'utilisation d'un prisme en PDMS ainsi que son couplage avec le capteur sur film a été investiguée de manière à obtenir une plateforme de test la moins coûteuse possible.

## Abstract:

The overall goal of this study was to develop a portable biological detection system with high sensitivity, accuracy and repeatability to be used in either the phytosanitary or the medical domain. This system is based on the Surface Plasmon Resonance (SPR) physical principle. Such a use of this principle is already achieved but leads to laboratory equipment. The goal here is to democratize its use up to an on field or point of care measurement system. In this context and within the frame of the BIOSENS INTERREG FWVL project, I worked more particularly on several developments around the sensor. From all the existing biosensor technologies, surface plasmon resonance (SPR) sensing technology has received continuous attention due to its advantages of a high-sensitivity, label-free and fast response time. Although the SPR sensing technique being legend in the sensor community, currently the temperature of the sample needs to be carefully maintained and controlled because SPR signal varies with temperature and any change in SPR signal can be interpreted as a biological interaction. This gives a huge challenge in the portable application that is targeted since embedding of a temperature controlled chamber size and energy consuming. A SPR sensor design including 4 SPR channels has been made and the temperature is controlled in real time by using Joule effect. Temperature behavior has been modelled under COMSOL and we experimentally demonstrated that the temperature modulation of SPR channel by Joule effect does not affect the detection scheme. Water was heated by injecting current through the plasmonic layer and the refractive index change of water due to temperature was measured and compared with the theory. We also demonstrated that the temperature of each of the 4 channels can be controlled independently without any thermal crosstalk. In order achieving a more precise monitoring of sample temperature, a temperature sensor was also fabricated on top of the plasmonic layer, allowing the real temperature at the sensor surface to be monitored in real time. This temperature control can so be used either to maintain the temperature of biologic samples or to identify the effect of temperature on biomolecular interactions. On addressing the cost of the sensing tool, a flexible and cheap SPR sensor made on tape has been fabricated and tested. Air and water plasmonic responses were measured using such a "tape sensor". A PDMS prism has already been investigated and combined to the tape sensor making then a very cheap sensing platform.